The Growth of Graphene on Nickel Thin Films

by

Syarifah Norfaezah Sabki, B.Sc., M.Sc.

Thesis submitted to the University of Nottingham
for the degree of Doctor of Philosophy

May 2012

The University of
Nottingham

UNITED KINGDOM · CHINA · MALAYSIA

Abstract

The growth of graphene on Ni thin films using several different methods is discussed. These methods include no intentional introduction of carbon, immersion in an organic solvent, exposure to carbon-containing gas and a solid state approach by decomposition of molecules. All the methods have produced single layer graphene over a large area. We suggest that the graphene formation without intentional introduction of carbon involves conversion of carbon-containing adsorbates on SiO_2. This process has been verified by our experiment of graphene growth by decomposition of C_{60}, in which C_{60} is deposited on top of SiO_2 and buried under Ni thin film. Single layer graphene has successfully formed which suggests that the carbon from C_{60} has diffused and segregated to the top of the Ni surface. So we investigate the effect of outgassing aimed to eliminate adsorbates on SiO_2. Graphene growth by immersion in an organic solvent was initially performed to investigate the effect of outgassing process, and single layer graphene is formed but is highly defective, as determined by the intensity of the Raman D band. We found that outgassing the SiO_2 is important to produce single layer graphene, but the defects in graphene are not significantly reduced. Graphene growth method using propylene is carried out to identify the factors that influence the amount of defects and to reduce through optimization of growth parameters. The graphene defects are reduced significantly by varying the annealing temperature and exposure time to propylene. We found that different Ni thickness do not affect the defect formation in graphene but do improve the Ni surface morphology. Graphene growth by decomposition of C_{60} on Ni thin film produced graphene layers with controlled thickness. This molecular carbon source provides a method of controlling the total dosage of carbon introduced into the film with a high degree of precision. We found that the C_{60} coverage, annealing temperature, and deposition sequence influence the properties of graphene layers. We also presented preliminary results of graphene enhanced Raman scattering (GERS) of adsorbed PTCDI. We demonstrate

that single layer graphene is a very good substrate for Raman enhancement in which the adsorbed molecules can be detected at a small fraction of monolayer coverage. Using the same transfer method typically used for graphene, we managed to transfer PTCDI on graphene from Ni film to SiO_2. Here we demonstrate the effect of a substrate for graphene which can give rise to the enhancement of a Raman signal of adsorbed molecules.

List of Publications

1. A.J. Pollard, R.R. Nair, **S.N. Sabki**, C. R. Staddon, L.M.A. Perdigao, C.H. Hsu, S. Gangopadhyay, H. F. Gleesom, A.K. Geim, and P.H. Beton, "Formation of Monolayer Graphene by Annealing Sacrificial Nickel Thin Film", *J. Phys. Chem. C* **113**, 16565, 2009.

2. L.M.A Perdigao, **S.N. Sabki**, J.M. Garfitt, P. Capiod, and P.H. Beton, "Graphene Formation by Decomposition of C_{60}", *J. Phys. Chem C* **115**, 7472, 2010.

Presentation:

1. **S.N. Sabki**, A.J. Pollard, L.M.A. Perdigao, and P.H. Beton, "Monolayer graphene grown on Nickel and transfer to dielectric substrate" – (Oral) Conf. on Nanoscale Physics – Condensed Matter and Material Physics (CMMP) 2009, 15 – 17 Dec 2009, University of Warwick, UK.

2. **S.N. Sabki**, L.M.A. Perdigao, A.J. Pollard, R.R. Nair, C.R. Staddon, C.H. Hsu, J.M. Garfitt, S. Gangopadhyay, P. Capiod, and P.H. Beton, "Monolayer and Few-Layer Graphene grown on Nickel" – (Poster) UK-Japan Graphene Workshop, 3 – 4 Feb 2011, Lancester University, UK.

Acknowledgements

This thesis would have not been possible without the help of many people and organizations. So I would like to thank them for various reasons:

Ministry of Higher Education (MOHE) Malaysia and University Malaysia Perlis (UniMAP) for the sponsor of my PhD study.

Prof. Peter H. Beton, my supervisor for supervising me in four years of my PhD, for guiding me through this work, for the help in the lab, for the support in my study extension, for the useful discussion, for the proof reading, for everything. Thank you, without you this thesis will not be possible to be accomplished.

Luis M. Perdigao, for the help in the lab especially in operating the UHV system, for some of the data and the useful discussion. Andy Pollard, Matthew Blunt, Jason Garfitt, Haya Alhummiany and others, also for the help in the lab. Rahul Nair for helping in the Raman measurement using the facilities in the University of Manchester. Jas Chauhan for the help in the clean room and Chris Staddon for the help in the XRD measurement.

Malaysian friends for all the laughs and hangouts, for the help when my family was in difficult time and for the time we spent together. An appreciation to Zanariah and Azman for looking after our son when we could not afford sending him to the nursery. Thank you for loving Iskandar, just like we do.

Fadhilah Sabki, my sister for coming to UK twice when I needed her help to look after Iskandar. You made me feel less guilty when I had to ignore Iskandar until he became confused and called you mama.

Norme Ibrahim and Sabki Adnan, my parents, for the never ending support and prayer through my study, for being there for me and for solving my problems, I can't imagine my life without you both.

Nazri Halif, my husband, for being my best friend, for helping the house chores, for the moral support whenever I was down, for the help in my understanding of some physics that I have forgotten, for the contribution in some parts in this thesis and for the never ending arguments especially over the time we had to spend between our work and Iskandar.

Iskandar, my son who came to this world when I started my PhD and is four years old when this thesis is submitted. I love you!

TABLE OF CONTENTS

List of Figures

List of symbols

a	Interatomic distance
K and K'	Dirac points
H	Hamiltonian
R	Position of carbon atom
ξ	Wavefunction
k	Wave-vector
t	Hopping energy of electrons
π and π^*	Valence and conduction bands
$f(k)$	Wave-vector dependent factor
V_F	Fermi velocity
E_F	Fermi energy
E_D	Dirac energy
ΔE	Energy shift
q	Momentum
I	Intensity
λ	Wavelength
d	Distance between lattice plane
θ	Angle of incidence of X-ray with the lattice plane
h	Planck's constant
c	Speed of light
I_t	STM tunneling current
v_s	STM bias voltage

Chapter 1

Introduction

1.1 Graphene

Carbon is known to be one of the most abundant elements in the universe by mass. Even before carbon was identified as an element, a substance, graphite, was discovered and named by Abraham Gotlob Werner in 1594. The word *graphite* is from Greek word *grafo*, meaning 'to draw or to write' because it was being used in pencils at the time. It was first recognized as an element in 1789 when Antoine Laurent de Lavoisier proposed to name it *carbon* which came from the Latin word *carbo*, meaning 'charcoal'.

Since then, carbon has proved a fascinating and essential element studied in many different research areas because of its capability to bond with other elements and form a wide range of organic compounds. In addition there is great interest in elemental carbon since it can form several different allotropes. The two most well known allotropes are diamond and graphite. Interestingly, in recent decades, several more forms of pure carbon have been discovered such as fullerenes, carbon nanotubes and graphene. It is even more interesting that all these recently discovered allotropes are not three-dimensional (3D). Fullerenes are zero-

dimensional, carbon nanotube is one-dimensional and graphene is two-dimensional. Amongst these three allotropes, graphene has been theoretically studied for more than sixty years (Wallace, 1947; McClure, 1956; Slonczewski & Weiss, 1958) and has now become the focus of a rapidly growing community of researchers since its isolation in 2004 by Novoselov and Geim (Novoselov et al., 2004; Novoselov et al., 2005) for which they were awarded a Nobel Prize in Physics in 2010 for the discovery.

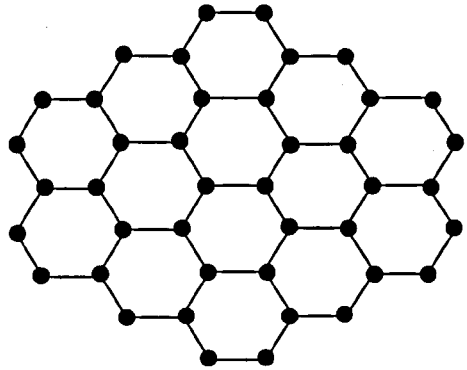

Figure 1.1: A graphene sheet with a honeycomb structure; carbon atoms are arranged in regular hexagons.

More than 70 years ago, Landau argued that a 2D material could not exist, since it would be thermodynamically unstable (Landau, 1937). However the isolation of graphene has proven that a 2D material cannot only exhibit high quality of electronic properties but can also large in coverage and extremely strong. The name graphene is given to a 2D layer of sp^2-bonded carbon atoms which form a honeycomb structure of fused benzene rings. These basic sheets are the building blocks of other graphitic materials such as carbon nanotubes. When several layers of 2D graphene layers are stacked and stabilised by van der Waals forces, graphite is formed. This is no longer 2D but should be considered a bulk, or 3D material. This raises the question of how many graphene layers are needed to form graphite. Based on the electronic structure of graphene, it is possible to distinguish different

types of graphene; single-, double- and few-layer, which consists of 3 to 5 layers of graphene. Graphene stacks that form films thicker than 5 layers are commonly considered to be graphite. A single layer graphene with honeycomb structure is shown in Figure 1.1.

1.2 Remarkable properties of graphene

Graphene has become so popular in nanotechnology because of its electronic properties which opens many doors for new research and potential applications. One advantage of graphene is the ambipolar electric field effect whereby charge carriers (electrons and holes) can be regulated using a gate for concentrations up to 10^{13} cm^{-2}. The mobilities of the charge carriers is very high and can surpass 200000 $cm^2V^{-1}s^{-1}$ (Castro et al., 2010). This high quality gives rise to the quantum Hall effect (QHE) that can be observed in graphene even at room temperature (Novoselov et al., 2007). Charge carriers in graphene are described by the Dirac equation and the interaction of carriers with the honeycomb lattice give rise to new quasiparticles with an effective speed of 10^6 $m^{-1}s^{-1}$ at low energies (Geim & Novoselov, 2007). These quasiparticles are also known as Dirac Fermions.

Graphene also has the complete absence of backscattering for certain models of disorder, a properly related to the Klein paradox. The Klein paradox refers to a counterintuitive process of perfect tunneling of relativistic electrons through arbitrarily high and wide barriers (Geim & Novoselov, 2007). Since the concept of the experiment may be readily implemented in graphene, this has stimulated research on weak and strong localization effects in disordered graphene. The superior properties put graphene a promising candidate for electronics due to minimal resistance which allow high-power and high-speed, fast-switching transistors, replacing analogue devices. There are many other reasons that generate so much interest in graphene. Other than electronic transport (Geim & Novoselov,

2007; Moroszov et al., 2008; Chen et al., 2008) and thermal conductivity (Balandin et al., 2008), other graphene properties have also been explored such as mechanical properties (Lee et al., 2008) and optical behavior (Nair et al., 2008).

1.3 Graphene isolation, growth and detection

The simplest method of graphene isolation is known as mechanical exfoliation or cleavage, which produces high quality monolayers and multilayers. An alternative, chemical exfoliation involves chemical reduction of graphene oxide (Stankovich et al., 2007; Eda et al., 2008). This process involves chemical conversion from graphite to graphene oxide and then to reduced graphene oxide. Even though the mechanical exfoliation is simple, graphene isolated by this method has the highest quality.

Many researchers have started to grow graphene on metal surfaces to acquire graphene in large coverage, particularly for electronic applications. One method which was once considered a very good approach to graphene growth is graphitization of SiC surfaces (Berger et al., 2004; Berger et al., 2006), because it produces graphene sheets on an insulating substrate. However the graphene formed on SiC is difficult to release and transfer. Accordingly, work on graphene growth has expanded rapidly since it becomes more challenging and interesting to produce graphene over large area with the highest quality possible and capability to be released and transferred. This has resulted in extensive studies of the growth of graphene on transition metal substrates such as Ru, Ni, Pd, Rh, Ir or Cu (Sutter et al., 2009; Reina et al., 2009; Pollard et al., 2009; Mattevi et al., 2011). Interestingly, there are several different approaches to graphene growth. Growth processes include the exposure to carbon containing gases (Obraztsov, 2007; Yu et al., 2008; Reina et al., 2009; Kim et al., 2009), converting carbon-containing adsorbates (Pollard et al., 2009), decomposition of molecules (Perdigao et al., 2011) and growth

from solid carbon sources (Sun et al., 2010). It is predicted that methods in graphene will continue to develop rapidly. Most recent research has successfully grown graphene from food, insects and wastes on Cu foils (Ruan et al., 2011).

In conjunction with the expansion of work on graphene growth, there has been great progress on the characterization of graphene layers. Raman spectroscopy, optical microscopy and transmission electron microscopy (TEM) are valuable tools that are capable to distinguishing graphene layers. Visualization of graphene using optical microscopy (Blake et al., 2007) by relating the different contrast with number of graphene layer is the quickest and simplest way to distinguish graphene but the images can be difficult to interpret. TEM is a powerful technique to distinguish graphene layers but requires the transfer of graphene sheets to the TEM grid. In fact, one early application of graphene is as a near-transparent TEM grid. In addition, TEM can be used to study structure and grain boundaries of graphene (Huang et al., 2011). Raman spectroscopy is the most powerful tool to characterize graphene layers (Ferrari et al., 2006; Casiraghi et al., 2007; Ferrari et al., 2007; Malard et al., 2009) because of its capability to give precise information about the graphene layer thickness and most importantly, it is non-destructive.

1.4 Thesis motivations and outlines

Graphene growth on Ni has stimulated great interest from researchers due to the ease of release-transfer process through sacrificial Ni films. To grow graphene, Ni thin films need to be exposed to carbon sources. In this thesis a study to characterize graphene growth on Ni films using various methods, such as converting carbon-containing adsorbates, exposure to carbon containing gas in particular, propylene and decomposition of C_{60} is reported. Even though graphene growth by exposure to propylene has been probed before (Grüneis et al., 2009;

Dedkov et al., 2008), the emphasis in this thesis is on polycrystalline surfaces and on transferred graphene, and is carried out to reduce the defect density in order to achieve high quality graphene. Apart from the growth, this thesis describes Raman spectroscopy of graphene. Also described is a study of PTCDI molecules on graphene. This is relevant to the use of graphene as a substrate for surface enhanced Raman scattering (SERS) study for adsorbed molecules (Jung et al., 2010), also known as graphene enhanced Raman scattering (GERS). This thesis outline is given below:

Chapter 2: Graphene - this chapter provides an introduction to graphene structure and properties in term of the tight binding model, stacking and vibrational properties. Also discussed is Raman spectroscopy and Raman scattering of graphene, which are important for graphene characterization.

Chapter 3: Experimental Techniques - this chapter concentrates on the specific instruments and procedures used in the experiments. The instruments are described in several subsections such as graphene growth, characterization of graphene-terminated Ni, transfer of graphene and characterization of graphene on SiO_2.

Chapter 4: Graphene Growth on Ni - This chapter discusses the graphene transfer method we have developed and the vacuum systems we used to deposit Ni thin films. The main focus of this chapter is divided into two sections; graphene growth without the intentional introduction of carbon, and secondly the intentional introduction of carbon.

Chapter 5: Monolayer Graphene Growth on Ni Films using CVD - This chapter may be viewed as a continuation of work in Chapter 4 and describes graphene growth by exposing Ni films to propylene. In this chapter the reduction of defects in graphene by fine-tuning specific parameters in the growth process is described.

Chapter 6: Graphene Formation by Decomposition of C_{60} - In this chapter the growth of graphene from the intentional inclusion of the fullerene, C_{60}, is discussed. Two methods of C_{60} decomposition are investigated; buried C_{60} under a Ni film and C_{60} sublimed on top of a Ni film.

Chapter 7: Graphene Enhanced Raman Scattering (GERS) of PTCDI – In this chapter the GERS effect is studied by investigating the enhanced Raman scattering of PTCDI adsorbed molecules on epitaxial and exfoliated graphene.

Chapter 8: Conclusions - This is the final chapter which summarizes and concludes the works carried out in the above chapters. It also includes viewpoints for future work.

Chapter 2

Graphene

2.1 Introduction

This chapter gives an overview of the 2-dimensional graphene lattice which is constructed from carbon-carbon bonds. The structure of graphene leads to its interesting electronic properties with the most significant contribution arising from the band formed by π electrons which will be explained within the tight-binding model. This chapter will also include a discussion of graphene stacking, as epitaxial graphene often contains multiple layers of graphene. It is important to understand the vibrational properties of graphene since the phonon dispersion provides the basis for understanding Raman scattering of graphene which is widely used to characterize graphene layers. Raman spectroscopy can give information on the quality and the number of layers of graphene. The techniques used in the analysis of the Raman spectrum of graphene will also be discussed in this chapter. The discussion of graphene growth will be focused on the use of transition metal substrates as this is the main topic of this thesis.

2.2 Graphene structure

Graphene is made up of carbon atoms. A carbon atom has six electrons occupying the $1s^2$, $2s^2$ and $2p^2$ atomic orbitals as shown in Figure 2.1. The $1s^2$ electrons are strongly bonded and are known as core electrons. The four remaining electrons as in $2s^2$ and $2p^2$ are valence electrons. The binding energy is the energy required to extract electrons from their atomic orbitals. The difference in binding energies between the 2s and 2p states is much smaller than the absolute binding energy. This means that the wavefunctions of the four electrons can be mixed when forming bonds with other atoms. This process is called hybridization and the resulting states are shown in Figure 2.2. The mixed wavefunctions result in three states, also known as sp^2 states which reside in xy-plane. The sp^2 states combine or overlap to form covalent σ bonds with their nearest neighbours, with an angle of 120° between bonds, which leads to the hexagonal lattice structure of graphene. σ bonds are strong and lead to the mechanical strength of graphene.

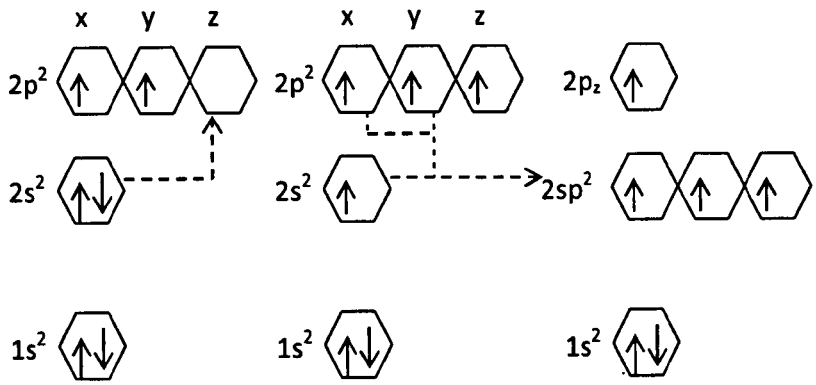

Figure 2.1: sp^2 hybridization in graphene showing the occupation of the atomic orbitals in the hybridization process.

The remaining electron occupies the $2p_z$ orbital (see Figure 2.1) which is oriented along the z-axis. Electrons in these states combine to form π bonds. The orbital structure after the hybridization is displayed in Figure 2.2 showing σ orbitals which are depicted in blue while the π orbitals depicted in red.

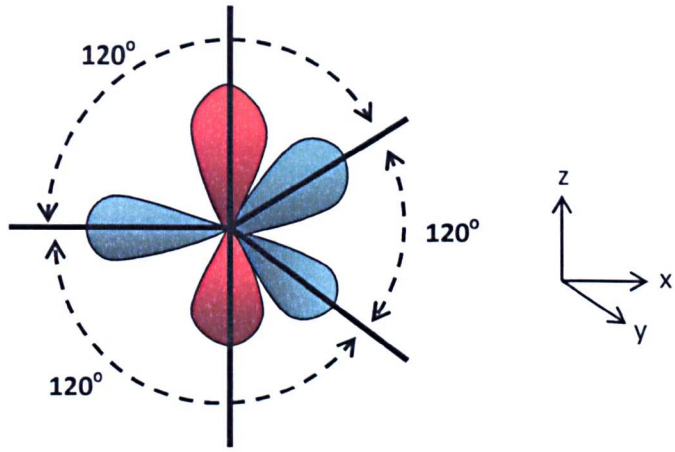

Figure 2.2: Hybridization process between two carbon atoms showing bonding of the σ orbitals (blue) and π orbitals (red).

The graphene structure is referred to as a honeycomb lattice structure since the carbon atoms sit at the vertices of regular hexagons. From a crystallographic point of view, the honeycomb lattice of graphene cannot be described by a Bravais lattice but it has to be represented by a triangular lattice with two atoms per unit cell. These two atoms are often referred to as A and B atoms as shown in Figure 2.3. The unit cell of the lattice is a rhomboid and can be defined by the lattice vectors as in equation (2.1) (Rao et al., 2009).

$$a_1 = \sqrt{3}ae_x \qquad \text{and} \qquad a_2 = \frac{\sqrt{3}}{2}ae_x + \frac{3}{2}ae_y \qquad (2.1)$$

Where a = 1.42 Å is the interatomic distance. Figure 2.3 shows the lattice and the reciprocal lattice, within the first Brillouin zone of graphene. The reciprocal lattice is also a triangular lattice with its lattice vectors b_1 and b_2 given in equation (2.2) Rao et al., 2009).

$$b_1 = \frac{2\pi}{\sqrt{3}a}\left(e_x - \frac{1}{\sqrt{3}}e_y\right) \qquad \text{and} \qquad b_2 = \frac{4\pi}{3a}e_y \qquad (2.2)$$

The first Brillouin zone as shown in Figure 2.3(b) (Castro Neto et al., 2009) has two inequivalent corners, K and K', and the other four corners can be obtained from an elementary translation of the form $nb_1 + mb_2$ where n and m are integers. K and K' are named Dirac points and their positions in momentum space are given in equation (2.3) (Castro Neto et al., 2009). The significance of K and K' will be discussed in the next section.

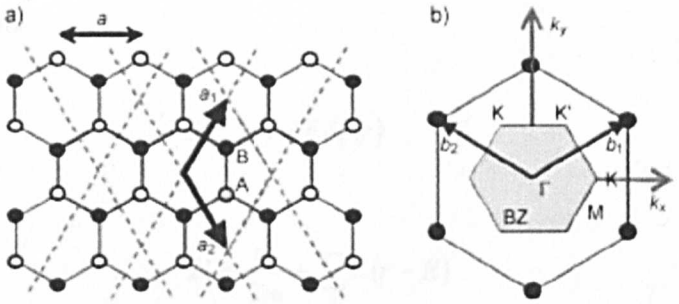

Figure 2.3: (a) Graphene lattice with a_1 and a_2 are the unit vectors. (b) Reciprocal lattice of graphene with the shaded hexagon as the first Brillouin zone. b_1 and b_2 are reciprocal lattice vectors (Rao et al., 2009).

$$K = \left(\frac{2\pi}{3a} \quad , \quad \frac{2\pi}{3\sqrt{3}a}\right) \text{ and } K' = \left(\frac{2\pi}{3a} \quad , \quad -\frac{2\pi}{3\sqrt{3}a}\right) \qquad (2.3)$$

2.3 Tight-binding model of graphene

The dispersion relation of the π electrons in graphene is described by the tight-binding model. The first tight-binding description of graphene was suggested by Wallace in 1947 with consideration of the nearest- and next nearest-neighbor interaction for the graphene p_z orbitals. However he neglected the overlap between wave functions centered at different atoms. Saito et al., 1998, has given a better tight-binding approximation which considers the overlap between the basis

functions, but includes only interactions between nearest neighbors within the graphene sheet. So Reich et al., 2002, derived an improved tight-binding electronic dispersion by including up to third-nearest-neighbor interaction and overlap.

From the Schrodinger equation in equation (2.4), we can calculate the eigenvalues E, of the allowed states. H in equation (2.5) is the single-electron Hamiltonian of graphene where the first term describes the kinetic energy of electron. The second term describes the periodic potential with R as the position of the carbon atom.

$$H\xi_k(r) = E\xi_k(r) \tag{2.4}$$

$$H = \frac{p^2}{2m} + \sum_R V(r-R) \tag{2.5}$$

Since graphene has two atoms per unit cell, the following assumption in equation (2.6) describes the wavefunction $\xi_k(r)$ where $\Phi_A^k(r)$ and $\Phi_B^k(r)$ are the Bloch functions. Both Ψ_A and Ψ_B in equation (2.6) depend on the wave vector k.

$$\xi_k(r) = \Psi_A\Phi_A^k(r) + \Psi_B\Phi_B^k(r) \tag{2.6}$$

Where

$$\Phi_{A/B}^k(r) = \frac{1}{\sqrt{N}}\sum_{R_{A/B}}^{N} e^{ikR_{A/B}}\chi(r-R_{A/B}) \tag{2.7}$$

$R_{A/B}$ indicates the position of the atom A or B, $\chi(r-R_{A/B})$ are Wannier functions localized at the A/B atoms and the $e^{ikR_{A/B}}$ contains the periodicity of the lattice. In order to obtain the energy eigenvalues, the wavefunction is substituted in the Schrodinger equation.

Assuming that electrons can hop to both nearest- and next-nearest-neighbor atoms but neglecting overlap integrals for larger spacings, the tight-binding Hamiltonian is given by equation (2.8) (Castro Neto et al., 2009),

$$H = -t \sum_{\langle i,j \rangle,\sigma} \left(a^{\dagger}_{\sigma,i} b_{\sigma,j} + H.c. \right) - t' \sum_{\langle\langle i,j \rangle\rangle,\sigma} \left(a^{\dagger}_{\sigma,i} a_{\sigma,j} + b^{\dagger}_{\sigma,i} b_{\sigma,j} + H.c. \right) \qquad (2.8)$$

Where i and j refer to sublattices A and B respectively. The lattice vector $a_{\sigma,i}$ annihilates and $a^{*}_{\sigma,i}$ creates an electron with spin σ up and down on site R_i on sublattice A, and similarly for the annihilation and creation of electron on site R_j on sublatice B. t is the hopping energy of electrons to the nearest-neighbor which refers to the hopping between different sublattices. t' is the hopping energy to the next-nearest-neighbor which refers to hopping in the same sublattice. H.c. is the Hermition conjugate.

From the tight binding Hamiltonian given in equation (2.8), the dispersion relation is (Wallace, 1947),

$$E_{\pm} = \pm t\sqrt{3 + f(k)} - t' f(k) \qquad (2.9)$$

Where the plus sign refers to the upper band, π^* and minus refers to the lower band, π and $f(k)$ is the wave-vector dependent factor given by,

$$f(k) = \sqrt{1 + 4\cos^2\left(k_x \frac{\sqrt{3}a}{2}\right) + 4\cos\left(k_x \frac{\sqrt{3}a}{2}\right)\cos\left(k_y \frac{3a}{2}\right)} \qquad (2.10)$$

Figure 2.4 below shows a close up at the band structure close to one of the Dirac point, at K or K' point in the Brillouin Zone. The dispersion energy, E can be obtained by expanding equation (2.10) around the Dirac point with $k = K + q$ and $|q| \leq \frac{2\pi}{a}$.

$$E_{\pm}(q) = \pm\hbar v_F \mid q \mid + O\left[\left(\frac{q}{K}\right)^2\right] \tag{2.11}$$

$$v_F = \frac{3ta}{2} = 1\times10^6 ms^{-1} \tag{2.12}$$

where v_F is the Fermi velocity and q is the momentum measured relative to the Dirac points.

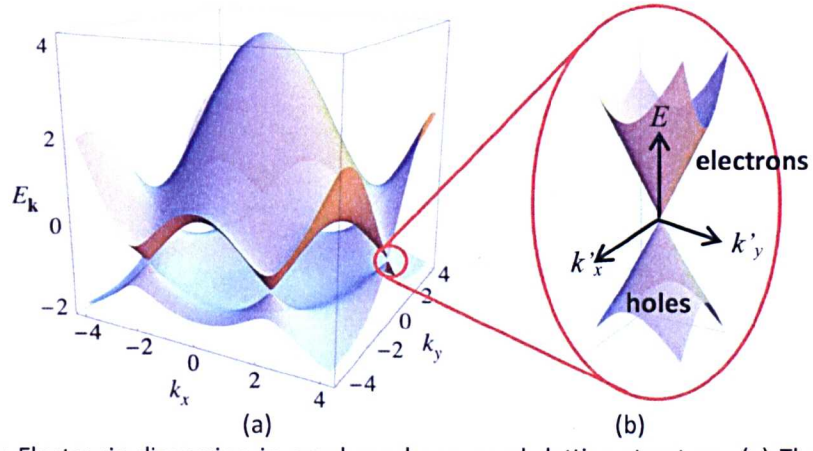

Figure 2.4: Electronic dispersion in graphene honeycomb lattice structure. (a) The energy spectrum (is in units of t) for finite values of t and t', with t=2.7eV and t'= -0.2t. (b) close up of the energy band close to one of the Dirac points (K and K') (Castro Neto et al., 2009).

One of the most important characteristics of the energy dispersion of graphene is that it has a linear energy-momentum relationship with the crossing of the valence (π band) and conduction (π^* band) bands at q = 0, which is symmetrically below and above the Fermi energy E_F = 0. Accordingly the fermi level is in between the π and π^* bands at the crossing point. Considering that a perfect graphene sheet has only one electron per carbon atom in the π level, zero excitation energy is needed to excite an electron from the very top of π band to the very bottom of π^*. Therefore graphene is a zero band-gap semiconductor, with a linear energy dispersion for electrons in the conduction band and holes in the valence

band as a result of two atoms per unit cell in graphene. This gives graphene metallic properties and characteristics of a gapless semiconductor.

2.4 Graphene stacks

Graphene refers to single 2D plane of carbon atoms network, as explained beforehand. Double layer graphene is a stack of two single layers, few layer graphene is a stack of 3 to 5 layers, graphite is a stack of more graphene layers on top of each other.

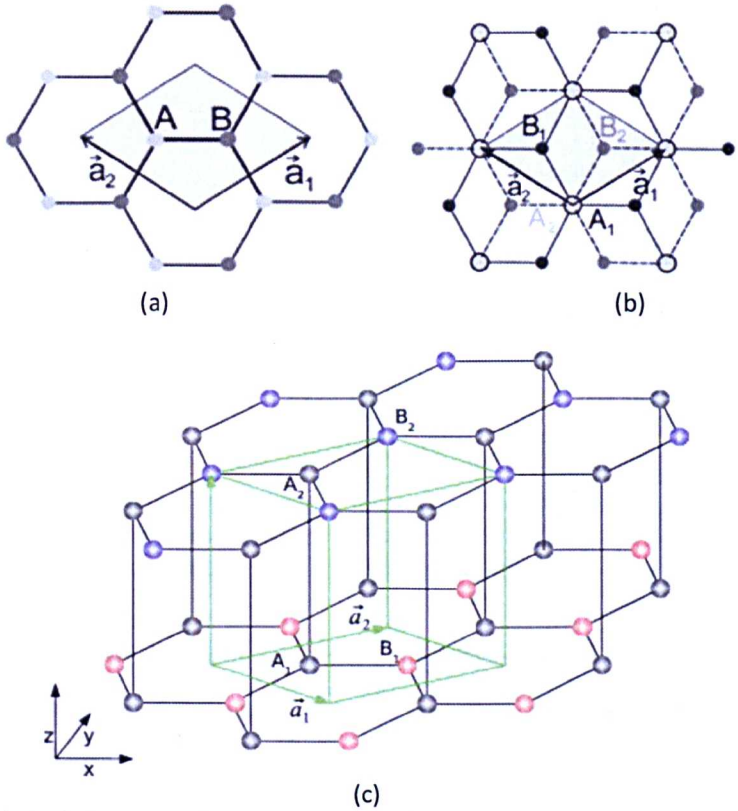

Figure 2.5: (a) single layer graphene with atom A (light grey dot) and atom B (dark grey dot) (b) double layer graphene with atom A_2 on top of atom A_1 (grey circle), atom B_1 (dark grey dot) and atom B_2 (black dot) (c) 3-dimension unit cell of double layer (Malard et al., 2009; Goncharuk & Smrčka, 2010).

Double layer graphene consists of two overlapping sheets (sheet 1 and sheet 2) arranged in Bernal stacking, where the atoms in a sheet are arranged relative to in-plane position. The distance between sheets is 3.37 Å (Goncharuk & Smrčka, 2010). The first network in sheet 1 can be represented by atoms A_1 and B_1, while the second network in sheet 2 can be represented by atoms A_2 and B_2. Therefore bilayer graphene has four atoms per unit cell. As shown in Figure 2.5 (b) and (c), atom A_1 is overlapping with atom A_2, however atom B_1 is placed underneath the vacant center of the above hexagon, while atom B_2 is placed above the vacant center of the underlying hexagon. For instance, two overlapping layers oriented in such a way that the atoms of the honeycomb structure of one layer are directly above one half of the atoms in the neighboring layer (Guinea et al., 2007).

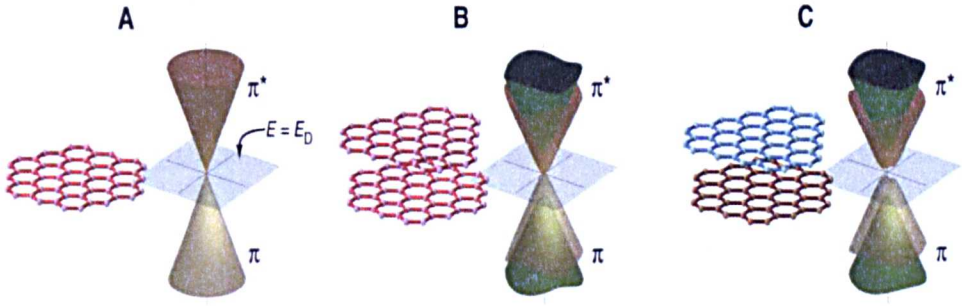

Figure 2.6: Electronic structure of (A) a single layer, (B) symmetric double layer, and (C) asymmetric double layer of graphene. The energy bands depend only on in-plane momentum because the electrons are restricted to motion in a two dimensional plane. The Dirac crossing points are at Dirac energy, E_D (Ohta et al., 2006).

This double layer graphene has a combination of two atoms per unit cells from two planes making four atoms into consideration. This causes a change in band structure whereas additional bands, such π and π^* states are formed in each valley split by interlayer (A-B) coupling, and two lower energy bands, as illustrated in Figure 2.6. For the case of asymmetric double layer graphene, the energy gap between π and π^* states is increased at the Dirac point due to the symmetry breaking with the Fermi energy residing within the gap. This gives rise to the

transition from semimetal to insulator. If this symmetry breaking could be controlled externally, the electronic conductivity would change through this transition, suggesting that a switch with a thickness of two atomic layers could be constructed (Ohta et al., 2006).

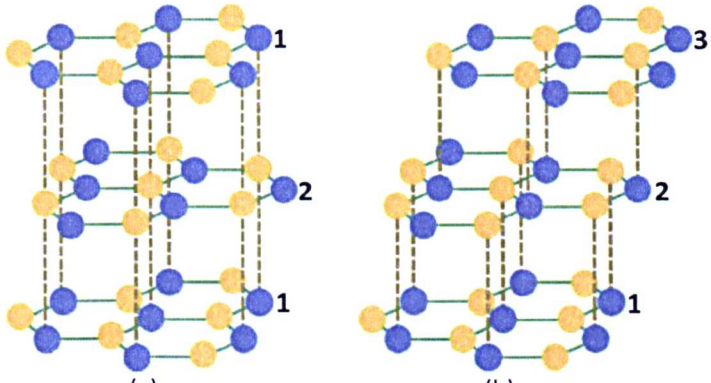

Figure 2.7: Lattice structure of tri-layer graphene with (a) 1 2 1 stacking and (b) 1 2 3 stacking sequence. The yellow and blue dots represent carbon atoms in the 1 and 2 sublattices of the graphene honeycomb structure (Lui et al., 2011)

Bernal stacking (described above) has a stacking order 1 2 1 2 and so on, is the most common and stable structure of graphite. Another stable crystallographic configuration is 1 2 3 stacking order as shown in Figure 2.7. Stacking order of 1 2 1 is commonly used to describe exfoliated graphene because of its thermodynamically stablility. Interestingly, recent study shows that 1 2 1 stacked tri-layer graphene is a semimetal with an electrically tunable band overlap, while 1 2 3 stacked tri-layer is predicted to be a semiconductor with a tunable band gap (Lui et al., 2011). The 1 2 3 stacking can be represented by rhombohedral stacking. When the stacking arrangement of many layers of graphene is not in a discernible order and relative orientation of the network changed, it is called turbostratic graphite. The characterization of graphene and graphite using Raman spectroscopy shows that turbostratic graphite has a quite similar Raman band shape and Raman shift to the Raman spectrum of graphene. The Raman characteristics of turbostratic graphite

will be further detailed in section 2.6.3. The formation of turbostratic graphite has been problematic in graphene growth and it is often neglected.

2.5 Vibrational properties of graphene

Atoms in a uniform solid material interact with their neighbours so that atoms do not vibrate independently. The vibrational energies of molecules can be considered as quantum harmonic oscillators since the energies are quantized. Phonons may be considered as quanta of vibrational energy in periodic solids at a collective vibrational mode which can accept energy only in discrete amounts. Phonon properties determine many of the thermal and mechanical processes in a crystal.

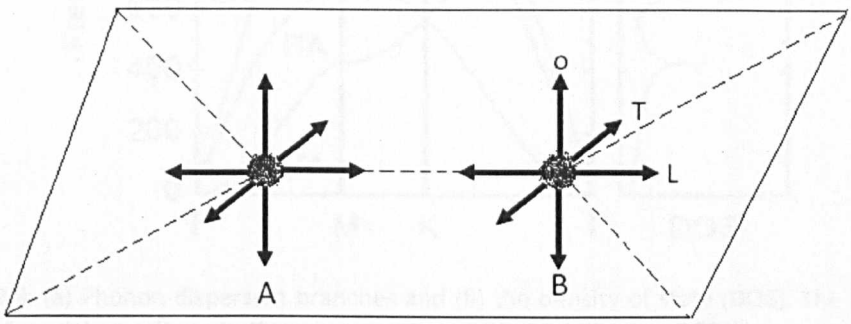

Figure 2.8: Atomic motions of atoms in graphene gives rise to 6 coordinates of phonon branches

In graphene, the phonon dispersion may be directly investigated using Raman spectroscopy, and this information is often used to characterize graphene layers. The crucial aspect to consider is the Brillouin zone (shown in Figure 2.3 previously) as it describes the wave-vector dependence energy of phonons. Since the unit cell of graphene consists of two carbon atoms, A and B, it gives rise to 6 coordinates of phonon branches as shown in Figure 2.8. The 6 phonon branches can be divided into three acoustic branches (A) which are in-phase and three anti-phase

optical branches (O). Both in-phase and anti-phase refer to relative motion of two carbon atoms in reciprocal lattice; in which in-phase is the motion of carbon atoms in the same direction while anti-phase is in opposite direction. Each of the vibrations can be in-plane (i) or perpendicular to the graphene plane, known as out-of-plane (o). The modes of the branches are associated with atomic motions in the direction of the carbon-carbon direction, longitudinal (L) and transverse (T).

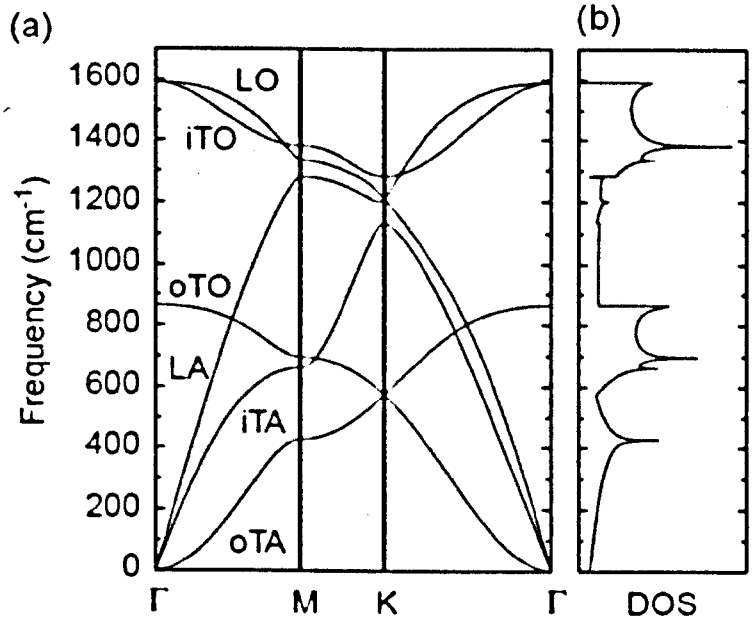

Figure 2.9: (a) Phonon dispersion branches and (b) the density of state (DOS). The *k*-space regions from (a) contribute to the strong peaks in DOS (Malard et al., 2009).

The six phonon dispersion curves can be represented by iTO, oTO, LO, iTA, oTA and LA as shown in Figure 2.9. The three phonon dispersion branches of graphene represented by out-of plane transverse modes (oTA), in-plane transverse modes (iTA) and in-plane longitudinal modes (LA) correspond to the acoustic modes at the Γ point of the Brillouin zone. The iTA and LA modes have a linear dispersion around the Γ point while oTA shows a q^2 energy dispersion from the D_{6h} point-group symmetry of graphene (Malard et al., 2009).

The optical modes are shown in the remaining three branches, which correspond to one out-of plane mode (oTO) and two in-plane modes (iTO and LO). The in-plane iTO and LO modes are degenerate at the Γ point, and correspond to the vibrations of the sublattice A against the sublattice B. According to group theory, the degenerate zone-center LO and iTO phonon modes belong to the two dimensional E_{2g} symmetry and are Raman active (Malard et al., 2009). The linear crossings at oTA/oTO and the LA/LO modes at the K-point are also a consequence of the D_{6h} point-group symmetry. The LA/LO crossing at the K point gives rise to a doubly degenerate phonon with E' symmetry (Jiang et al., 2005).

For instance, the regions of the Brillouin Zone in which the Raman bands are observed are at the Γ, K and K' points (see Brillouin zone in Figure 2.3). The vibrational modes at these points contribute to the Raman bands of graphene, observed as D, G, D' and 2D bands (see 2.6.2). Raman active vibrational modes of graphene will be further detailed in section 2.6.2.

2.6 Raman spectroscopy

Raman spectroscopy is based on the Raman effect, which is the change in light wavelength that occurs when a light beam is scattered by a material. The effect was discovered in 1928 by Sir Chandrasekhara Venkata Raman and named after him. He was awarded a Nobel Prize in Physics in 1930 for the discovery. Raman spectroscopy is widely used in chemical characterization because it is essentially a non-destructive tool and can give detailed information about a specific material.

The measured Raman frequency shifts can give information on the composition of a material. In addition, changes in the frequency of the Raman band can give information related to the strain or stress of a material. The polarisation, width and intensity of the Raman band can also provide useful information, for

example on the crystal symmetry and orientation, the quality of crystal and the amount of material (Ferraro et al., 2003).

Commonly, when a material is irradiated by a monochromatic beam of radiation, there will be an interaction where the atoms in the material can be perturbed by the radiation. The beam can then be absorbed, diffracted, reflected or scattered. The most interesting component from this is the incident beam scattering, which can be elastic or inelastic. Most of the photons are scattered elastically and this process is known as Raleigh scattering. The remaining scattered photons are inelastically scattered corresponding to the Raman effect.

2.6.1 Raman scattering

Raman spectroscopy provides information about the vibrational states of a material, that is its phonon spectrum. The following explanations will therefore focus on the interaction of an incident beam of light with phonons. As mentioned earlier, most of the incident beam of electromagnetic radiation is elastically scattered and is of little interest in this context. The inelastically scattered radiation at longer wavelengths (lower photon energy) than the incident beam is known as Stokes-shifted and arises due to excitation of phonons.

It is also possible to observe inelastically scattered radiation corresponding to the adsorption of a phonon, and this signal, which has higher photon energy than the incident beam is called the anti-Stokes line. As shown in the diagram in Figure 2.10, when a beam of light traverses a material of a chemical compound, most of the transmitted light (final intensity, I_f) has the same wavelength as the incident light (incident intensity, I_i), but a small part of the light (scattered intensity, I_s) has different wavelength, and is inelastically scattered, contributing to the Stokes and anti-Stokes signals. The wavelength shift of these lines provides the basis of Raman

spectroscopy and may be interpreted in terms of the vibrational spectrum of a material and related to chemical information.

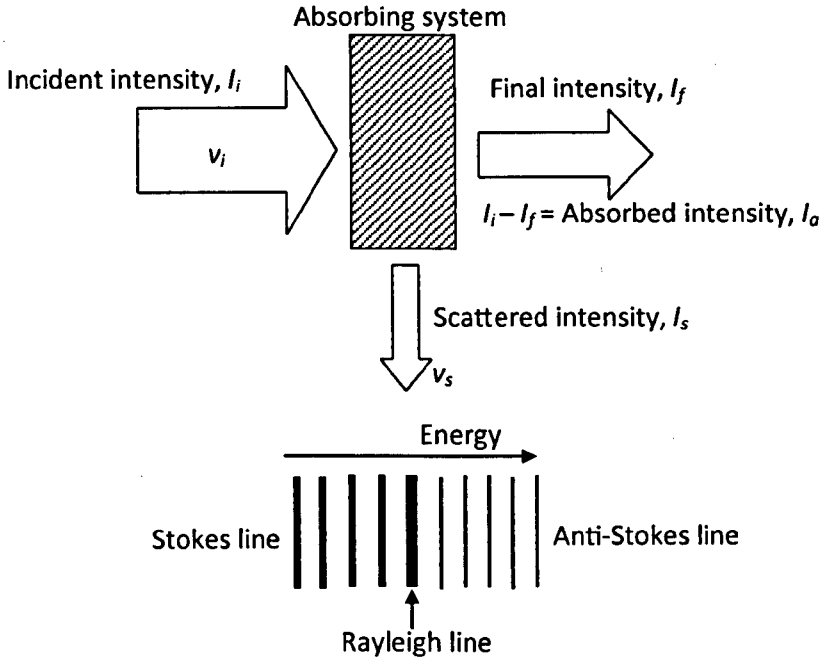

Figure 2.10: Interaction between incident beam and a material which contribute to Stokes and anti-Stokes signal. v_i is incident frequency and v_s is scattered frequency.

The energy shift (ΔE_m) can be calculated by equation (2.12) below with h is the Planck's constant, c is the speed of light, λ_i and λ_s are the wavelengths of the incoming and the scattering photons respectively.

$$\Delta E = hv_i - hv_s = h_c\left(\frac{1}{\lambda_i} - \frac{1}{\lambda_s}\right) \qquad (2.12)$$

As shown in Figure 2.11 for Stokes interaction, the emission of a vibrational excitation occurs when electrons in a low energy state (v = 0) are excited to a virtual state, and then relax to a higher energy vibrational state, emitting a photon. In this case, the scattered photons have less energy than the incident photons (λ_0 - λ_v).

However, in anti-Stokes scattering, the electrons are scattered in a molecule in a higher energy vibrational state, and then relaxes to a lower energy vibrational level (v = 0). This means that the scattered photons have more energy ($\lambda_0 + \lambda_v$) and shorter wavelength than the incident photons. It is expected that both Stokes and anti-Stokes Raman scattering will occur simultaneously, with the Stokes scattering intensity generally greatly exceeding the anti-Stokes scattering intensity. This is due to the fact that there are more molecules in the lower vibrational states.

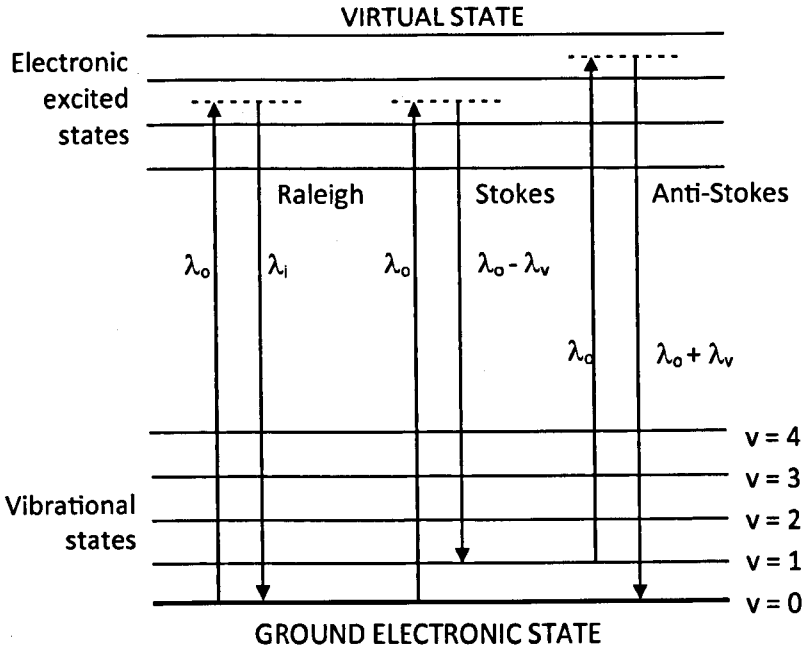

Figure 2.11: Conservation of energy for Raman scattering; Stokes and anti-Stokes.

Another scattering process is resonance Raman scattering which is often used to increase the intensity of the Raman scattered signal. Many molecules adsorb laser beam energy and strongly fluoresce, disturbing the Raman signal. This problem often occurs when UV lasers are used, but under certain conditions, some molecules can generate strong Raman scattering instead of fluorescence. This effect is known as resonance Raman scattering.

In resonance Raman scattering, the energy of the incoming laser is adjusted such that it coincides with an electronic transition of the molecule. Since it involves an electronic transition, the intensity of the Raman signal is enhanced by a few orders of magnitude. This is the main advantage of the resonance Raman over the non-resonance or traditional Raman spectroscopy. Non-resonance and resonance Raman scattering can be distinguished by varying the incident photons energy λ_0. In resonance Raman scattering, the incident beam energy is higher than the non-resonance Raman scattering, as shown in Figure 2.12 below and gives rise to a more intense Raman line.

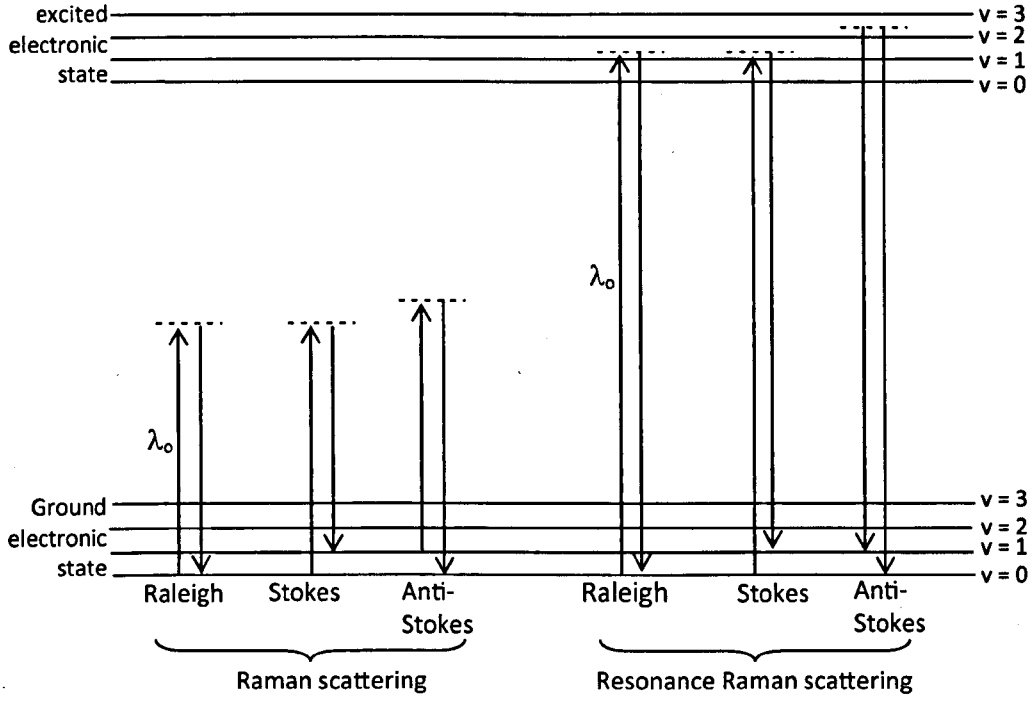

Figure 2.12: Resonance and non-resonance Raman scattering.

For a molecule with many vibrational modes, resonance-Raman spectroscopy allows a few vibrational modes to be observed at a time. This process reduces the signal complexity which leads to easier identification of some unknown peaks. Resonance-Raman also can give structural identification of a substance or

compound. Since the intensity of Raman peaks can be increased, the resonance Raman spectra can be generated with much lower sample concentration as compared with conventional Raman spectroscopy. One disadvantage of resonance-Raman is the increased fluourescence and risk of photodegradation of the sample.

2.6.2. Raman scattering of graphene

Before a thorough discussion on Raman scattering of graphene, it is useful to present the main features in the Raman spectrum of graphene as in Figure 2.13 which has three dominant bands; D, G and 2D bands. The Raman band at 1580 cm^{-1} was initially found in graphite and named as G band. The G band is the only band arising from a normal first-order Raman scattering process. It is associated with the doubly degenerate phonon mode (iTO and LO) at the Brillouin zone center.

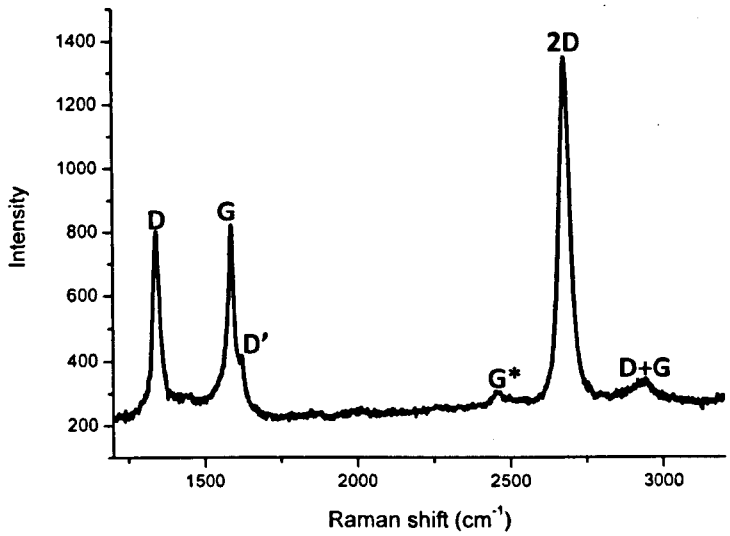

Figure 2.13: Raman spectrum of a defected graphene showing main features of a Raman spectrum.

The G band Raman shift and its line shape reflects doping and strain level of graphene. The Raman shift of the G band does not vary with the incident photon energy, but is sensitive to charge transfer. This can provide information about the doping or impurities within a graphene sample (Malard et al., 2009). For instance,

negatively charged impurities in graphene correlated to electron transfer, will cause a downshift of the G band because of the decrease in the energy of the phonon vibration. The G band can also be an indicator of the number of graphene layer, as it gives rise to a slight frequency upshift (<10 cm^{-1}) but its shape does not change with the number of layers (Charlier et al., 2008). But the G band intensity increases with an increasing number of graphene layers from one to four layers (Graf et al., 2007). The first order G band process is illustrated in Figure 2.14(a).

There is a second-order resonance mode involving a iTO phonon near the K point and one defect which generates a frequency lower than the G band. This band, at 1350 cm^{-1}, is named the D band due to the interaction of photons with defects and disordered sp^2 carbons in rings (Ferrari, 2007). The D band mechanism requires the interaction of a photon with the K and K' points (refer Figure 2.3) and the process is called an inter-valley mechanism as represented in Figure 2.14(b). The D band is commonly observed at the graphene edges, however there are a few more defect types which also need to be considered such as stacking order, crystalline size and structural disorder which relate to vacancies, topological defects, bond distortion and sp^3 conversion. The D band is sensitive to the laser beam energy as it relatively upshifted with higher laser beam energy.

Similar to the D band, a band named the 2D band, also known as the G' band, originates from a second-order process involving two iTO phonons near the K point. The 2D band is approximately twice the D band frequency due to the two iTO phonons which contribute to the inter-valley process. This process connects states close to inequivalent K and K' points in the first Brillouin zone and is illustrated in Figure 2.14(c). Accordingly the 2D band frequency is observed at 2700 cm^{-1}. Unlike the D band, the 2D band is not associated with any kind of defects or disorder. In the case of the 2D band, the scattering of holes also needs to be considered. Holes can be scattered by phonon with wavevector $+q$ and in this case, the electron and hole scattering leads to a triple resonant process (Figure 2.14(d)), which contributes to the intensity of the 2D band (Malard et al., 2009).

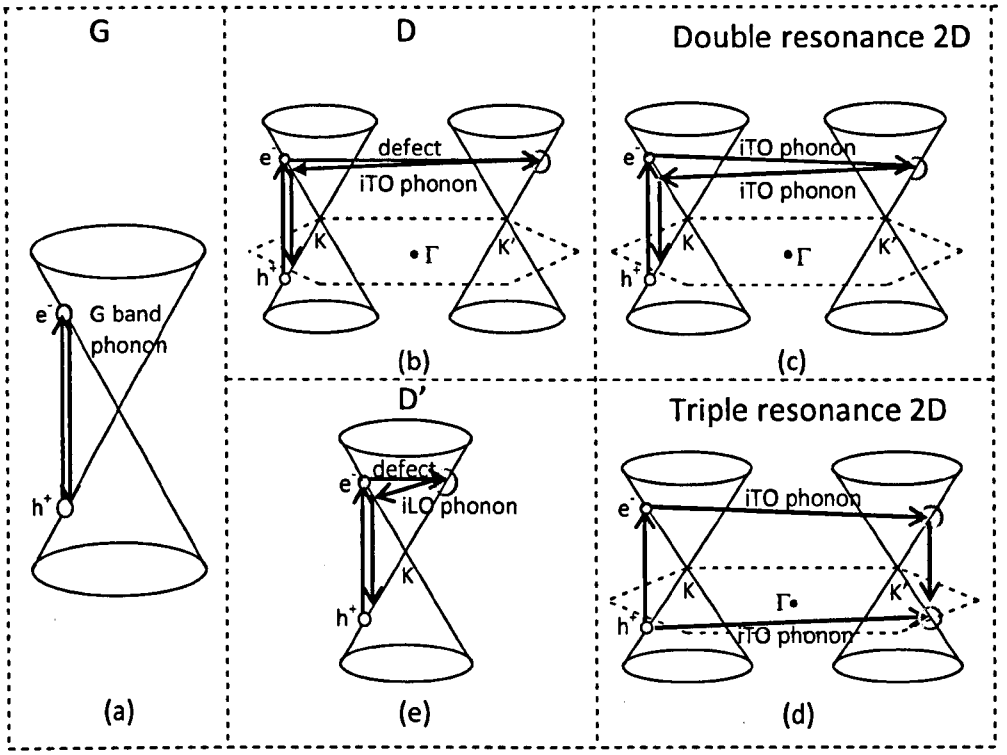

Figure 2.14: Schematic representation of the electronic scattering mechanisms at the K and K' points in the reciprocal space. (a) First-order G band process, (b) inter-valley process for D band, (c) inter-valley double resonance process of 2D band, (d) inter-valley triple resonance of 2D band process, (e) intra-valley process for the D' band. Resonance points are shown as open circles near the K point and K' point (Malard et al., 2009).

Another band which typically has a frequency at 1620 cm^{-1}, arises through a double-resonance process as a result of an intra-valley scattering mechanism in a transition occurs between states within the cone around the K point or the K' point and it is illustrated in Figure 2.14(e). This is a weak defect and disorder induced band (similar to D band) and involves the scattering of the iLO phonon near the Γ point. This band is observed as a shoulder next to the G band and is referred to as the D' band. Since the intensity of the D' band is much weaker than the D band, it is not widely used in the characterization of graphene.

A weak band is observed at ~2450cm^{-1}, called the G* band. This is a second order band which involves one iTO and one LA phonon in a double resonance Raman mode (Malard et al., 2009; Maultzsch et al., 2004). The frequency of the G* band can be influenced by the laser excitation energy in which the G* band is downshifted with higher laser energy (Mafra et al., 2007). A peak observed at 2950 cm^{-1} is denoted as D+G band which is also a second order band and a disorder-induced band (Livneh et al, 2002). Both G* and D+G bands are very weak and typically not of interest for graphene characterization as will be extensively discussed in the following chapters.

2.6.3. Characterization of graphene using Raman spectroscopy

In the characterization of graphene, the determination of the number of layers using Raman spectroscopy is quite straightforward. However a careful investigation requires the functional fitting of Raman bands. Previous work on graphene characterization (Ferrari et al., 2006; Ferrari, 2007; Charlier et al., 2008) has demonstrated that the intensity and full width half maximum (FWHM) of the Raman bands may be used to distinguish the number of graphene layer. Typically Lorentzian functions are used to determine the number of peaks that contribute to graphene Raman spectrum as well as their FWHM and intensity. The intensity ratios can be calculated from the data obtained.

Typically, the criteria between single and multilayer graphene can be differentiated by the ratio of 2D band to G band (I_{2D}/I_G) and FWHM of the 2D band. Characteristically, single layer shows a single sharp 2D band which is about two times more intense than the G band (Ferrari et al., 2006). In this work, graphene is considered as single layer graphene if $I_{2D}/I_G>1$ and the FWHM of the 2D band is less

than 35 cm^{-1}. Therefore a double or multi-layer graphene should has the intensity ratio of $I_{2D}/I_G<1$ and FWHM of the 2D band more than 35 cm^{-1}.

The Raman spectra of double layer and few-layer graphene have apparent differences as compared with the spectrum of a single layer. The Raman spectra of single and double layer graphene (Figure 2.15) show a different intensity and Raman shift for the G and 2D bands. 2D band of double layer graphene consists of four components $2D_{1B}$, $2D_{1A}$, $2D_{2A}$ and $2D_{2B}$, two of which, $2D_{1A}$ and $2D_{2A}$ have higher relative intensities than the other two (Ferrari et al., 2006). The G band for double layer graphene shifts towards lower wave numbers (2 - 3 cm^{-1}) and has a slightly higher intensity (I_{2D}/I_G around 0.8 – 1). These characteristics are due to the different electron dispersion energy in double layer graphene as shown beforehand in Figure 2.6(B) and (C). For the π band (or valence band) consists of two components represented by π_1 and π_2 while the π^* band (or conduction band) has another two components, π_1^* and π_2^* at the K and K' points respectively. These four different components contribute to the four band components ($2D_{1B}$, $2D_{1A}$, $2D_{2A}$ and $2D_{2B}$) (Ferrari, 2007; Malard et al., 2009).

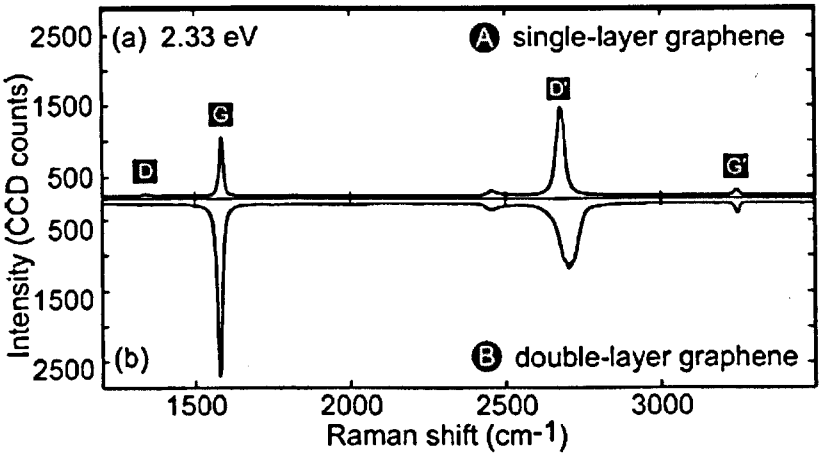

Figure 2.15: Raman spectra of single and bilayer graphene (D' is also known as 2D peak) (Graf et al., 2007).

A significant difference between the Raman spectrum of graphene and graphite is, the decrease of the relative intensity of the lower wave number $2D_1$

components (Ferrari et al., 2006), thus producing a shoulder on the 2D band as the number of layers is increased. This peak evolves into only two peak components in bulk graphite. Raman spectroscopy can differentiate a single layer from a bilayer and from few layers (3 to 5 layers), however it is very difficult to distinguish more than five layer graphene from bulk graphite.

Another issue which needs to be considered is turbostratic graphite which typically has a sharp single 2D peak similar to single layer graphene but has a FWHM of ~50 cm^{-1} and is up-shifted of 20 cm^{-1} (Ferrari et al., 2006). The similarity of the Raman 2D band of a turbostratic graphite to that of single layer graphene provides direct experimental evidence that a turbostratic graphite can be considered as a 2 dimensional graphite (Pimenta et al., 2007). The D band in turbostratic graphite is a first order band (Lespade et al., 1084), unlike the D band in graphene which is second order.

2.7 Surface Enhanced Raman Spectroscopy (SERS)

SERS is an enhancement of the Raman signal, typically by a few orders of magnitude, due to absorption of molecules on a rough metal surface. SERS is used to investigate the vibrational properties of adsorbed molecules yielding structural information of the molecule and its local interactions. This surface-sensitive technique also uniquely identifies molecules and allows the detection of single molecules.

SERS was first reported by Martin Fleischman and coworkers in 1974 with pyridine molecules adsorbed onto an electrochemically roughened silver surface (Fleischman, 1974). The mechanisms which contribute to the SERS effect are still debated, however the two most discussed theories are the electromagnetic (Jeanmarie & Van Duyne, 1977) and chemical (Albrecht & Creighton, 1977) enhancement theories. It is currently accepted that the electromagnetic enhancement typically provides the highest contribution to SERS.

The electromagnetic enhancement arises from the presence of localised plasmons on a rough surface. Surface plasmons are electromagnetic waves that propagate along the surface parallel to the metal or dielectric interface and are generated when the incident light excites the electron gas of the metal. When a molecule is placed in the proximity of the plasmons, it experiences a locally enhanced electromagnetic field which produces an increase in Raman scattering.

Chemical enhancement involves charge transfer between the chemisorbed species and a metal surface. In this case enhancement arises due to charge transfer which causes the polarizability of the molecules to increase due to the larger separation between positive and negative charge in the molecule/substrate. This causes the cross-section for Raman scattering to increase (Ling et al., 2010). Chemical enhancement has been shown to have a higher cross section for the first monolayer of adsorbed molecules than the second layer (Otto, 1992). However the chemical enhancement is generally less than a factor of 10, much lower than electromagnetic enhancement.

2.7.1 SERS of Graphene

Graphene is found to be a very good substrate for enhancing the Raman signal of adsorbed molecules. Ling et al., 2010 found that Raman signal of adsorbed molecules on single layer graphene are stronger than on SiO_2/Si and multilayer graphene substrates. The Raman signal is found to decrease with increasing thickness of graphene; graphite itself is a very poor Raman substrate for Raman enhancement (Jung et al., 2010). Most studies have attributed the enhancement of the Raman signal to the charge transfer (chemical mechanism) between graphene and the molecules (Ling & Zhang, 2010; Ling et al., 2010; Ling & Zhang, 2011).

One of the important characteristics in chemical enhancement is the short range, wherein the chemical enhancement follows a power law decay, d^{-10} (where d is the distance between the probe molecule and the substrate) (Mrozek & Otto,

1990). These authors pointed out that the chemical enhancement can be achieved when the molecule is close enough to the substrate, which is consistent with the first layer effect.

One of the advantages of the measurement of Raman spectra of adsorbed molecules on graphene is that fluorescence and luminescence are quenched (Xie et al., 2009). Jung et al., 2010, reported that the quenching rate increases as the spacing between the molecule center to graphene plane decreases. To calculate the Raman enhancement factor, the intensity signals of adsorbed molecules on a SiO_2 substrate are compared with the signals for adsorbed molecules on graphene.

2.8 Graphene growth

The growth of graphene over large areas is currently a rapidly developing area of research. There are two methods of graphene growth on metal surfaces to be considered. The first method is segregation of bulk-dissolve carbon to the surface, which involves carbon doped samples, which in other words, contains carbon impurities. The second method is the surface decomposition of carbon-containing molecules, eg. hydrocarbon gases like ethylene, propene or methane are used. This method has been explored experimentally since 1974 for example by Shelton who found that at an equilibrium temperature carbon would dissolve into nickel producing a condensed graphitic monolayer at the nickel surface, known as graphene nowadays (Shelton et al., 1974; Fujita et al., 1995).

Both graphene growth methods are capable to produce single or multilayer graphene by controlling the growth parameters, such as temperature. Graphene grown by both methods were initially observed using Auger Electron Spectroscopy (AES) (Grant & Haas, 1970; Shelton et al., 1974) and low energy electron diffraction (LEED) (Bonzel & Krebs, 1980). Graphene had also been detected using angle-resolved photoelectron spectroscopy and the results were compared with ab-inito

calculations which have shown a nearly parabolic band which is assigned to the $2p_z$ orbitals of the carbon atom (Himpsel et al., 1982).

There has been remarkable progress in the growth of graphene on SiC. The growth process involves annealing the SiC at very high temperature (~1100°C) resulting in the desorption of the top Si layers leaving a few layers of graphene at the surface. The number of graphene layers could be controlled by fine tuning the growth parameters such as annealing temperature and time. The quality of the graphene as well as the number of layers could be controlled using different SiC crystal orientations for the growth; as an example the C-terminated surface produces few layers (2 to 5 layers) with low electron mobility, while the Si-terminated surface produces several layers with higher electron mobility (de Heer et al., 2007). One drawback of graphene grown on SiC is that it is almost impossible to release-transfer graphene from the surface. However, there is a way to grow and release-transfer graphene grown on transition metal substrates, such as Ru, Ni, Pd, Rh, Ir or Cu. It is also the most promising and readily accessible route of reasonably high quality graphene.

Graphene growth on polycrystalline ruthenium (Ru) (Sutter et al., 2009) shows that, after an appropriate treatment, Ru thin films have a columnar structure with highly aligned grains exposing flat (001) surface facets. A uniform monolayer of graphene covers the entire Ru surface. Sutter et al., 2009 found that monocrystalline graphene domains are coherent across a large number of substrate grains, hence the size of graphene domains is not limited by grain boundaries in the metal template. It has been found that graphene on Ru has zigzag edges and ripples which related to a 10 x 10 reconstruction (Vazquez de Parga et al., 2008). The inhomogeneous graphene coverage is caused by locally enhanced carbon segregation at stacking domain boundaries of metal emphasizing the importance of the suppression of local segregation (Yoshii et al., 2011).

Research on graphene growth on Ni has attracted considerable interest because of the high quality of graphene sheets produced and the easy release-

transfer process through the use of sacrificial Ni films. Many methods has been explored using Ni films since 1974 (Shelton et al., 1974; Fujita et al., 1995; Campagnoli & Tossati, 1989) with the exposure to carbon containing gasses (Obraztsov, 2007; Yu et al., 2008; Reina et al., 2009; Kim et al., 2009) such as methane at atmospheric pressure. Graphene could also be formed without exposing Ni films to carbon containing gas, instead by immersing Ni films in an organic solvent. One interesting outcome found by Pollard et al., is that monolayer graphene could be formed without intentional introduction of an additional carbon source and might come unintentionally from exposure to atmosphere or during Ni film deposition in a commercial evaporator (Pollard et al., 2009).

A quite similar approach is used to grow graphene on Cu foils and involves heat treatment at low pressure and exposure to carbon-containing gas. Recent research on graphene grown on copper has demonstrated high quality films with uniform single layer coverage. It was demonstrated that graphene grown on 25 μm copper foil could produce more than 95% single layer coverage (Mattevi et al., 2011). Interestingly, copper is reasonably cheap, the growth process is straightforward and it is easily etched in solvents available in most laboratories making the transfer process of graphene over large area readily accessible. Most recently an experiment has been carried out to omit the transfer process by evaporating copper after graphene growth so that the as-grown graphene rests on the dielectric substrate (Ismach et al., 2010).

Progress in graphene growth has led to a new approach to grow monolayer graphene from solid carbon sources. The advantage of the graphene produced using this approach is that it has very low concentration of structural defects however the control of the film thickness, size and location has become a challenge. An experiment to use PMMA as a solid carbon source has shown that graphene layers could be controlled by controlling the PMMA thickness (Sun et al., 2010).

2.8.1 Graphene growth mechanisms

Graphene growth on Ni thin films involves interaction of carbon and Ni surfaces. The process of introducing carbon to a metal is called carburization which is typically used in many processes in industry with the aim to improve surface characteristics, such as surface hardness and resistance. Remarkably this process provides the possibility to synthesize graphene. Many transition metals used as substrates catalyze the formation of graphene. One of the factors determining the graphene growth mechanism is the solubility of carbon in the chosen transition metal. Materials that are known to have low carbon solubility are copper, platinum and iridium but nickel is proven to exhibit high carbon solubility, in which carbon can easily dissolve in Ni.

One important characteristic of Ni is that it can form ordered surface carbide, which is an atomic layer of Ni_2C phase. It can be envisaged that the formation of Ni_2C competes with the growth of graphene. On Ni (111), Ni_2C forms an ordered $\sqrt{39}R16.1°$ x $\sqrt{39}R16.1°$ surface structure which is almost square (Klink et al., 1995). The base unit of the Ni_2C is unmatched with respect to the Ni (111), which is hexagonal. At elevated temperature, the carbon from the Ni_2C dissolves into the Ni bulk and when the sample is cooled, the carbons are driven out to the surface. During this cooling process the carbon solubility of Ni decreases, which causes carbon to expel from the Ni bulk and form graphene at the surface (Lahiri et al., New J. Phys., 2011).

Physisorbtion is known as a physical adsorption process, in which, the process makes the electronic structure of the atom or molecule perturbed. If we consider graphene is physisorbed, we would expect that the distance between graphene and metal surfaces (eg. Ni) is the distance comparable to the layer spacing in bulk graphite, which is ~3.35 Å. From the LEED-1(V) analysis of graphene on Ni (111) (Gamo et al., 1997), it is obtained that the graphene layer on Ni (111), is oriented such that one carbon atom of the unit cell sits on top of a metal atom

(Figure 2.16(a)) (Wintterlin & Bocquet, 2009). It is found that the vertical positions (Figure 2.16(b)) of carbon on Ni are 2.11 Å and 2.16 Å which is shorter than the expected layer spacing for a physisorbed layer (3.35 Å). This suggests that chemical bonds are formed between C and Ni atoms.

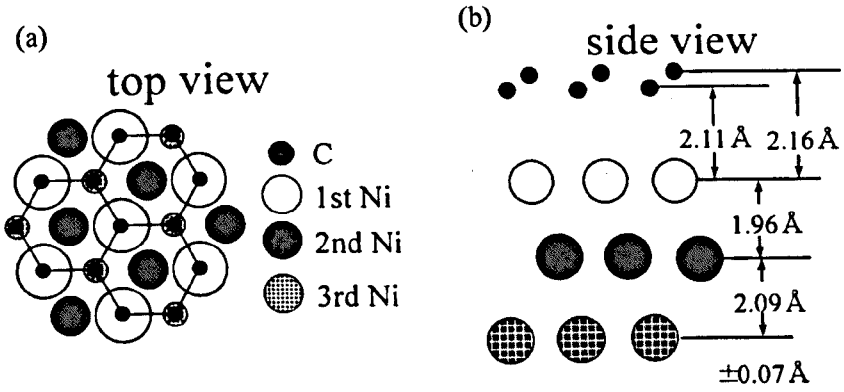

Figure 2.16: The (1×1) structure models of graphene on Ni(111) obtained from LEED-I(V) structure analyses. (a) Top view and (b) side view of the structure. Figure adapted from Gamo et al., 1997.

2.8.2 Defects in graphene

Compared to three dimensional crystals, graphene, due to its dimensionality, has a lower number of types of possible defects. One important defect in graphene is the point defect which comprise of the Stone-Wales defects, single and multiple vacancies, carbon and foreign adatoms, and substitutional impurities (Banhart et al., 2010). For example hexagonal graphene rings can be reconstructed into a nonhexagonal rings and one such arrangement is known as the Stone-Wales (SW) defect. Note that this type of graphene does not involve any removed or added atoms, so the defected structure has the same number of atoms as undefected graphene. In this type of defect, the reconstruction of the graphene rings occurs by in-plane rotation of the C-C bonds, by simultaneously movement of the two involved atoms. The change in the graphene rings is illustrated in Figure 2.17.

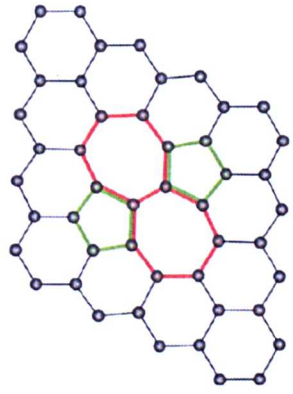

Figure 2.17: Stone-Wales defect structure obtained by DFT calculation (Banhart et al., 2010).

Single and multiple vacancies in graphene correspond to missing lattice carbons, which also transform a perfect graphene lattice structure. Single vacancies only involve one missing carbon atom, which leads to the formation of a dangling bond attaches to a new ring consists of 9 carbon atoms and a neighboring ring with 5 carbon atoms. The example of the single vacancies is shown in Figure 2.18 (a). Double vacancies are generated by coalescence of two single vacancies or by removal of two neighboring atoms, but no dangling bonds are generated. This is due to the formation of two pentagons and one octagon, which is shown in Figure 2.18 (b). Multiple vacancies can be generated from these single and double vacancies which may lead to a more complex arrangement.

Interstitial atoms can only appear in three dimensional crystals. For the case of graphene, the interaction of a carbon adatom with carbon rings in graphene can change the hybridization of the carbon atoms. This leads to a local carbon sp^3-hybridization, which generates two new covalent bonds between the carbon adatoms and the underlying carbon atoms in graphene. If foreign adatoms, which are not carbon interact with graphene, the bonding that occur will depend on the interaction (Banhart, 2009). The interaction leads to weak or strong bonds, which lead to physisorption and chemisorption, respectively.

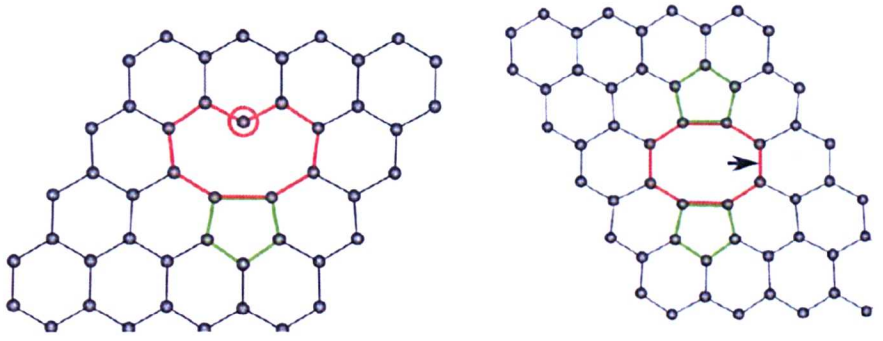

(a) (b)

Figure 2.18: (a) Single vacancy atomic structure with dangling bonds and (b) double vacancy atomic structure consisting two pentagons and one octagons (Banhart et al., 2010).

Another type of defect in graphene, which is one-dimensional is dislocation-like. It is seen as line defect, separating two domains of different lattice orientations. This defects can be considered as a line of reconstructed point defects with or without dangling bonds (Malola et al., 2010; Yazyev & Louie, 2010). Graphene edges is known to be one of the contributor to most defect peak in graphene Raman bands. A well known types of graphene edges are the armchair and the zigzag orientations, which minimizes the number of dangling bonds at the edge. These defective edges develop due to local changes in the reconstruction type or because of the sustained removal of carbon atoms from the edges. The armchair edges can be transformed to the zigzag edges when the carbon atoms are displaced (Girit et al., 2009). The transitional structure can be considered as a defective edge. If hydrogen atoms or other chemical groups interact with the dangling bonds at the graphene edge, that can be considered as disorder, in which the interaction leads to an increasing number of possible defects at the edge. The armchair and the zigzag defects orientation at the graphene edge are shown in Figure 2.19(a) and 2.19(b) below.

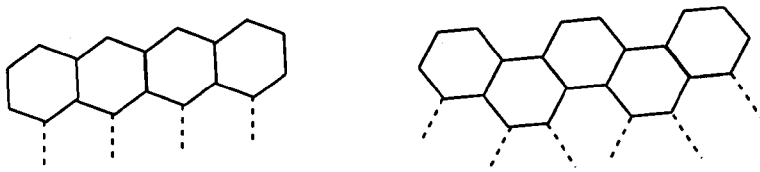

(a) (b)

Figure 2.19: Different defects orientation at the graphene edges (a) armchair edge, (b) zigzag edge.

2.9 Summary

The graphene structure is made up of carbon atoms bonded together by covalent σ bonds and weak π system. In this chapter a discussion of the Brillouin zone of graphene, including the K and K' points which also known as a Dirac point, has been presented. The graphene tight-binding model gives the dispersion relation of π electrons in graphene and lead to the understanding of the band structure of graphene. Single layer graphene is a zero-band gap semiconductor with a linear energy dispersion for electrons in the conduction band (π* band) and holes in the valence band (π band), a result of two atoms per unit cell in graphene.

The networks and stacking of carbon atoms leading to the formation of graphene band gap has also been presented. Understanding the vibrational properties of graphene is important as the phonon dispersion of graphene is of direct relevance to Raman spectroscopy which is used to determine graphene quality and layer number. The graphene phonon branches contribute to the three most prominent bands in graphene Raman spectrum, the D band, G band and 2D band as well as the weaker G* and G+D bands. The characterization of graphene based on its Raman spectrum has been described above. The surface enhanced Raman scattering (SERS) is also described. This chapter has also discussed graphene growth with an overview of the growth on SiC and on transition metals such as Ru, Ni and Cu, including the growth mechanisms and defects.

Chapter 3

Experimental Techniques

3.1 Introduction

This chapter will be focusing on the experimental methods used to grow and characterize graphene on Ni films and the study of the properties of transferred graphene on a SiO_2/Si substrate. To grow graphene on Ni films, firstly a layer of Ni has to be deposited. This process has been performed using two different systems; a standard commercial evaporator and an ultra-high vacuum (UHV) evaporator system. Once Ni thin films are formed, they are annealed and exposed to a carbon source in a UHV system. After graphene layers are formed on Ni films, they are transferred onto a dielectric substrate.

Information on surface morphology and topography of the graphene layer are investigated using optical microscopy, scanning tunneling microscopy (STM) and atomic force microscopy (AFM). The crystal orientation and elements found in our samples are investigated using x-ray diffraction (XRD). The transfer process of graphene involves spin coating of PMMA, deposition of PDMS and Ni etching in $FeCl_3$. Finally optical microscopy and Raman spectroscopy are used to determine the composition, quality and number of layers of the transferred graphene.

3.2 Graphene growth

This section will be describing two different systems used for Ni film deposition; a standard commercial evaporator and an ultra-high vacuum (UHV) evaporator system. The commercial evaporator is using the Edwards Auto 306 vacuum coater. Finally the operation of the graphene growth chamber will be described.

3.2.1 Ni deposition in the Edwards Auto 306 vacuum coater

Ni thin films were deposited on SiO_2/Si substrates using a standard commercial evaporator, the Edwards Auto 306 vacuum coater. The Auto 306 vacuum coater is designed for standard physical vapour deposition under high vacuum. The major components of this system are a pumping system, a baseplate and an electrical system which incorporate the system controller. The system is shown in Figure 3.1. The rotary roughing pump and turbomolecular pump is used to pump the system down to ~1×10^{-7} mbar.

The substrates are placed on a metal surface using magnets and mounted at the top of the bell jar with the substrate surface facing the source. The tungsten crucible containing the Ni source is heated by passing a current through it causing the Ni to evaporate. Once the expected deposition rate is reached, a shutter separating the Ni source from the target substrate is opened to expose the substrate to Ni evaporation. A crystal microbalance and a control unit are used to measure the thickness of the films being deposited. The typical thickness of Ni thin films used in this work is about 100 nm. The deposition rate used is around 0.02 nm/s and the base pressure is 1×10^{-7} mbar. Once the expected thickness is achieved, the shutter is closed and the current flowing to the crucible is reduced and turned off. Films prepared in this manner were then transferred through the atmosphere to the UHV system described below.

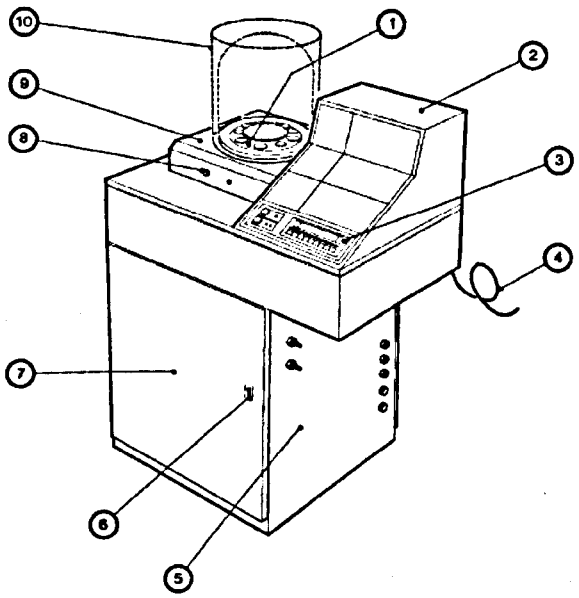

Figure 3.1: The Edwards Auto 306 vacuum coater[1]

3.2.2 Ni film deposition in ultra high vacuum (UHV)

To deposit Ni thin films in our UHV system, a SiO_2/Si substrate is cut with the dimension of about 1 cm x 1 cm and placed on a highly doped silicon strip heater attached to the UHV sample holder which also known as the sample stub, shown in Figure 3.2. A clear arrangement of the substrate on the sample stub is illustrated in the diagram in Figure 3.3. The substrate is placed on a Si strip heater which is on the quartz disc. The Si is heated by flowing current through it via two metal (Ta) chips.

The UHV system has two chambers, one used to deposit Ni films and one to grow graphene. The Ni deposition system is located at the bottom part of the system as shown in Figure 3.4 while the graphene growth is located at the top with both chambers being pumped down by two different ion pumps. The SiO_2/Si substrate is loaded into the system from the load-lock connected to the growth

[1] Figure adapted from the Instruction Manual: Auto 306 Vacuum Coater with Turbomolecular Pumping System, Boc Edwards, E090-03-860, Issue G.

chamber as shown in Figure 3.5. The load lock is pumped to a low pressure using a turbomolecular pump before the sample is introduced. Both chambers have a similar base pressure (1×10^{-9} mbar) and are separated by a valve.

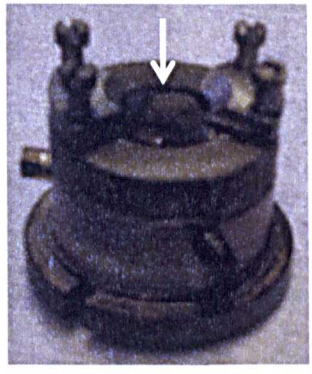

Figure 3.2: Picture of sample holder (also known as sample stub) for the UHV system with sample placed on top of the holder (as pointed by the arrow).

Substrates are outgassed in the top chamber before Ni deposition. The samples are heated by flowing current to the silicon strip heater at the back of the sample holder (Figure 3.2 (b)) at ~500°C. The process will cause the base pressure to rise up to 10^{-7} - 10^{-6} mbar. Typically the sample is left to outgas overnight for about 18 hours before increasing the current slowly until reaching 800°C. The sample then is left to outgas for another hour. The annealing is stopped by reducing the current gradually to zero and the substrate is ready for Ni deposition.

As shown in Figure 3.4, the Ni deposition system consists of an integral tungsten-alumina crucible with Ni wire in it. The base pressure of the chamber is approximately 1×10^{-9} mbar and the deposition rate and thickness are measured by a quartz microbalance. The base pressure of the chamber can rise to 1×10^{-7} mbar during the evaporation. Once the desired evaporation rate is achieved, the sample is turned to face the evaporator. Ni heating is reduced to stop the evaporation and the sample surface turned away when the target thickness has been deposited.

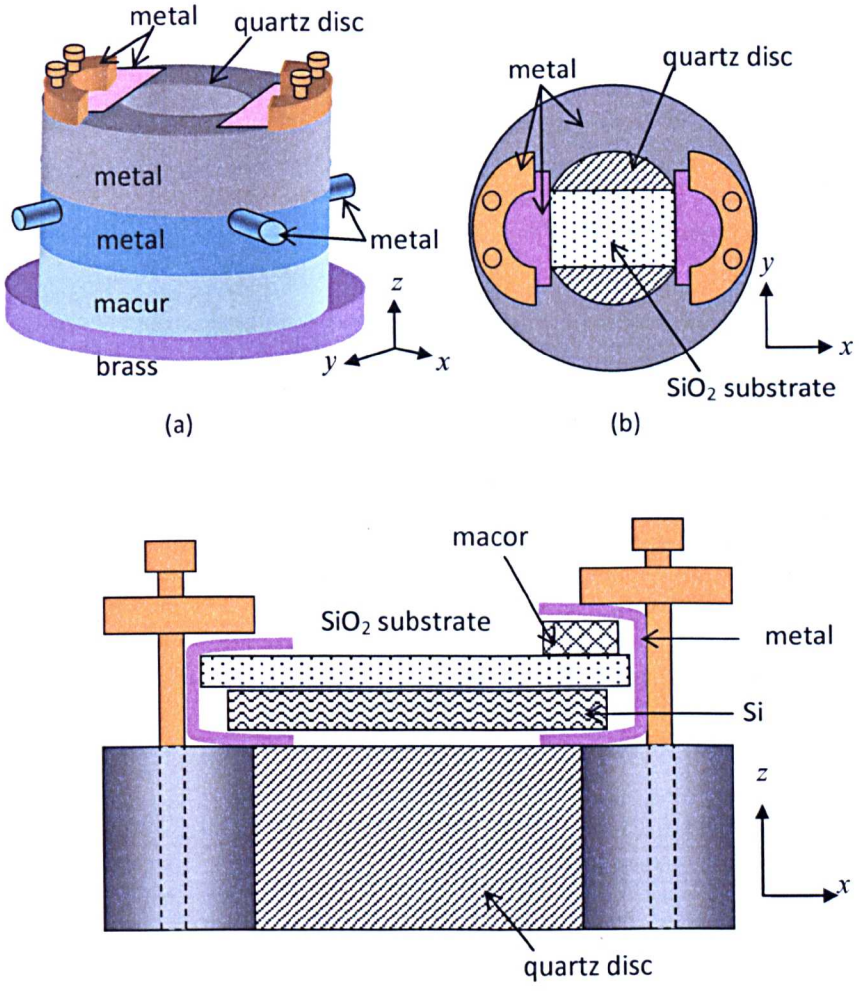

Figure 3.3: Diagram of the UHV sample stub in Figure 3.2. (a) the arrangement of the sample stub in side view. (b) top view showing a sample placed on top of the quartz disc. (c) cross section of the top area of the sample stub showing position of the sample on the sample stub.

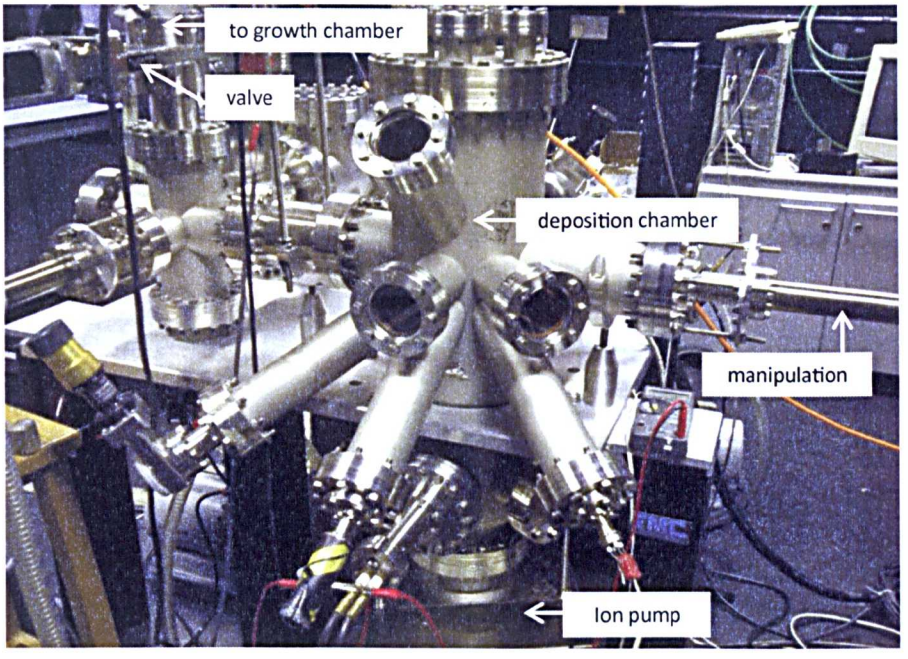

(a)

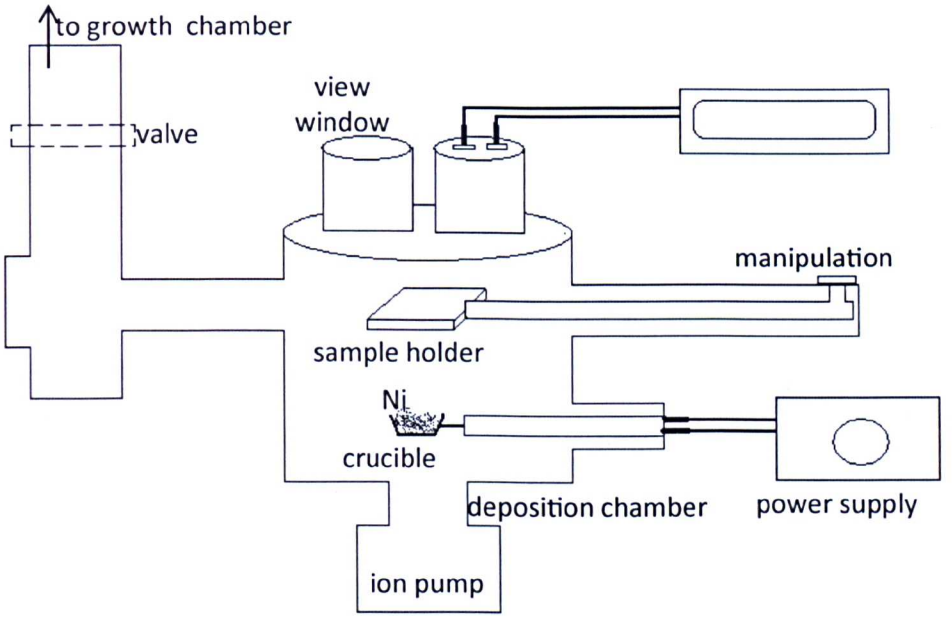

(b)

Figure 3.4: (a) Photo of the UHV Ni deposition chamber (b) Schematic diagram of the Ni deposition system.

3.2.3 Graphene growth chamber

The chamber used for graphene growth is in the same UHV system discussed above (see Figure 3.4) and a more detailed configuration is shown in Figure 3.5. The procedure for graphene growth varies slightly depending on the specific aim of the work. The base pressure of the growth chamber is maintained at around 10^{-9} to 10^{-10} mbar. Usually a Ni film is annealed at a certain temperature between 700°C to 900°C for a specified period of time. The temperature is measured using a pyrometer placed about 30 cm from the sample surface. During the annealing process the internal power supply connection is made by mechanically attaching a lead to the sample using a manipulation arm. For the samples treated with a gas such as propylene, the gas will be introduced into the chamber through a leak valve during the annealing process and the pressure rises to 1×10^{-6} mbar.

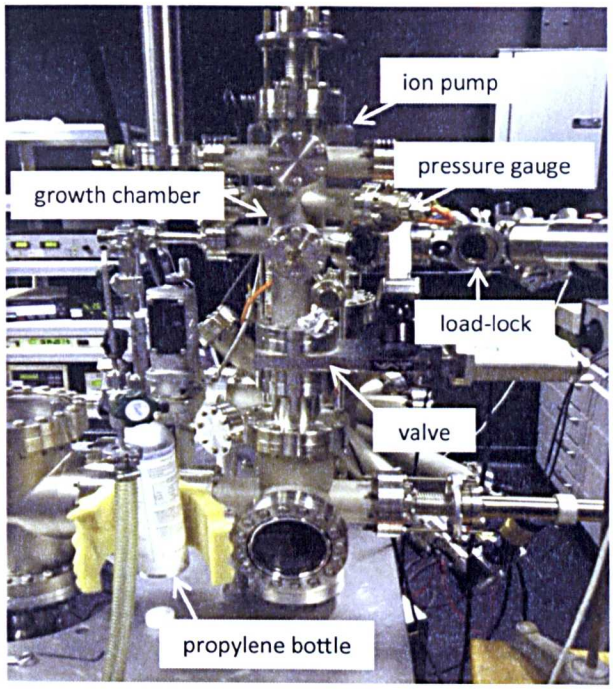

(a)

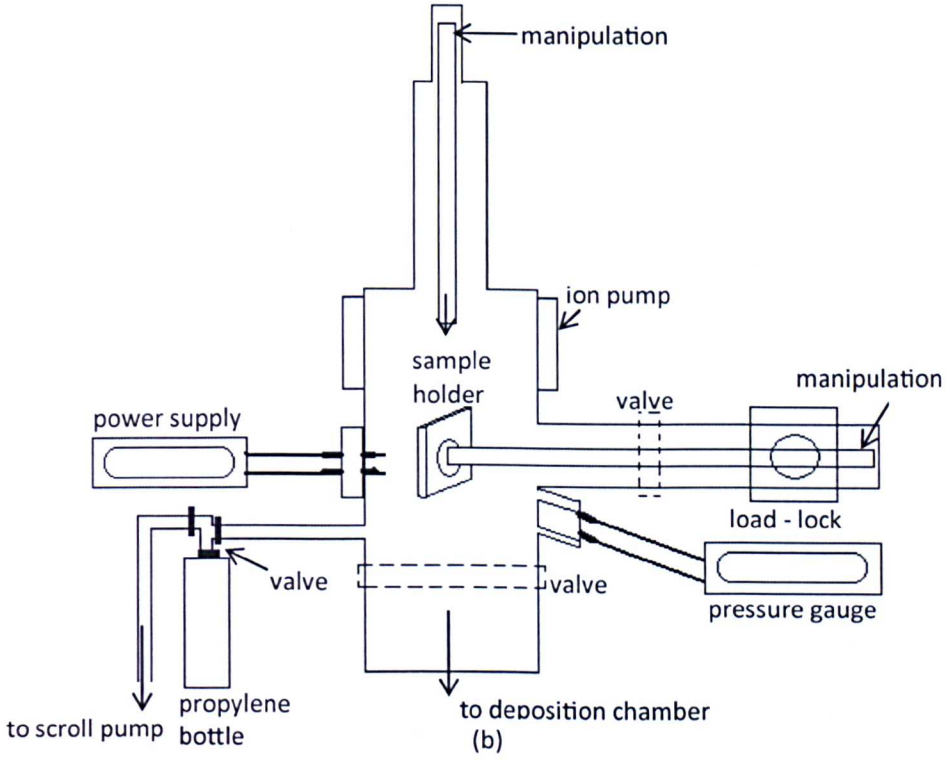

(b)

Figure 3.5: (a) UHV system used for graphene growth (b) schematic diagram of the UHV system for graphene growth.

3.3 Characterization of graphene terminated Ni

Characterization of the graphene terminated Ni samples is performed using several different methods. After the growth process, the quickest and easiest way to observe the surface morphology is by using optical microscopy but a better resolution of the growth morphology and surface topography of graphene can be measured using scanning tunneling microscopy (STM) and atomic force microscopy (AFM). The X-ray diffractometer (XRD) is used to analyze the structure of the Ni films before and after graphene growth. All apparatus used to characterize the graphene terminated Ni will be further detailed in the next section.

3.3.1 Atomic force microscopy (AFM)

The AFM is used to investigate conductive or non-conductive samples on the atomic scale in various environment such as air, ultrahigh vacuum (UHV) and liquids (Ohnesorge & Binnig, 1993). The AFM has a similar concept and design (as shown in Figure 3.6) to the STM. However the tunneling tip that is used in STM is replaced by a force sensing cantilever in AFM. The AFM cantilever has an atomically sharp probe tip at its end, and is typically made of silicon or silicon nitride (Baird et al., 2004).

Figure 3.6 shows the principle of the AFM. The forces between the probe and the sample lead to a deflection of the cantilever which can be measured using an optical deflection system. Both the vertical and lateral deflections of the cantilever can be measured. The optical deflection system operates by reflecting a laser beam off the cantilever. The reflected laser beam strikes a position-sensitive photo-detector using a photodiode device consisting of four segments. The differences between the signals arising from the segments of the photo-detector of signals indicate the position of the laser spot on the detector and thus the angular deflections of the cantilever.

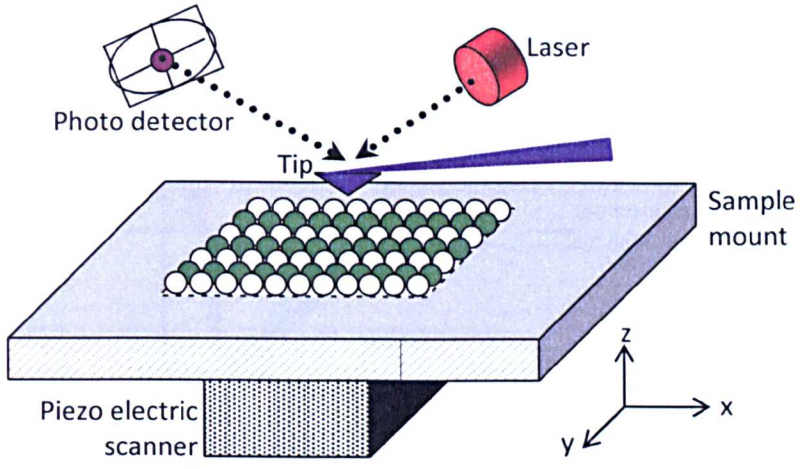

Figure 3.6: The principle of atomic force microscopy with x, y and z piezo movement.

There are three commonly used modes in the AFM operation; contact mode, non-contact mode and the tapping mode. These three modes are differentiated by the nature of forces and the distance between the tip and surface during the scanning process. Basically contact mode is concerned with operation in a regime in which the dominant force arises from repulsive interactions at small tip-sample separations. This mode has the possibility to damage some delicate sample surface. For non-contact mode attractive interactions at larger tip-sample separations are relevant. This mode is very suitable to image soft and fragile samples as the tip does not come into contact with the sample surface. However the images may have lower resolution than the contact mode due to the long range interactions. The tapping mode is a combination of the contact and non-contact modes. Figure 3.7 shows the forces that occur between tip-sample surface including the modes of operation of AFM.

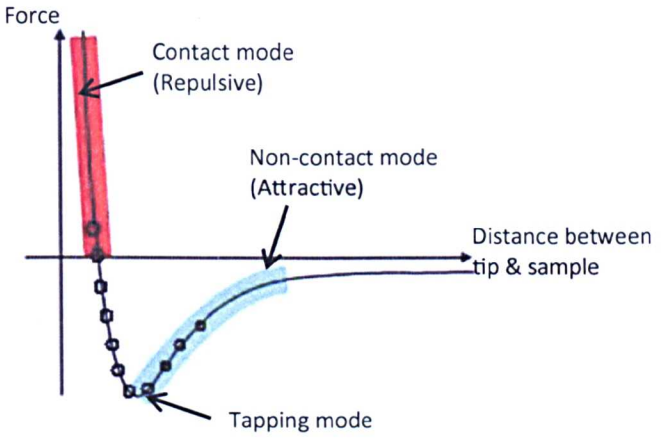

Figure 3.7: AFM force separation curve that shows the AFM mode of operations consisting contact mode (in repulsive regime, marked with red), non-contact mode (in attractive regime, marked with blue) and tapping mode (consist of both regimes, marked with circles).

In this work, tapping mode is used in order to obtain high resolution images and to prevent any possible damage to the graphene layer. In tapping mode the cantilever is very close to the sample surface while oscillating at its resonant frequency. In other words, the cantilever is driven at larger amplitude than in the non-contact mode and as a result, the tip approaches very close to the surface over a small fraction of its oscillation period. This tapping process is meant to improve lateral resolution while avoiding lateral forces which are common in contact mode. The AFM system used in this work is MFP-3D Stand Alone (MFP-3D-SA). It has low coherence light source to eliminate optical interference.

3.3.2 Scanning tunneling microscopy (STM)

STM is used to acquire images of surface topography of graphene and it is one of the important tools used to study graphene. The basic concept of STM is as shown in Figure 3.8. An atomically sharp tip that has been formed by chemical etching or mechanical grinding or cut using a wire cutter is mounted on an x, y, z, transducer which functions as a scanning device. When the tip is brought very near

to a sample a tunnelling current I_t can flow between the tip and the sample when a voltage V_t is applied. As the probe passes over the sample surface, the variations of the tunneling current are translated into an image. The very high resolution of the STM rests on the strong dependence of the tunnel current on the distance between the two tunnel electrodes, that are the metal tip and the scanned surface (Neddermeyer, 1996).

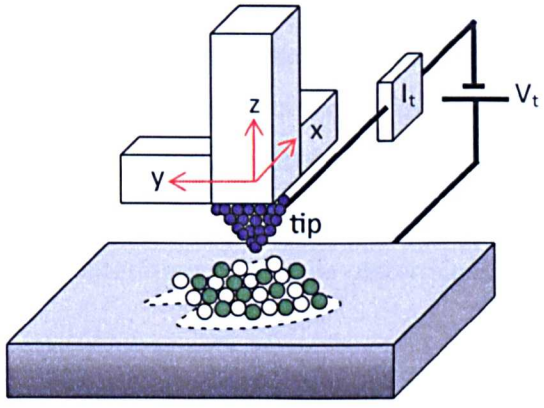

Figure 3.8: A schematic diagram of scanning tunneling microscope (STM).

The STM tip is one of the most crucial components and ideally is atomically sharp to ensure that an image with good atomic resolution can be obtained. The tip is usually made of tungsten or platinum-iridium. Although the concept of STM is simple, there are some problems that arise in its operation such as the precise control of the tip location and movement, control of vibration and making an atomically sharp tip (Baird et al., 2004). One of the drawbacks of STM is that it can only image the electrically conductive samples. This limits its application to the imaging of metals and semiconductors (Giessbl, 2003).

The ambient STM images in this study were acquired using a commercial instrument, supplied by Molecular Imaging/ Agilent. For the STM images acquired in vacuum a commercial Nanograph Systems instrument is used which is housed in the same UHV system as used for graphene growth (see Figure 3.4). In both systems Pt/Ir cut tips are used.

3.3.3 X-ray diffraction (XRD)

Although AFM and STM provide high resolution images of the graphene terminated Ni morphology and topography, neither technique provides information about the crystal structure. X-ray diffraction (XRD) is used to characterize and identify the crystal structure of our samples.

Crystalline structures have periodic lattice which behave like a grating that can diffract waves or electromagnetic radiation with wavelengths of a similar order to the lattice period. X-rays, of interest here, can have wavelengths similar to interatomic spacings, *d*. When the wavelength is close to the lattice of the crystalline structure, X-rays may be scattered coherently by any n^{th} order of parallel lattice plane leading to constructive interference which can be observed as diffraction pattern. The constructive interference can be determined by Bragg's Law as illustrated in Figure 3.9.

From figure 3.9(a), BC + BD = $n\lambda$ where BC = BD, n is an integer determined by the order given and λ is the wavelength of X-ray. This makes 2BC or 2BD equal to $n\lambda$. Figure 3.9(b) shows that BC = $d \sin \theta$ where d is the distance between the lattice planes and θ is the angle of incidence of X-ray with the lattice plane, which gives the Bragg's Law in equation (3.1).

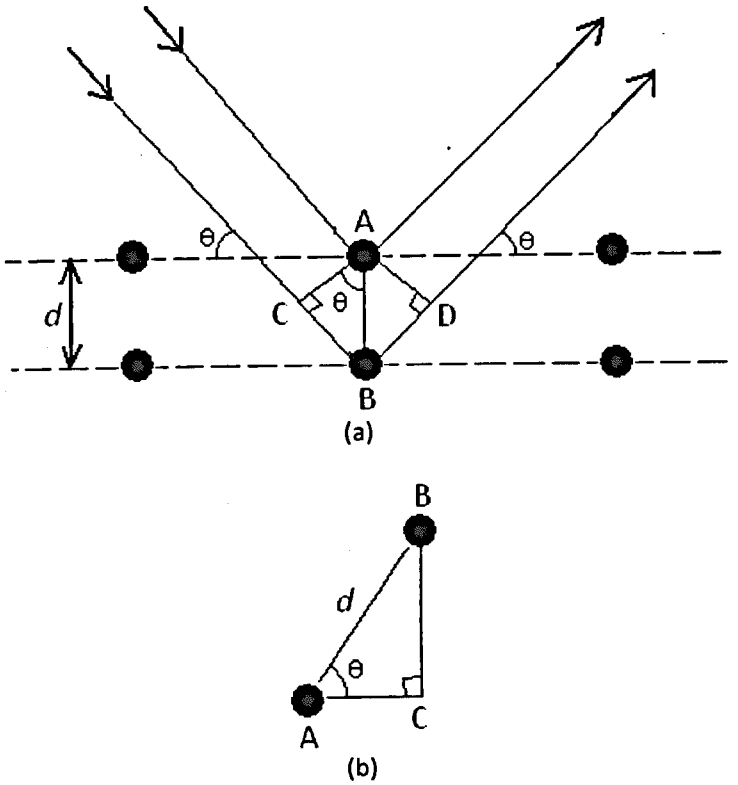

Figure 3.9: The Braggs Law. (a) Illustration of Bragg's Law showing X-ray scattered from a set of parallel planes inside the crystal (b) inset of the illustration in (a) showing spacing of the plane *d*, the angle θ between the incident ray and the scattering planes.

$$n\lambda = 2d\sin\theta \tag{3.1}$$

Braggs Law in equation 3.1 can be generalised as,

$$d(h,k,l) = \lambda/2\sin\theta(h,k,l) \tag{3.2}$$

where $d(h,k,l)$ is the distance between each corresponding (h,k,l) atomic plane and $\theta(h,k,l)$ is the incident angle where constructive interference occurs. The lattice plane of a crystal are defined by Miller indices. The reflection planes of the n^{th} order can be represented by (nh,nk,nl) plane reflection with h, k, and l are integers. The spacing of planes with Miller indices $d(nh,nk,nl)$ can be reduced to $d(h,k,l)/n$.

Diffraction measurements discussed here were acquired in the 'θ-2θ' arrangement in which atomic planes parallel to the substrate are picked out. The setup is called 'θ-2θ' because the samples can be rotated by the angle θ and the detector rotates simultaneously by the angle 2θ to pick up diffraction interference waves. The peaks in the X-ray diffraction pattern contain d spacing which can be used to calculate crystalline phases hence the orientation of thin films can be identified. Our Ni films have been characterized using PANanalytical(Philips) Xpert Materials research diffractometer (MRD). The X-ray source in the standard Philips is a high intensity ceramic sealed tube with a Cu-Kα source with wavelength of λ = 1.54 Å. Figure 3.10 is showing a basic setup of a goniometer in XRD setup.

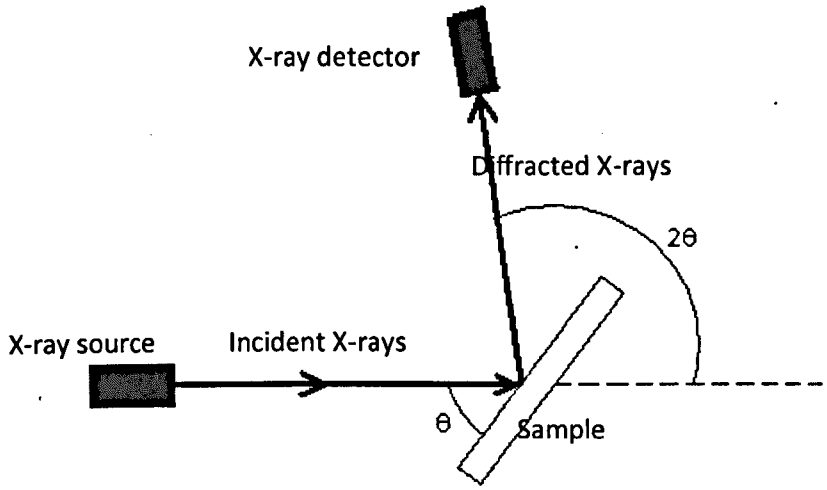

Figure 3.10: Schematic diagram of XRD 'θ-2θ' goniometer setup.

3.4 Transfer of graphene

After growth, graphene is transferred to dielectric substrates using a transfer method which was developed as part of this thesis work (Pollard et al., 2009, Kim et al., 2009). In the process, polymethylmethacrylate (PMMA) is spin-coated on top of the graphene terminated Ni surface. Since PMMA is very thin and difficult to handle

after the Ni has been etched, a polydimethylsiloxane (PDMS) layer is added to ease mechanical transfer. The graphene terminated Ni (with PMMA and PDMS on the top) is etched in $FeCl_3$ leaving graphene attached to PMMA which then is placed on a SiO_2/Si substrate. PMMA is then dissolved in acetone leaving graphene on the SiO_2/Si. This transfer process will be detailed in Chapter 4. In this section the methods used in the transfer will be described.

3.4.1 Spin coating

Spin coating is a common technique used in many micro-fabrication processes. In the case of the graphene transfer process, it is used to place a thin layer of PMMA on graphene surface. The spin coating process can be divided into three stages as shown in Figure 3.11. Initially, a quantity of solution is placed on the stationary substrate (see Figure 3.11(a)). When the substrate is accelerated up to the desired angular velocity, a large quantity of the solution is thrown off the substrate (see Figure 3.11(b)). When the substrate spinning has reached a constant angular velocity, the thinning of the surface layer is controlled by the viscous outward flow towards the substrate edge. This results in an even layer of the solution due to the viscous shear drag forces between the solution layer and the air which has reached an equivalent acceleration due to the spinning (Meyerhofer, 1978). The even thinning is generated by a steady flow of liquid which moves radially outwards followed by its ejection off the substrate edge. As the spinning progresses, the outward flow of the solution does not influence the thinning anymore. On the contrary, the thinning becomes dominated by the evaporation of the solvent from the solution layer.

To spin coat the PMMA, the substrate (our sample is graphene/Ni/SiO_2/Si) is placed on a vacuum chuck to ensure that it is stationary and stable. A drop of PMMA solution is then placed on top of the substrate. The PMMA spin coating process for

our case is performed at the speed of 3000 rpm for 40 s forming ~100 nm thick of PMMA. The spin-coater used in this work is the Solitec 5110.

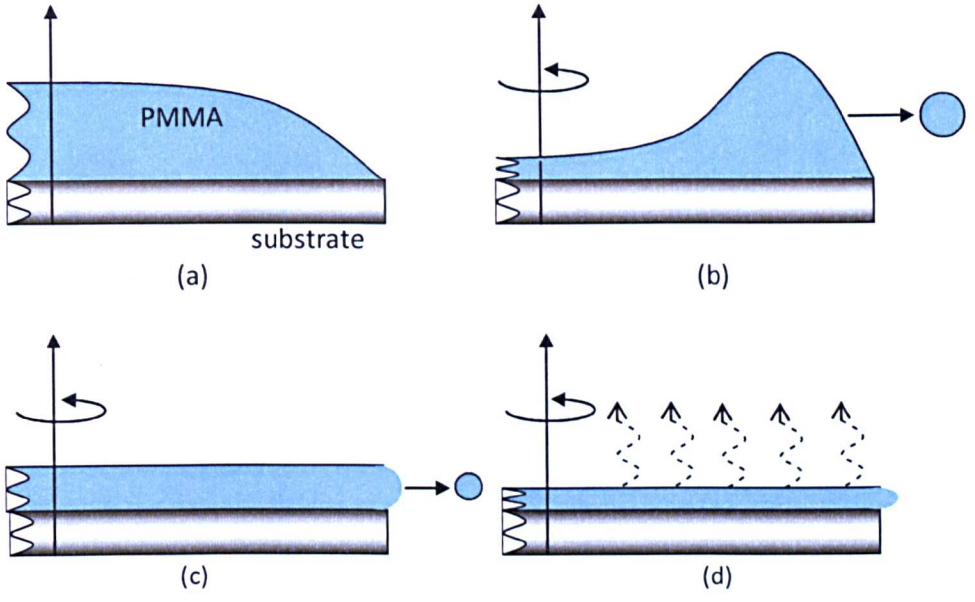

Figure 3.11: Stages in the spin coating process (a) PMMA is placed on the stationary substrate. (b) First stage: spinning reaches angular velocity, majority of the solution is thrown off. (c) Second stage: spinning at stable velocity, the coating is dominated by viscous flow. (d) Third stage: spinning at stable velocity, the coating is dominated by the solvent evaporation (this figure is adapted from Blunt, 2007).

3.4.2 Poly dimethylsiloxane (PDMS)

PDMS is commonly used as an elastomeric stamp for soft lithography because of its unique surface behavior. The organic portion of PDMS is the methyl group, which has very weak intermolecular forces. The inorganic siloxane makes PDMS a very flexible polymer and has very low surface energy. This makes PDMS a suitable candidate to be placed on our sample for easy handling. Before placing PDMS onto PMMA and graphene terminated Ni, the PDMS need to be prepared. PDMS consists of two component mixture which are the pre-polymer and the curing agent. The pre-polymer used is the Sylgard silicone elastomer 184 and the curing

agent is Sylgard silicone elastomer 184 curing agent. Both components are cured by mixing the pre-polymer and the curing agent at 10 : 1 by weight or volume. The mixing is usually done in a disposable plastic container because the mixture hardens after a few hours at room temperature and is difficult to clean so that the residual can be easily thrown away.

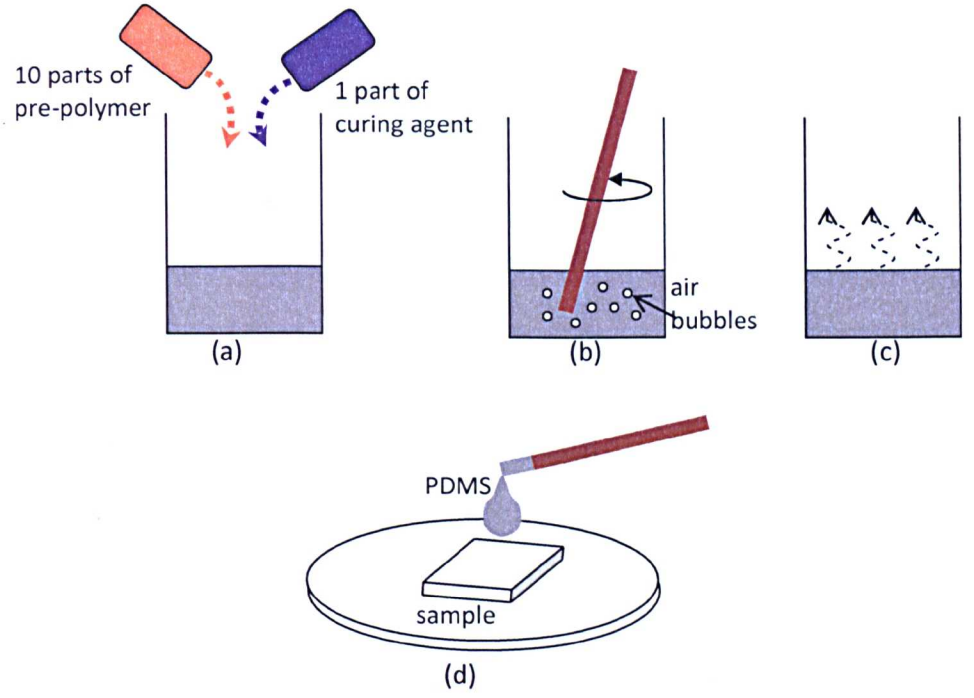

Figure 3.12: PDMS preparation method (a) 10 parts of pre-polymer and 1 part of curing agent are mixed. (b) The solution is stirred vigorously, creating air bubbles in the mixture. (c) Leaving the mixture for 20 - 30 min at room temperature cause the air bubbles to rise up making the mixture free of air bubbles. (d) the PDMS is placed on top of the sample before curing it at 150°C 10 min in the furnace.

While mixing the pre-polymer and curing agent, air is unintentionally introduced creating bubbles in the mixture. The mixture is allowed to settle for 20 - 30 min at room temperature depending on the volume of the mixture to reduce the amount of the air bubbles. Once the bubbles are removed, a drop of this PDMS is placed on top of the PMMA/graphene terminated Ni. Since the mixture is quite viscous, it forms a layer about 3 mm thick. To cure the PDMS, the sample is placed in

a furnace at 150°C for 10 min. The whole process described above is illustrated in Figure 3.12.

3.4.3 $FeCl_3$(aq) etching

$FeCl_3$ or ferric chloride aqueous solution is corrosive and used as an etchant for our Ni thin film. Mixing the $FeCl_3$ with water produces the aqueous solution. The aqueous $FeCl_3$ is the salt of combination of weak base $Fe(OH)_3$ with strong acid HCl. $FeCl_3$ dissociates as in equation 3.3,

$$FeCl_3 \text{ ------> } Fe(3+) + 3Cl(-1) \qquad (3.3)$$

When mixed with water, $FeCl_3$ combines with OH(-) present in H_2O, in which water also dissociates to a very small extent as in equation 3.4. Hence $Fe(OH)_3$ is obtained as in equation 3.5, which shows that in the aqueous solution, excess of H(+) ion is present. The solution becomes acidic with the presence of the HCl and the excess of H(+) ion.

$$H_2O \text{ <-----> } H(+) + OH(-) \qquad (3.4)$$

$$Fe(3+) + 3OH(-) \text{ ------> } Fe(OH)_3 \qquad (3.5)$$

The $FeCl_3$ consists of atoms Fe and Cl, which has atomic mass of 55.8 g and 35.5 g respectively. Since there are three atoms Cl present in the $FeCl_3$ formula, the molecular weight for Cl becomes 106 g. Adding both molecular weights of Fe and Cl gives the molar mass of $FeCl_3$, which is 162 g/mol. To prepare a 10ml of $FeCl_3$ aqueous solution with 1 M needs 0.01 mol $FeCl_3$. Hence by multiplying 0.01 mol with the molar mass or $FeCl_3$ gives the weight of 1.62 g $FeCl_3$ to make the 10 ml solution.

The preparation of the aqueous solution is illustrated in Figure 3.13. The $FeCl_3$ powder is firstly weighed before adding water and stirring forming an aqueous

solution with orange color. We usually filter the solution before keeping it in a glass container with lid. The filtration is important to avoid any $FeCl_3$ solid to attach to our graphene layer during the Ni film etching. Water is used to clean our sample after the etching process.

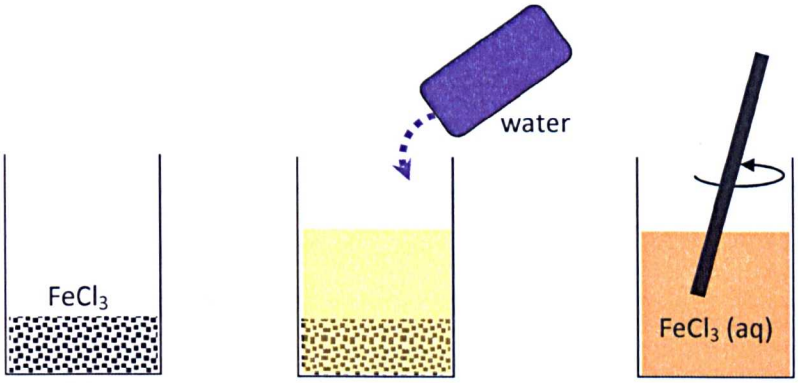

Figure 3.13: Preparation method of the $FeCl_3$ aqueous solution. (a) $FeCl_3$ is weighed. (b) High purity water is added to the $FeCl_3$. (c) The mixture is stirred until the $FeCl_3$ dissolves completely.

3.5 Characterization of graphene on SiO_2

After graphene is transferred to SiO_2 substrate, it can be easily observed using the optical microscope. Optical microscopy is very useful in identifying the number of graphene layers based on different contrast observed under visible light (Blake et al., 2007). However, it was not accurate compared to Raman spectroscopy which now has become the best tool to characterize graphene (Ferrari et al., 2006). Now the optical microscope is only used to obtain images of graphene and to identify the location of graphene layer before it is distinguished using Raman spectroscopy. This section will describe the optical microscopy and Raman spectroscopy used in the characterization of graphene on SiO_2.

3.5.1 Optical microscopy

Optical microscopy is used to observe our graphene layer on Ni films and SiO_2 substrates. The object is illuminated with white light through the objective lens, which is used to provide illumination and imaging. In this process, the light is reflected and transmitted by the glass reflector, which is placed in the optical path between the objective lens and the ocular (or the eyepiece that one looks into) at 45° angle. The reflected light is transmitted through the glass reflector towards the ocular. The basic arrangement of the optical microscope described above is illustrated in Figure 3.14. When the light interacts with the object, some of it is adsorbed, scattered and reflected, depending on the interaction. A fraction of the light that has interacted with the object then passes through the imaging lens system, which is used to give clear visual images of the object.

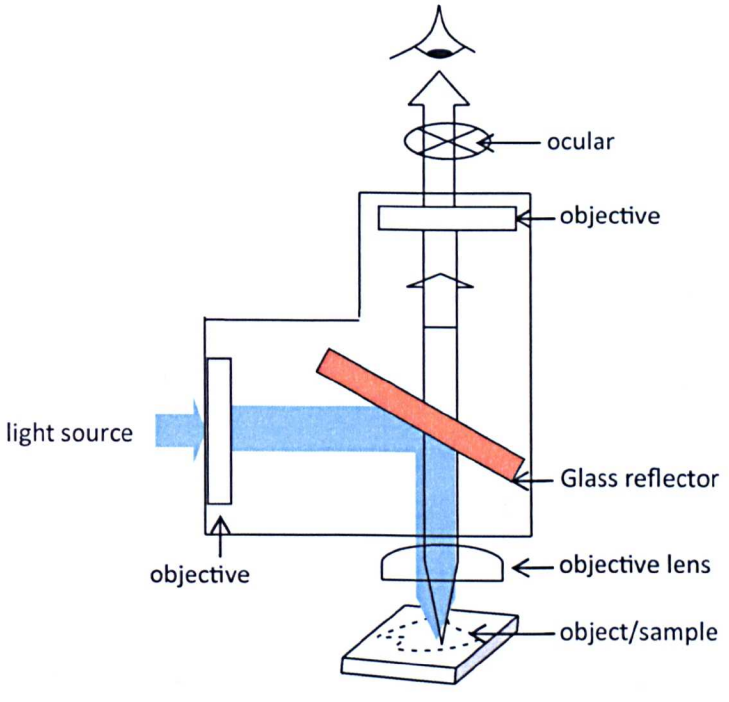

Figure 3.14: Basic diagram of the optical microscope.

The optical microscope used in this work is the Olympus BX51 Microscope. This system also has digital camera Olympus DP70 that has very good sensitivity, resolution, color reproduction and speed. The software used with this system is the Image Pro plus which is suitable for 2D and 3D image processing.

3.5.2 Raman spectroscopy

Raman spectroscopy is used to study graphene as it gives detailed information of graphene quality and layers. There are four important components in Raman system need to be considered; the excitation source or the laser, the sample illumination system and light collection optics, the wavelength selector using filter or spectrophotometer and the detector using Charge-Coupled Device (CCD). The basic set-up for Raman spectroscopy is shown in Figure 3.11.

The excitation laser for graphene detection usually chosen is green with a wavelength of 514 nm. However, the green laser of the Raman system that we have and used is with wavelength of 532 nm. The spatial resolution of the laser system can be approximated by the minimum laser focal spot on the sample which can be calculated by equation (3.6) below.

$$d = \frac{1.22\lambda}{NA} \tag{3.6}$$

d is the diameter of the laser spot, λ is the wavelength of the excitation laser (532 nm) and NA is the effective numerical aperture of the objective lens (NA = 0.75). So based on the equation above, the laser focal spot that we used is 0.87 μm.

A confocal light illumination and collection system was used in this work. The optical scheme for the confocal Raman spectroscopy is shown in Figure 3.15. The laser beam travels through the pinhole aperture (or the confocal hole) and irradiates the dichromatic mirror which is used to reflect the light at 90°. The laser light then

passes through the microscope objective lens which focuses the laser beam onto a point on the sample.

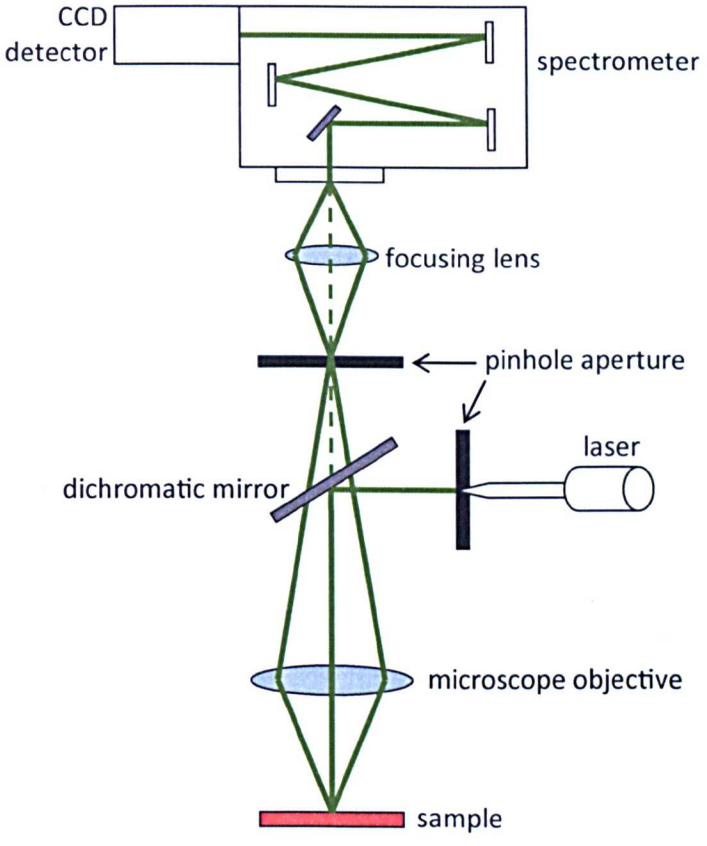

Figure 3.15: Optical scheme for confocal Raman spectroscopy including confocal microscopy, spectrometer and CCD detector.

The scattered light from the sample is directed through a notch filter which designed to filter a small range of light. The notch filter is used to block the Raleigh scattering. The scattered light then travels through a lens system to focus the light onto an entrance slit. The slit is the point where the scattered light enters the spectrometer. The entrance slit can be adjusted from 10 μm to 2.5 mm. We typically set the opening at 300 μm, which provided a good signal-to-noise ratio. The Raman bands are dispersed by the grating as a function of wavelength and are then incident on the CCD. There are different gratings that are available with the system, which

are 600 l/mm and 1200 l/mm which provide different spectral resolution. A CCD then detect the light and converts it into electric signal, amplifies it and sends it to the computer for processing.

The Raman spectroscopy system used in this study is Horiba Jobin Yvon LabRAM HR with integrated Raman microscope. The LabRAM HR provides high spectral resolution in the order of 0.3 cm^{-1} to 1 cm^{-1}. The software used with the system is LabSpec which has Raman spectrum and map acquisition, data analysis and processing.

3.6 Summary

This chapter has discussed four major aspects; graphene growth, characterization of graphene terminated Ni, transfer of graphene, and characterization of graphene on SiO_2. The first part of the graphene growth technique describes Ni film deposition in the Edwards Auto 306 vacuum coater and in ultra high vacuum (UHV) chamber including the graphene growth chamber. The characterization of graphene-terminated Ni is achieved using the atomic force microscopy (AFM), scanning tunneling microscopy (STM) and X-ray diffraction (XRD). The graphene transfer process employs spin coating, polydimethyl siloxane (PDMS) preparation and $FeCl_3$ etching. Finally this chapter describes the characterization of graphene on SiO_2 using the optical microscopy and Raman spectroscopy.

Chapter 4

Graphene Growth on Ni Thin Films

4.1 Introduction

The formation and isolation of high quality single layer graphene over large areas remained a significant challenge until relatively recently as explained in chapters 2 and 3. In this chapter the focus is on graphene growth on Ni thin films. The direct growth of graphene on Ni thin films has been extensively studied since it was the first approach which was used successfully to produce monolayer and few-layer graphene with good physical properties over large areas (Pollard et al., 2009, Reina et al., 2009). A common aspect of many experiments on graphene growth is that the resulting films may be successfully released and transferred onto dielectric substrates to provide large areas of single and bi-layer graphene. For example in our early work, we found 75% coverage of single layer graphene (Pollard et al., 2009) which, at that time was the highest monolayer fraction reported. Reina et al., 2009, demonstrated 87% coverage of graphene depending on the properties during growth on Ni films, but a significant proportion was bilayer.

In this chapter graphene growth on Ni thin films produced using two different evaporator systems (see Chapter 2) will be discussed. Ni thin films then undergo a series of annealing steps to optimise thermal cycling in an ultra-high vacuum (UHV) system. We found that graphene could be formed in UHV without the

intentional introduction of carbon feedstock giving films which were highly reproducible. In addition, we will demonstrate the influence of outgassing on the formation of graphene, which was performed before Ni deposition. We will also demonstrate the introduction of carbon by immersion of Ni thin films in acetone.

Overall, the objective of this work is to study graphene formation on Ni thin films, to investigate properties that lead to graphene formation, to introduce a method to release and transfer graphene onto dielectric substrate and to explore graphene formation with and without intentional introduction of carbon. This study shows the importance of considering unintentional carbon sources which must be ascertained when developing models for graphene growth.

4.2 Graphene release and transfer

We have developed a process to release graphene from the Ni thin films and transfer it to SiO_2/Si substrates. Firstly, the samples which consist of graphene/Ni/SiO_2/Si are spin-coated with polymethylmethacrylate (PMMA). The PMMA spin-coating process is performed at 3000 rpm for 40 s, which produced ~250 nm thick layer on top of graphene. PMMA was then baked by placing the sample on a hotplate at 180°C for 2 min.

The next step is to deposit a layer of polydimethylsiloxane (PDMS) which was prepared by mixing elastomer base and elastomer curing agent at the ratio of 10:1. Droplets of PDMS were dropped on top of PMMA and cured at 150°C for 10 min in a furnace. The PDMS coating is quite thick (~0.3 cm) and typically covers the Ni films edges and leaked onto a supporting glass cover slip. The PDMS around the sample edges was cut in order to allow $FeCl_3$ to contact with the Ni films. The PDMS layer was used to provide additional mechanical support to the thin PMMA films.

To release graphene from Ni/SiO_2/Si, the sample is then immersed in aqueous $FeCl_3$ for about 18 hours to completely etch Ni film leaving graphene attached to the PMMA/PDMS. The $FeCl_3$ residue on graphene/PMMA/PDMS was cleaned in de-ionized (DI) water before placing the graphene surface onto SiO_2/Si

substrate (90 nm). The sample then immersed in acetone for about 3 hours to dissolve the PMMA leaving only graphene attached to SiO_2 substrate. We found that immersion of the sample in acetone for more than 3 hours provided a large coverage of transferred graphene in which breakage of the film can be minimized. Finally the graphene on SiO_2/Si was cleaned in isopropanol (IPA) and blown with nitorgen gas to dry. The whole process detailed above is shown in a diagram in Figure 4.1. The resulting layer of graphene on 90 nm SiO_2 substrate is optically visible based on the different contrast from the SiO_2 surface. The sample is then characterized using Raman spectroscopy.

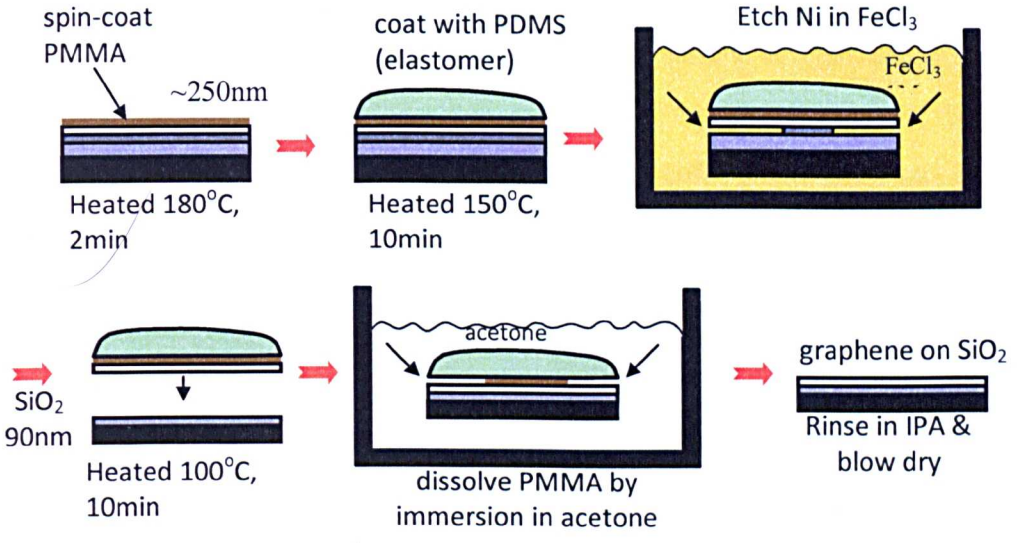

Figure 4.1: The process to release graphene from Ni film and transfer it to SiO_2 substrate (90 nm).

4.3 Overview of vacuum systems for Ni deposition

This section is focused on Ni thin film synthesis and preparation. Initially, before we had a dedicated system for Ni deposition, the Ni thin films were prepared in a commercial evaporator. We then built a UHV evaporator system connected to the graphene growth system. The systems will be described below in terms of the resulting Ni thin film morphology based on the AFM characteristics.

4.3.1 Ni thin film deposition in commercial evaporator

In our early work, Ni thin films on Si/SiO_2 substrates were produced in a standard evaporator, the Edwards Auto 306 Vacuum Coater. This system was used to prepare some preliminary samples because initially we did not have a specific UHV system for Ni deposition. In this section Ni thin films which were produced using the Edwards Auto will be described. These films are used to produce large areas of single layer graphene as described in 4.4. The substrates used in this experiment were Si (100) wafers with a SiO_2 layer of thickness 300 nm. A 100 nm thick Ni layer is deposited and the system has a vacuum base pressure of 10^{-6} to 10^{-7} mbar. The evaporation rate was ~0.02 nm/s.

An AFM image of a sample of Ni deposited on SiO_2/Si substrate using this evaporator is shown in Figure 4.2(a). Based on the profile of the Ni grains, the size varies between 21 nm to 33 nm. The roughness profile gives root mean square (RMS) of the roughness of 1.3 nm. The Ni films are then removed from the system and stored under atmospheric conditions for, typically, 1 to 3 days for AFM imaging before they are loaded into a separate UHV system. The samples are then annealed and Figure 4.2(b) shows that the material was re-distributed. The surface became highly faceted with facets average size of ~1 μm following vacuum annealing at 800°C in the UHV system. Further description of the annealing process in UHV will be discussed in 4.4.

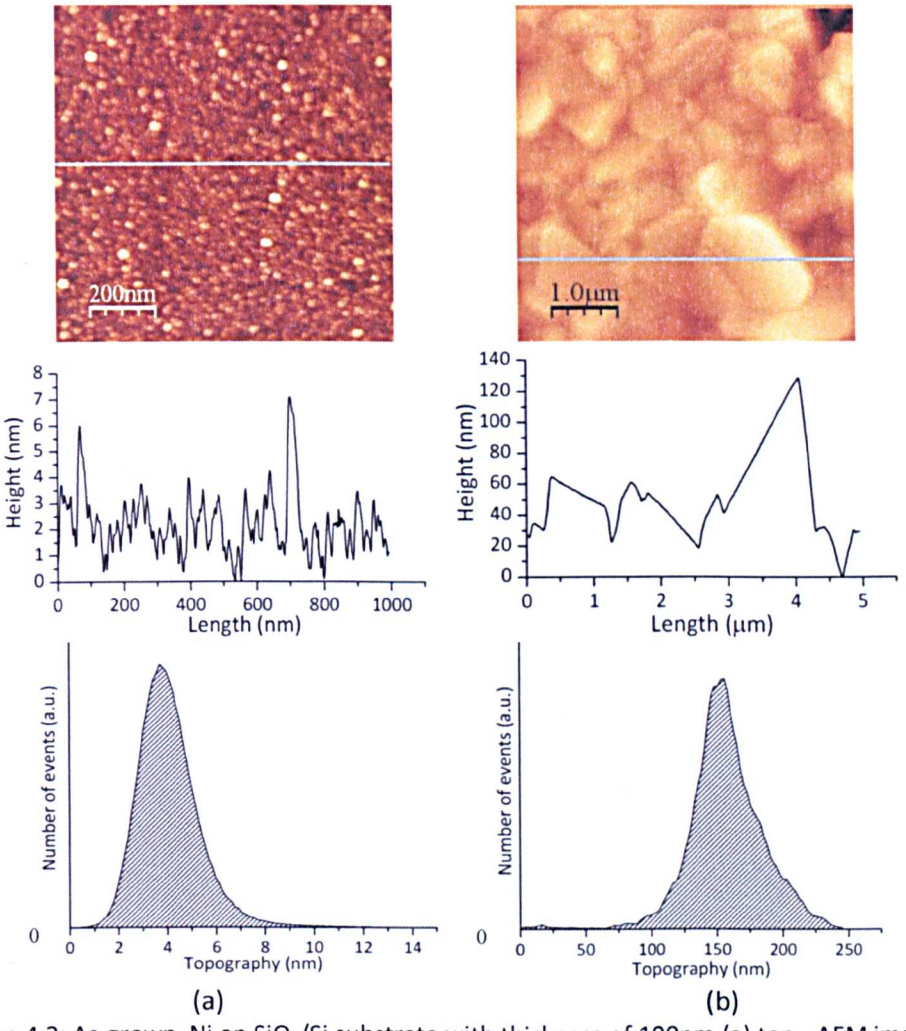

Figure 4.2: As-grown Ni on SiO_2/Si substrate with thickness of 100nm (a) top - AFM image of Ni thin film before annealing, middle – AFM height and length profile, bottom – AFM roughness profile (b) top – AFM image of graphene on Ni after annealing at 800°C, middle – AFM height and length profile, bottom – AFM roughness profile.

4.3.2 Ni thin film deposition using a UHV evaporator system

In order to control Ni thin film deposition and avoid exposure of the samples to atmosphere after the deposition, we built a UHV evaporator system directly connected to the graphene growth chamber. The Ni thin films produced in this system have a slightly different morphology than those produced in commercial evaporator. It should be noted that the same deposition rate was used in the

commercial evaporator and applied in the UHV system (evaporation rate of about 0.02 nm/s) with a base pressure of about 1 x 10^{-10} mbar. However the design of the UHV system for Ni deposition is slightly different in terms of the distance between the alumina crucible (that contains Ni source) to the substrate surface which is larger than the system in the commercial evaporator. Design of both systems are described previously in Chapter 3.

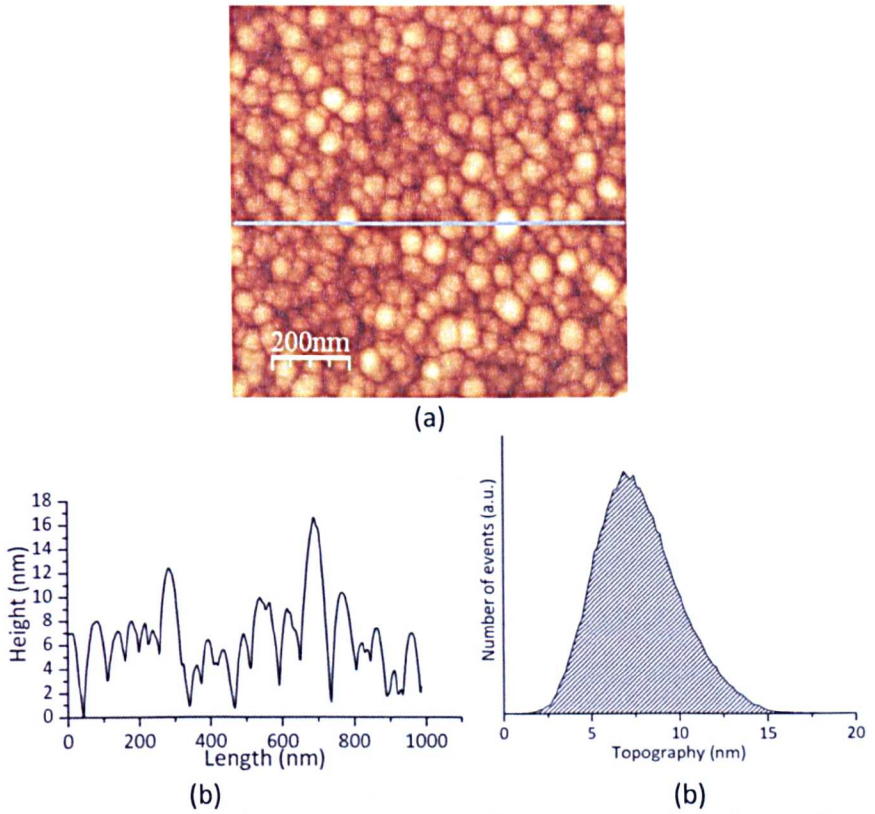

Figure 4.3: (a) AFM image of as-grown Ni on SiO_2/Si substrate with thickness of 60 nm (b) AFM height and length profile (c) AFM roughness profile.

Figure 4.3(a) shows an AFM image of a 60 nm Ni film with Ni grain size between 30 to 58 nm, which is larger than Ni grains deposited in Edwards Auto 306 (see 4.3.1). The RMS of roughness is 2.4 nm. We suggest that the evaporation of the Ni in this system results in higher substrate temperature than in Edwards Auto 306 due to radiant heating.

4.4 Graphene growth in UHV system

Both Ni films deposited in the commercial evaporator and in the UHV evaporator system were then annealed in the UHV system to grow graphene. The growth without and with intentional introduction of carbon sources will be explained under this section. In the transfer process, a 90 nm thick SiO_2 substrate was chosen to maximize the contrast in optical microscopy and allows the discrimination between single and few-layer graphene. The Raman spectra in this work were taken with a 50x objective at 514 nm laser excitation and 4 mW of laser power using a Renishaw micro-Raman spectrometer for spectra taken in Manchester. For the spectra taken in Nottingham, the Raman system has been described in Chapter 3.

4.4.1 Graphene growth without the intentional introduction of carbon

In our initial work, graphene was formed by annealing Ni films in vacuum (base pressure of ~5 x 10^{-10} mbar) without any intentional carbon source. This means that the samples are not exposed to any carbon containing gasses or immersed in an organic solvent. Initially, the samples are outgassed by annealing at 500°C for about 12 to 18 hours and are then followed by annealing at 500°C to 800°C for 20 min. The samples are allowed to cool to room temperature by reducing the current through a silicon strip heater to zero over a period of approximately 60 s. A significant transformation of the Ni grains is observed for annealing temperature between 700°C to 800°C.

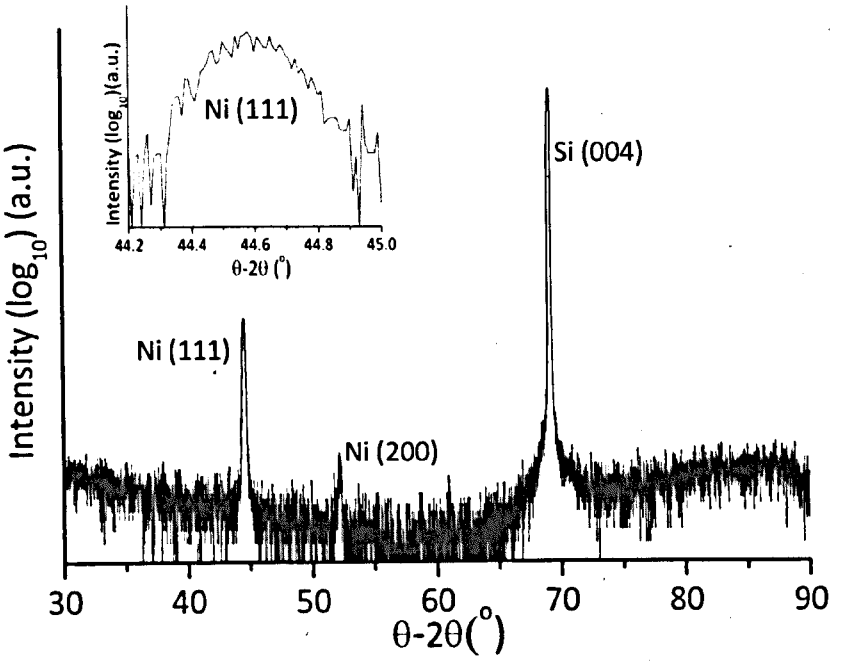

Figure 4.4: The θ-2θ XRD result for Ni thin film appears at 44.5° which corresponds to the lattice spacing *d* of 2.03 Å and the peak is identified due to (111) oriented crystallites.

The Ni film crystallinity has been investigated using X-ray diffraction (XRD). Figure 4.4 shows θ-2θ° XRD results using Cu : $K\alpha_1$ radiation with wavelength of 1.54 Å at 5 sec/degree angle step. The first order Bragg reflection of the Ni thin film appears at 44.5° which corresponds to the lattice spacing *d* of 2.03 Å. This provide the evidence of Ni in a (111) crystal orientation. The full width of half maximum (FWHM) of the peak is very small (~0.2°) which implies that the crystalline quality of the Ni is very good. The peak at 52.7° is corresponds to Ni (200), and the peak at 69° is corresponds to Si (004).

Figure 4.5 shows an optical micrograph of a graphene layer on 90 nm SiO_2 substrate after the transfer process (Pollard et al., 2009). The lighter contrast is single layer graphene while the darker contrast corresponds to few-layer graphene (see Raman spectra below). The image has been examined using an image histogram based on the Raman spectra obtained from different area of color contrast. It is found that 75% of the film is single layer graphene and the other 25% is covered by

few-layer graphene, which likely to be between two to four layers. And remarkably only 1% of the film has a greater thickness.

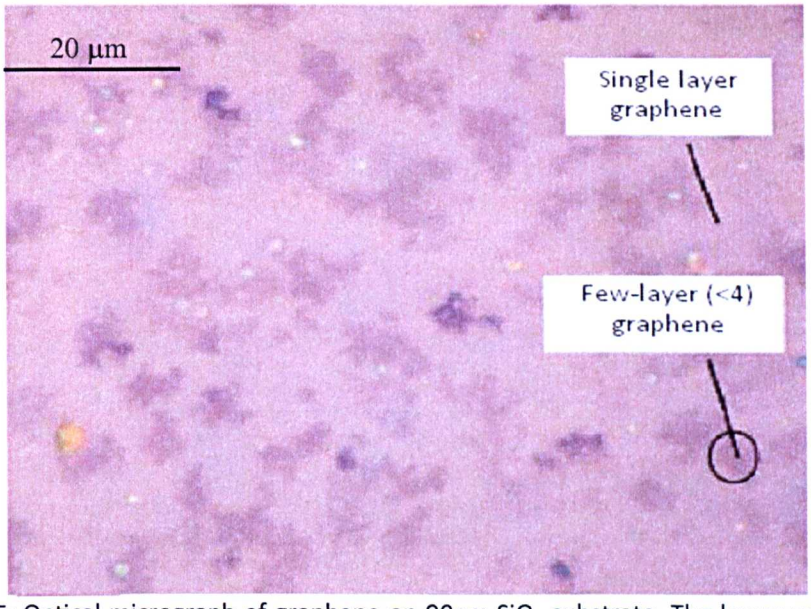

Figure 4.5: Optical micrograph of graphene on 90nm SiO_2 substrate. The lower contrast is corresponding to monolayer and the higher contrast is corresponding to few-layer graphene. Image acquired at Manchester University with Rahul Nair.

Raman spectra have been acquired on areas of different color contrast observed under the optical microscope (Figure 4.5). The Raman spectra of single and few-layer graphene are shown in Figure 4.6. The disorder-induced band or D band at 1350 cm^{-1} is observed on both single- and few-layer graphene. An image acquired using a scanning electron microscopy (SEM) is carried out to examine the film and the presence of cracks are confirmed as shown in Figure 4.7 (Pollard et al., 2009). However the type of defects that contribute to the D band intensity is still unclear and is high for both spectra with I_D/I_G of 0.6 and 0.5 (but smaller than that observed for graphene oxide, reduced graphene oxide (Gomez-Navaro et al., 2007), and graphane (Elias et al., 2009)) which indicates that the film has a reasonably good quality. An experiment aimed at reducing this D band intensity has been performed and will be discussed in Chapter 5.

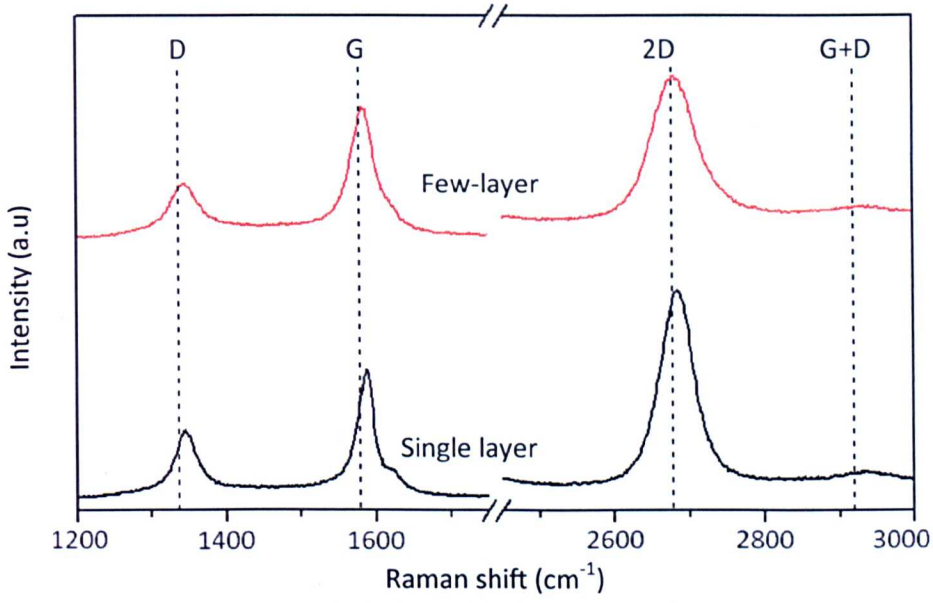

Figure 4.6: Raman spectra of single layer (black - corresponds to lower contrast region in Figure 4.5) and few-layer (red - corresponds to higher contrast region in Figure 4.6). This spectra was acquired at Manchester University with Rahul Nair.

As mentioned earlier in Chapter 2, the intensity of the G band and the Raman shift give the information about the number of graphene layers. The G band in Figure 4.6 observed at ~1590 cm^{-1} has intensity ratio (I_{2D}/I_G) which agree well with single layer (black) as the I_{2D}/I_G of 1.7. The I_{2D}/I_G for the area with higher contrast (red) is 0.7, which suggests that the area has more than double-layer. The downshift of the G band towards lower wavenumber of ~3 cm^{-1} (Graf et al., 2006) suggests that the lower contrast is single layer while the G band with higher wavenumber is few-layers.

The 2D band at ~2690 cm^{-1} for the lower contrast region agrees well with single layer graphene based on the ratio I_{2D}/I_G (1.7) and the full width of half maximum (FWHM) is ~33 cm^{-1} (obtained from a fit with a single Lorentzian functions). The FWHM of the 2D band for few-layer graphene in Figure 4.6 is ~50 cm^{-1}, however it exhibits a single Lorentzian peak which is likely to correspond to the turbostratic graphite. As discussed in Chapter 2, turbostratic graphite has a single sharp 2D band with FWHM of ~50 cm^{-1} and is upshifted at ~20 cm^{-1} (Ferrari et al.,

2006). The hypothesis that the low contrast regions are single layers, is supported by the diffraction patterns from transmission electron microscopy (TEM) as in Figure 4.7(b) and (c). These results show that single layer regions have equally intense first- and second-order spots, while few layer regions give rise to multiple diffraction spots caused by rotationally disordered (turbostratic) graphite (Pollard et al., 2009). Figure 4.7(d) is the diffraction spots intensities for single layer regions which is consistent with that reported by Meyer et al., 2007.

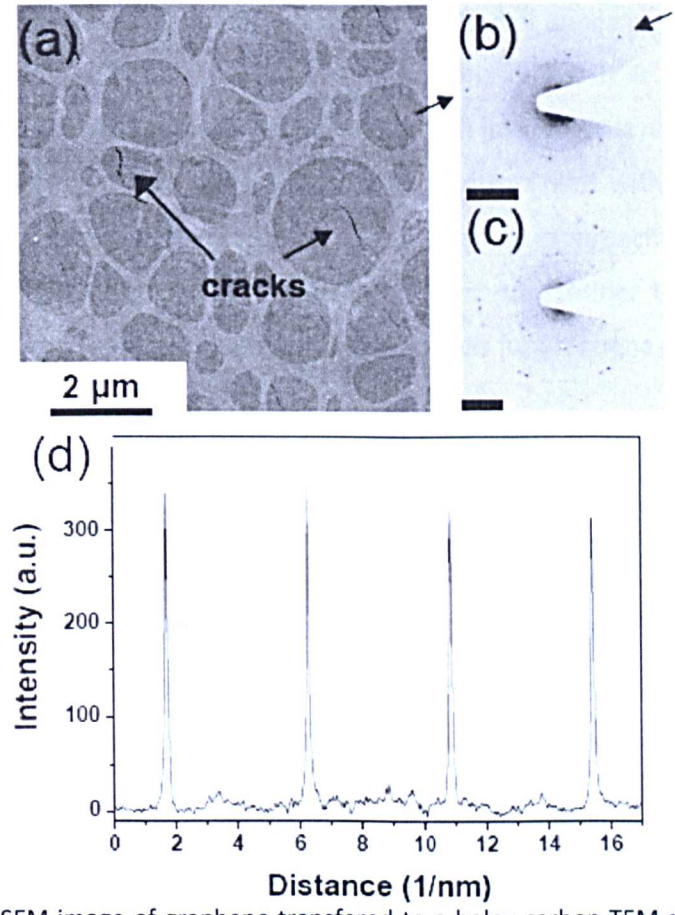

Figure 4.7: (a) SEM image of graphene transfered to a holey carbon TEM sample grid with dark grey regions are identified as graphene and black lines are identified as cracks . (b) and (c) TEM diffraction patterns (Technai F30, accelerating voltage 300kV) from single-layer ((b) scale bar 4.3 nm^{-1}) and few-layer ((c) scale bar 3.8 cm^{-1}) regions. (d) intensity of diffraction spots versus position (in reciprocal space) along the line between the points marked by arrows in (b). The results are taken from Pollard et al., 2009.

The source of carbon that contributes to the formation of graphene was unclear. However, it has to be noted that the Ni films in this work are deposited using the Edwards Auto 306 Vacuum Coater that uses a turbo molecular pump (oil-based primary pump) backed by a rotary pump (secondary pump). To investigate the possible source of carbon, several graphene growth cycles were carried out using Ni films in an evaporator with oil-free pumps (turbomolecular, ion and scroll pumps) as described in the next section.

Generally, this work has shown that it is possible to obtain single layer graphene over large area using the very simple method of annealing Ni thin films in vacuum without intentional introduction of carbon source. It is likely that this process involves converting trace amounts of carbon into single layer graphene and is highly reproducible. Remarkably, this process produces films with, at the time of publication, higher single layer fraction than alternative approaches to graphene growth on Ni. We suggest that it is also important to consider the presence of unintentional carbon sources when developing models for graphene growth.

4.4.2 Influence of outgassing

We tried depositing Ni films in the UHV evaporator system using ion pump which is oil-free with the same deposition parameters used for Edwards Auto 306 evaporator; evaporation rate of 0.02 nm/s, Ni thickness of ~60 nm. The base pressure is between 10^{-9} to 10^{-10} mbar. Before Ni deposition, the samples are outgassed by annealing at 500°C for about 12 to 18 hours and then annealed at 500°C to 800°C for 20 min. The same processing parameters as in 4.4.1 are also used for this type of Ni films which involves annealing the Ni films between 500°C to 800°C in vacuum of base pressure 1 x 10^{-10} mbar. However graphene is not formed on any of the samples.

We then tried to follow the same approach as described above except that the outgassing step was omitted. The Ni surface after the treatment has Ni grains as

in Figure 4.8 with a size varying between 20 nm and 100 nm. Remarkably, graphene is successfully formed on the Ni film. This suggests that without the outgassing step, carbon-containing adsorbates remain on SiO_2 and can be incorporated into Ni films during growth and subsequently converted to graphene during annealing. However, samples produced using this approach are highly defective, as proven by the optical micrograph and Raman spectrum.

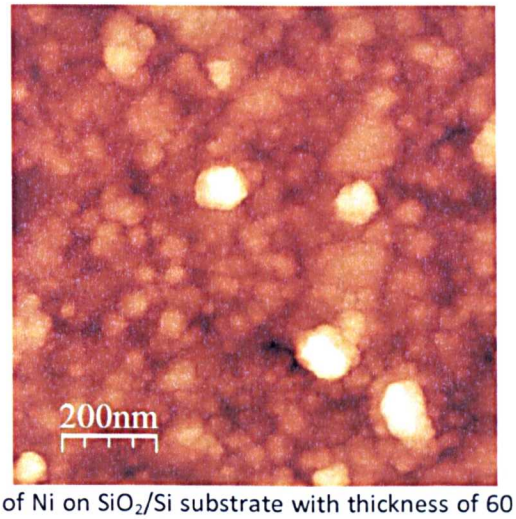

Figure 4.8: AFM image of Ni on SiO_2/Si substrate with thickness of 60 nm, deposited in UHV evaporator system, annealed at 700°C in base pressure of 1 x 10^{-10} mbar, 15 min, no outgassing process. The AFM image of the as-grown Ni film is shown in Figure 4.2.

Figure 4.9(a) shows the optical micrograph of the graphene film on SiO_2 (90 nm) after it is transfered from the Ni film. The sample is not outgassed before the Ni deposition process. After the Ni film is deposited, the sample is annealed in vacuum at 700°C for 15 min before it is transfered to SiO_2 substrate. The optical micrograph clearly displays a continuous but broken film with dark spots which likely to be thicker regions. Raman spectra are taken on the large region with lighter contrast and on the dark spots.

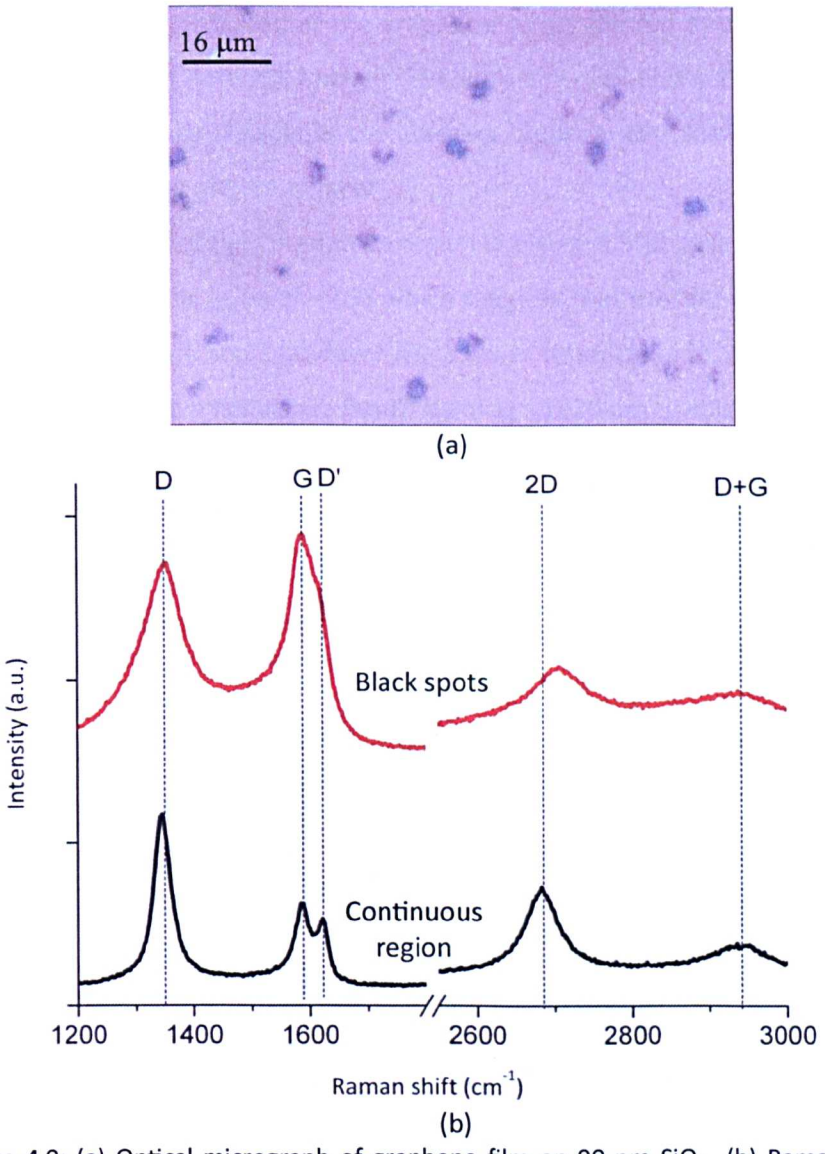

Figure 4.9: (a) Optical micrograph of graphene film on 90 nm SiO_2 (b) Raman spectra of graphene in (a) consists of 3 to 4 layer graphene (black) and graphite (more than 5 layers) (red) on SiO_2, grown on Ni film (in Figure 4.8) where it was deposited in UHV evaporator system, annealed at 700°C in base pressure of 1 x 10^{-10} mbar, 15 min, no outgassing process.

The spectra are shown in Figure 4.9(b) with the black spectrum acquired in the lighter contrast region and the red spectrum over the dark spots in Figure 4.9(a). Both regions have a very high intensity of the defect-induced, D, band with I_D/I_G of 0.9 on the dark spots and 2.3 on the continuous area. The high intensity of D band on the lower contrast region may arise from the highly fragmented film since the D

band is commonly observed at the graphene edges (Ferrari et al., 2006). However the specific type of defect is unclear. The high intensity of the D band on the dark spots may caused by defects in the stacking order or structural order of the film since this is a thicker graphene layer.

The G band of the continuous region in Figure 4.9(b) observed at ~1590 cm^{-1} has an intensity ratio, I_{2D}/I_G of ~0.95 which suggests that the film is double layer. The spectrum of the dark spots however has a lower intensity ratio, I_{2D}/I_G of ~0.7 which suggests that the film is thicker. The D' band at ~1620 cm^{-1}, which forms a shoulder at the right side of the G band, is also a defect and disorder induced band, however its signal is weaker compared to the D band. Comparison between the D' bands of both regions (in Figure 4.9(a)) suggests a different origin of defects in this case, the broken film on the continuous region.

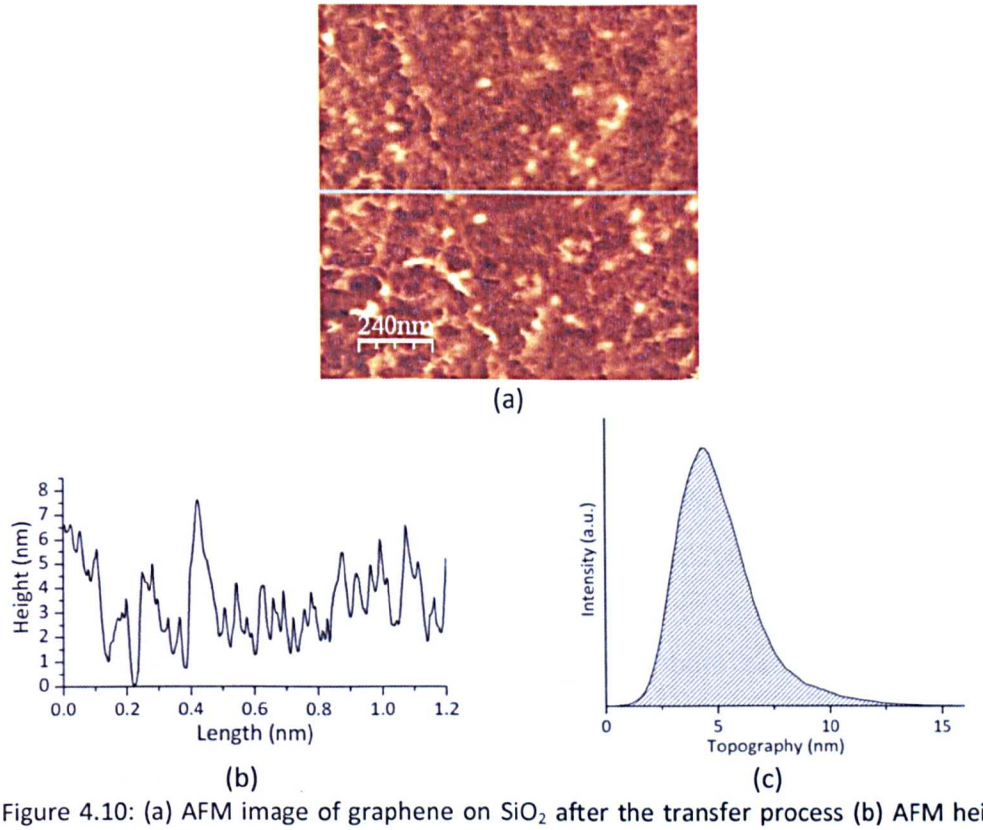

Figure 4.10: (a) AFM image of graphene on SiO_2 after the transfer process (b) AFM height profile of graphene (c) AFM roughness profile of graphene.

The 2D band line width is related to the number of graphene layers. The 2D band of the black spectrum has a frequency shift of 2680 cm^{-1} with FWHM of ~57 cm^{-1} which indicates that the film is few-layer. The red spectrum has the frequency shift of 2700 cm^{-1} with larger FWHM of ~76 cm^{-1}, suggesting a thicker film. The I_{2D}/I_G ratio mentioned before (~0.7) illustrates that the film of the dark spots is thick and may have more than five layers (Ferrari et al., 2006; Gupta et al., 2006). However, the 2D band for the black spots exhibits a single Lorentzian which suggests that this region consists of disordered or non-Bernal stacking, known as turbostratic (Reina et al., 2009). The AFM image of the released and transferred graphene from Ni film to SiO_2/Si substrate is shown in Figure 4.10 above. The image displays the RMS of the surface roughness is 1.8 nm.

4.4.3 Introduction of carbon source

The introduction of carbon using solvent immersion was investigated by immersing Ni thin films in acetone. Acetone is an organic compound that contains carbon with chemical formula of $(CH_3)_2CO$ previously used in graphene growth on Rh (Müller et al., 2009). To distinguish the effect of carbon from acetone and the presence of adsorbates on SiO_2, we produced samples using two different methods. The first method is performed using the outgassing process and in the second method the outgassing process before Ni deposition was omitted. After Ni deposition in vacuum, the Ni thin films were taken out, exposed to the atmospheric conditions and then immersed in acetone for 1 to 2 min. The samples were then loaded back into the vacuum system and annealed at 700°C for 15 min in base pressure of 1×10^{-10} mbar.

Figure 4.11 shows a comparison between both samples, which were outgassed and non-outgassed before Ni deposition. By comparing both defect induced bands or D bands, it shows that the non-outgassed sample has higher D band intensity compared to the outgassed sample with I_D/I_G of 1.75. The D' band

which is always weak, also lower for the outgassed sample. The intensity ratio of I_{2D}/I_G for the outgassed sample is ~1.65 which suggest single layer graphene. Whilst the non-ougassed sample has the I_{2D}/I_G ratio of ~1. Other than I_{2D}/I_G ratio, the width of 2D band can indicate the number of graphene layers. The 2D band of the non-outgassed sample has a broad 2D band with a shoulder on the left side that gives a FWHM of ~73 cm^{-1} suggesting that the film is few layer (Gupta et al., 2006). The outgassed sample has single sharp 2D band that exhibit single Lorentzian peak with FWHM of ~34 cm^{-1} which confirm that the film is single layer.

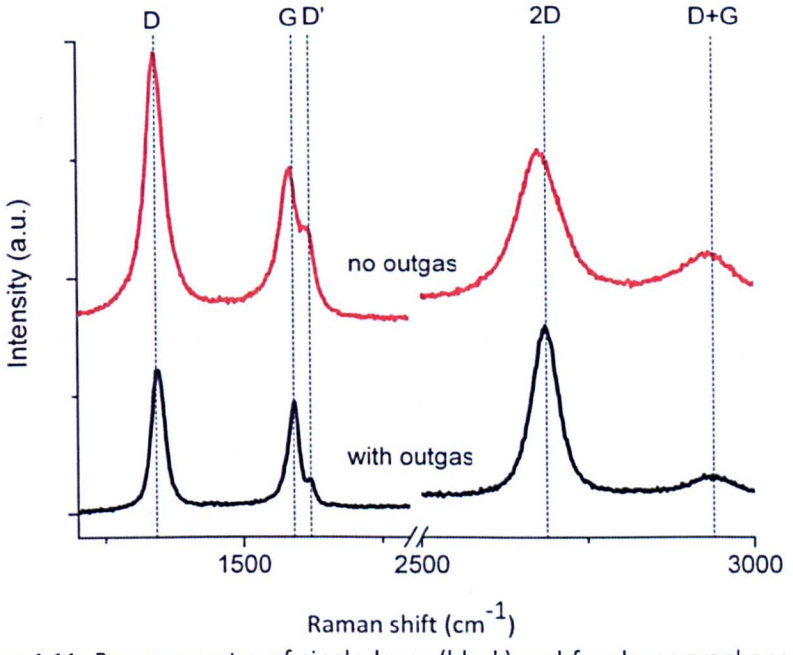

Figure 4.11: Raman spectra of single layer (black) and few-layer graphene (red) on 90 nm SiO_2. The sample with single layer graphene was outgassed while the few layer graphene was not outgassed before Ni deposition. Both samples were annealed at 700°C in base pressure of 1 x 10^{-10} mbar, 15 min.

We have demonstrated that the outgassing process is important to produce single layer graphene with better film quality, based on the observed Raman bands. Even though the D band is still quite high, we believe that some growth parameters can be tuned to reduce defects or disorder of the graphene film formed on Ni. The immersion of the Ni films in acetone is known to provide a direct introduction of

carbon to the sample, however exposure of the Ni film to atmosphere could unintentionally introduce carbon to the sample and this process cannot be ignored. Hence, we carried out further work to intentionally introduce carbon using propylene to form graphene on a Ni film without exposing the sample to atmospheric condition. The aim of the work is to reduce the D band or concisely to reduce graphene film defects and disorder. The work is further detailed in Chapter 5.

4.5 Summary

The first part of this chapter has described our method to release and transfer graphene from Ni film to SiO_2/SiO substrate. It follows with an overview of the vacuum systems which we used to deposit Ni thin films. The section describes two different systems; commercial evaporator (Edwards Auto 306 Vacuum Coater) and UHV evaporator system in terms of the resulted Ni thin films.

The main section in this thesis is on graphene growth in our UHV system. on the graphene formation without intentional introduction of carbon. Ni films deposited using the commercial evaporator (using oil-based vacuum pump) show a significant transformation in the Ni grain size between annealing treatment of 700°C to 800°C, identified as (111) oriented crystallites. We have proven that is possible to produce single layer graphene over large area (~75% coverage) using the very simple method of annealing Ni thin films in vacuum without intentional introduction of carbon source. We demonstrate the possibility of conversion of carbon-containing adsorbates on SiO_2 to single layer graphene and find that this is highly reproducible. Remarkably, this process produces films with higher single layer fraction than alternatives approaches to graphene growth on Ni. We suggest that it is important to also consider the presence of unintentional carbon sources when developing models for graphene growth.

We then discuss graphene formation on Ni thin films deposited in the UHV evaporator system (using oil-free vacuum pump). We demonstrate the effect of outgassing the SiO_2 substrates before Ni deposition process which has proven that the process is essential in the elimination of any adsorbates on SiO_2 which can lead to the formation of graphene on Ni films. We also demonstrate the effect of outgassing and graphene growth with the intentional introduction of carbon by immersing the Ni film in acetone before annealing it in vacuum, which resulted in single layer graphene. Based on this work, we propose the importance of outgassing the SiO_2 substrates to produce single layer graphene with better film quality. Based on the Raman D band intensity ratio ,I_D/I_G (~0.9), we suggest that some growth parameters can be modified to reduce the defects. It has to be noted that samples in this work are exposed to atmosphere which can also unintentionally introduce carbon to the sample and this process cannot be ignored. Hence, further work is performed to intentionally introduce carbon using propylene gas to form graphene on Ni film without exposure of the sample to atmospheric conditions. The aim of the work is to reduce the Raman D band intensity which is a measure to the amount of defects in graphene. The work is further detailed in Chapter 5.

Chapter 5

Monolayer Graphene Growth on Ni Thin Films using Chemical Vapour Deposition (CVD)

5.1 Introduction

The formation of graphene on Ni films has been explored using various methods to introduce carbon. These include immersion of the metal in an organic solvent (Pollard et. al., 2009) and exposing the metal to carbon containing gasses (Obraztsov, 2007; Yu et al., 2008; Reina et al., 2009; Kim et al., 2009). In addition, some studies focus on the use of solid carbon sources eg. polymers (Sun et al., 2010), as well as decomposition of carbon-containing molecules (Perdigao et al., 2011). This chapter however will be focusing on the formation of graphene by exposing Ni thin films to a carbon-containing gas, in particular, propylene. Our approach is based on previous work on the formation of graphene (Dedkov et al., 2008; Farias et al., 1999) on single-crystal Ni (111) under UHV conditions.

The work in this chapter may be viewed as a continuation of Chapter 4 but using the intentional introduction of carbon source. Since the amount of defects are relatively high in the work described in Chapter 4 and in the initial graphene samples formed using propylene, this work is carried out to identify the factors that affect the amount of defects quantified by the intensity of the Raman D band. The dependence on annealing temperature, exposure time to propylene and Ni film

thickness will all be discussed. The objective of this work is to obtain large coverage of low defective single layer graphene.

5.2 Propylene

Propylene or propene is an alkene with the chemical formula C_3H_6 which contains carbon-carbon single and double bonds. Propylene is gaseous at room temperature and atmospheric pressure. Figure 5.1 shows the molecular structure of propylene with a carbon - carbon single and double bond as well as bonding with hydrogen atoms.

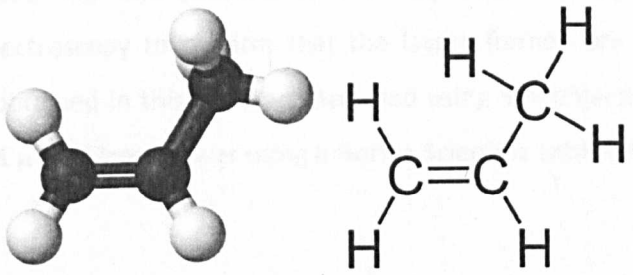

(a) (b)

Figure 5.1: The geometry of propylene with (a) propylene molecule with carbon atoms are represented by black spheres and hydrogen by white spheres (b) chemical structure of propylene showing carbon - carbon single and double bonds.

Propylene is introduced into our vacuum system where it can interact with a heated Ni thin film. Graphene is formed through decomposition of propylene gas on Ni (111) according to the methods described in previous works (Dedkov et al., 2008; Farias et al., 1999). This process involves breaking the carbon-carbon and carbon-hydrogen bonds.

5.3 Sample preparation

Several aspects of the sample preparation are similar to those described in Chapter 4. The Si/SiO_2 (with SiO_2 thickness of 300 nm) are outgassed at ~500°C for

14 to 18 hours. A Ni film (thickness 100 nm) is then deposited by sublimation. The Ni films are then heated in UHV (base pressure of ~1 x 10^{-9} to 10^{-10} mbar) to temperatures varying between 600°C and 850°C. It takes 5 to 15 min to reach this temperature. Once the required temperature is attained, the samples are exposed to propylene for 5 to 20 min. The pressure during propylene exposure rises to 1 x 10^{-6} mbar and is controlled by a leak valve. The process is then ended by closing the leak valve and followed by cooling the sample to room temperature by reducing the current through the silicon heater over a period of 15 sec.

The graphene films formed on the Ni thin film surface are transferred to 90 nm SiO_2 substrates using a similar approach to that explained in Chapter 3, 4 and Pollard et al., 2009. The films obtained on the SiO_2 substrates are then examined using Raman spectroscopy to confirm that the layers formed are graphene. The Raman spectra obtained in this work are acquired using 50x objective at 532 laser excitation and ~1 μW of laser power using a Horiba Scientific LabRAM HR.

5.4 Preliminary results on graphene growth from propylene

The aim of our initial studies of graphene growth was to optimize parameters to obtain single layer material. In the early stages, graphene was grown by annealing the Ni films at 650°C and exposure to propylene gas for 5 min. From the Raman bands obtained from the samples produced using these parameters, we found that the graphene films have a relatively intense D band. However single and double layer graphene are successfully grown as inferred from the Raman spectra shown in Figure 5.2. Six samples are taken for the comparison in the Figure 5.2 using similar processes as explained in 5.3, with all samples annealed at 650°C and exposure to propylene for 5 min. All samples have slightly differences in the Raman spectra, but the data are, at least to a good approximation, reproducible.

As discussed in previous chapters, the signature of single layer graphene is a single Lorentzian 2D band (Pollard et al., 2009; Ferrari et al., 2006). It is estimated

that single layer graphene has FWHM of 2D band of around ~35 cm^{-1} or less. However, if the band exhibits single Lorentzian with very large FWHM (~50 cm^{-1}), the film is turbostratic graphite. Bernal stacked double layer graphene is easy to distinguish from single layer since its 2D band does not exhibit a single Lorentzian, but it consists of four components due to different electron dispersion energy (Ferrari et al., 2007; Malard et al., 2009). Another characteristic for single layer is to have 2D band intensity, $I_{2D}/I_G > 1$.

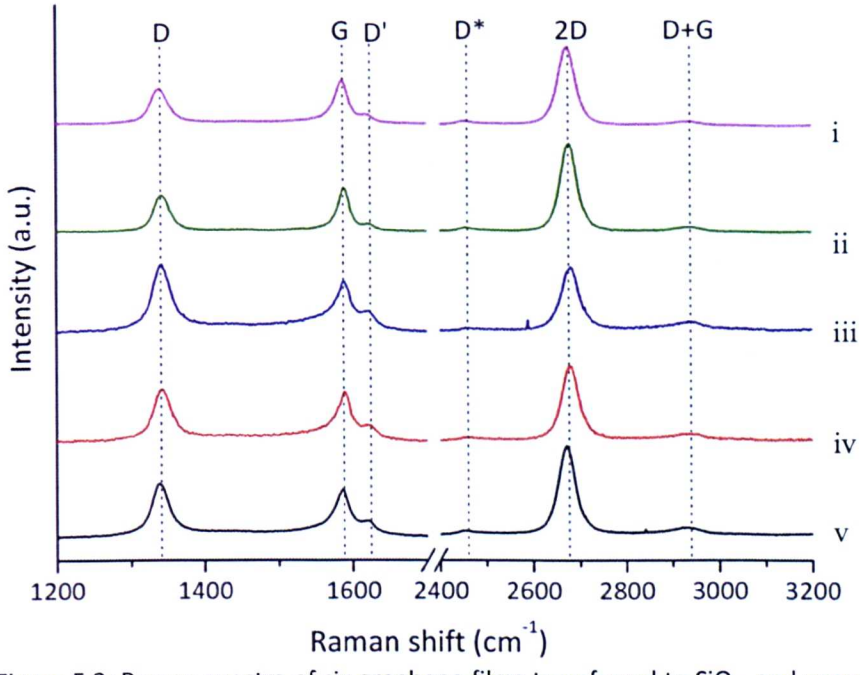

Figure 5.2: Raman spectra of six graphene films transferred to SiO_2, and prepared using the same growth parameters; annealing at 650°C and exposure to propylene for 5 min. The samples are cooled in 15 sec.

Raman spectra in Figure 5.2 are acquired for graphene films on SiO_2. The spectra confirm that the graphene films obtained from the method explained above produce single layers. This is indicated by the full width half maximum (FWHM) of 2D bands which are between 36 to 39 cm^{-1} and the intensity ratio I_{2D}/I_G between 1.5 to 2.1 in Table 5.1. However the D band intensity is high compared with exfoliated graphene. Data from the Raman spectra obtained in Figure 5.2 is presented into

Table 5.1, indicates the defect, or disorder induced, D band intensity ratio I_D/I_G is between 0.8 to 1.5. This is slightly lower than D band intensity obtained in Chapter 4 for graphene growth by immersion in acetone. However the defects and degree of disorder need to be reduced in order to acquire good quality of graphene films. To achieve this objective, a series of experiments is performed by fine-tuning some growth parameters such as annealing temperature and time dependence of Ni film exposure to propylene. The influence of thickness of the Ni thin film is also investigated. Further work on reducing the graphene defects is discussed in the subsequent section.

Table 5.1: Summary of measured values obtained from the Raman spectra of transferred graphene (refer Figure 5.2). All the six samples are prepared using the same growth parameters; annealing at 650°C and exposure to propylene for 5 min. The samples are cooled in 15 sec.

Samples	D band		G band		2D band		
	I_D/I_G	Position (cm^{-1})	Position (cm^{-1})	FWHM (cm^{-1})	I_{2D}/I_G	Position (cm^{-1})	FWHM (cm^{-1})
i	0.8	1341	1586	24.4	1.9	2674	38.0
ii	0.9	1343	1588	20.5	2.1	2677	36.2
iii	1.5	1343	1587	45.3	1.5	2679	38.6
iv	1.2	1343	1587	20.5	1.8	2678	37.2
v	1.2	1341	1585	24.4	2.1	2672	37.1

5.5 Effects of annealing temperature, exposure time and Ni film thickness on graphene quality

To optimise graphene quality we first investigated the effect of exposure time on the Raman spectral features. The exposure to propylene was varied from 3 to 25 min while maintaining annealing temperature, pressure and Ni film thickness. It is observed that at 3, 5 and 10 min exposure to propylene, the D band intensities are significantly high ($I_D/I_G>1$). However, the D band intensity started to reduce when the exposure time is increased up to 20 min with intensity ratio I_D/I_G of ~0.8.

Longer exposure time of more than 25 min do not reduce the I_D/I_G intensity. Hence the quality of graphene film appears to be slightly improved at an exposure time of 20 min.

As a next step the annealing temperature was varied. Raman spectra of Figure 5.4 compares different annealing temperature at 20 min exposure time. The I_D/I_G intensity for annealing temperature at 600°C is the highest (~2.1) and produced few-layer graphene, indicating that this is not an appropriate temperature to produce good quality single layer graphene. Reduction of the I_D/I_G intensity from 0.8 for 650°C to 0.2 for 700°C suggests the film quality increases significantly over this temperature range. It has been argued that defects are high in low-temperature growth, while high temperature growth facilitates relaxation of metal-carbon system toward thermal equilibrium, hence defects can anneal rapidly (Banhart et al., 2011).

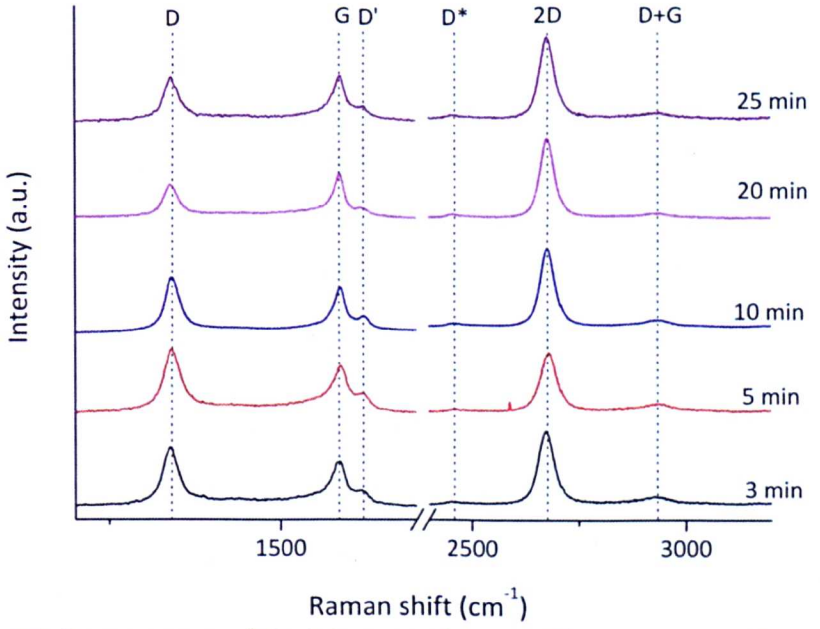

Figure 5.3: Raman spectra of single layer graphene at different exposure time to propylene. The Ni films (100 nm) are annealed at 650°C, pressure in propylene at 1 x 10^{-6} mbar.

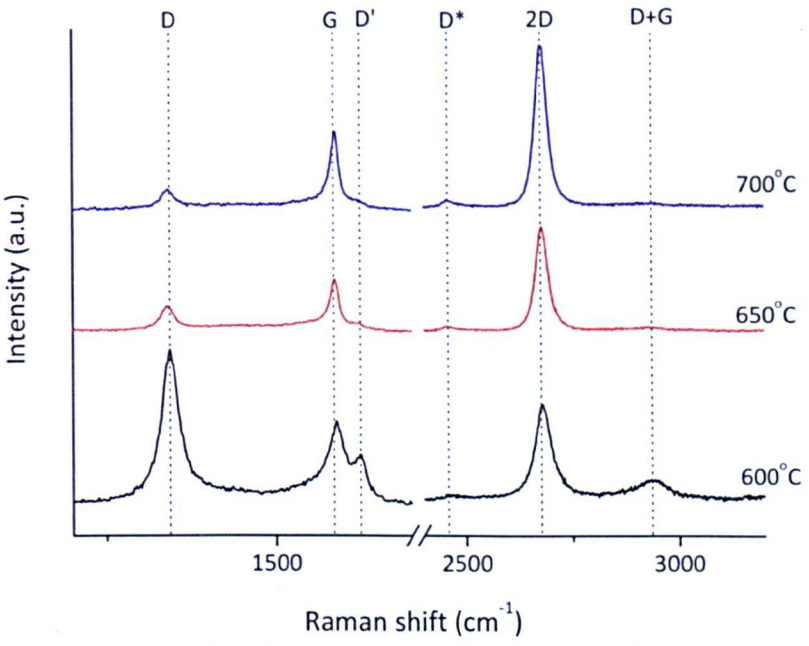

Figure 5.4: Raman spectra of graphene shows increasing Ni film annealing temperature of 600°C, 650°C and 700°C significantly reduce the D band intensity. Ni films are exposed to propylene for 20 min in pressure of 1 x 10^{-6} mbar.

A further increase of annealing temperature is performed to observe changes in the Raman D band intensities as shown in Figure 5.5. All the graphene films in the figure have I_D/I_G intensities of ~0.2 which indicate that further annealing above 700°C up to 850°C does not reduce the amount of defects. This suggests that for annealing temperatures above 700°C, the relaxation of the metal-carbon system has achieved thermal equilibrium, hence the amount of defects as obtained from the Raman spectra do not reduce further.

A detailed study of Raman spectra in Figure 5.5 is given in Figure 5.6. The G band position (Pos(G)) in Figure 5.6(a) varies between 1581 cm^{-1} to 1587 cm^{-1}. The G band FWHM (FWHM(G)) for 700°C and 750°C are at ~20 cm^{-1}, while 800°C and 850°C are at 34.7 cm^{-1} and 36.5 cm^{-1} respectively. This data is in the same range as the data from Lespade et al., 1984, for graphene with a D band. Casiraghi et al., 2007 suggests that large FWHM (G) (>16 cm^{-1}) and Pos (G) higher than 1580 cm^{-1} indicates structural disorder.

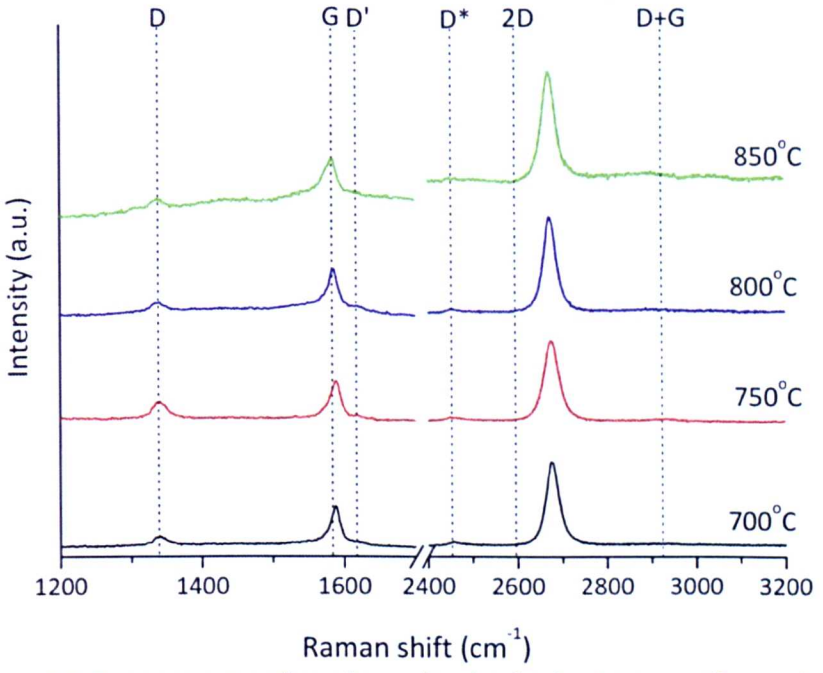

Figure 5.5: Raman spectra of graphene showing further increase of annealing temperature causing a slight decrease in the D band intensity. The 100 nm Ni films are exposed to propylene for 20 min in pressure of 1 x 10^{-6} mbar during annealing.

To analyse the 2D band, the I_{2D}/I_G ratio is plotted as a function of Pos(G) as shown in Figure 5.6(b). The plot shows that the I_{2D}/I_G ratio increases with annealing temperature, with 850°C showing the highest value. Annealing temperatures of 700°C and 750°C give I_{2D}/I_G of 2.3 and 2.2 respectively. As shown previously in Table 5.1, the I_{2D}/I_G ratio for 650°C are between 1.5 to 2.1, which is lower than the ratio shown in Figure 5.6(b). The plot also indicates that higher Pos(G) is correlated with lower I_{2D}/I_G intensities. Overall, all the four temperatures have shown I_{2D}/I_G value consistent with single layer graphene.

Figure 5.6(c) shows Pos(G) as a function of Pos(2D). The 2D band position (Pos(2D)) for the four annealing temperatures is between 2672 cm^{-1} to 2677 cm^{-1} which is in the same range with Pos(2D) for suspended graphene obtained by Berciaud et al., 2009. The figure clearly shows that both Pos(2D) and Pos(G) decrease with higher temperature.

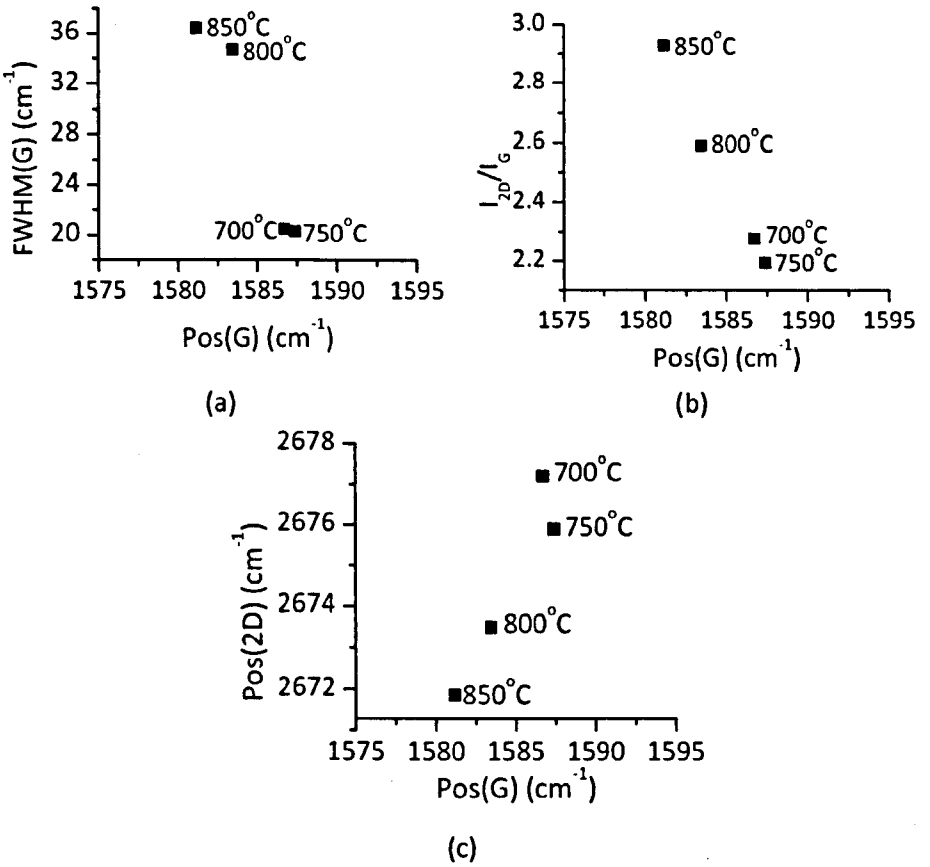

Figure 5.6: (a) FWHM of G band and position of G band (b) I_{2D}/I_G intensity ratio vs. position of G band (c) I_{2D}/I_G intensity vs. annealing temperature for graphene growth (d) position of 2D band vs. position of G band.

Images acquired using optical microscopy for graphene-terminated Ni films (prior to transfer) are shown in Figure 5.7. As the annealing temperature increases, the Ni film restructures with the formation of holes (this is probably due to de-wetting) and the resulting holes can be seen in Figure 5.7b) to 5.7d). The transferred graphene from these Ni films contain holes of the same dimension as those in the Ni layer. Whether graphene is formed inside the holes is unknown but it is not transferred. At annealing temperatures above 900°C much larger holes are present in the Ni film and no graphene is transferred.

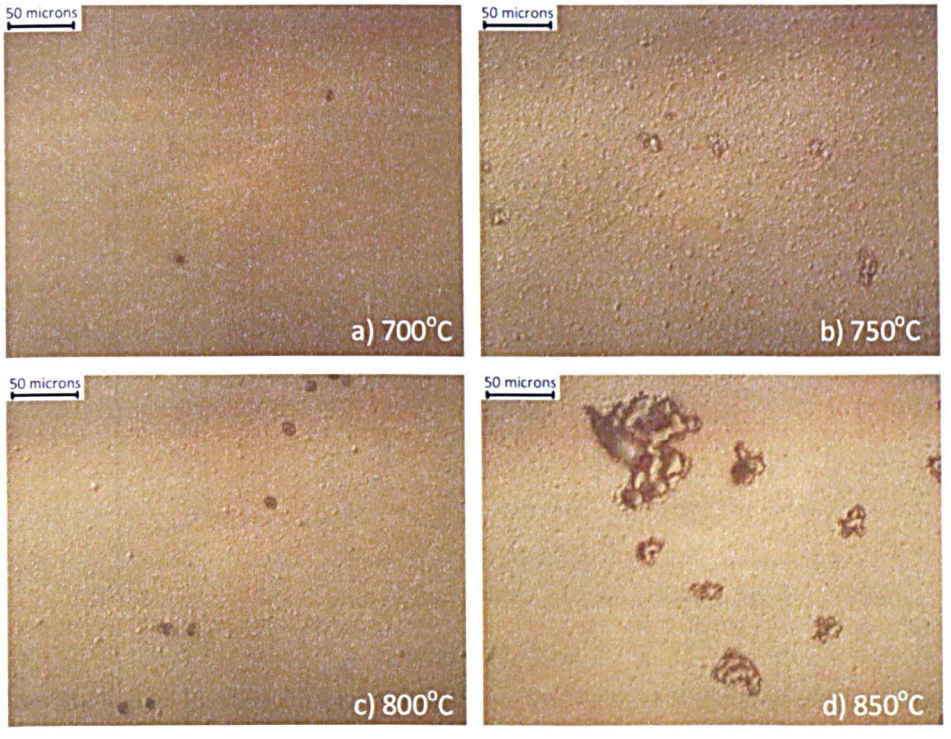

Figure 5.7: Optical micrographs of graphene on Ni (100 nm) at different annealing temperature. All the samples are exposed to propylene for 20 min at a pressure 1 x 10^{-6} mbar.

Based on the Raman spectra in Figure 5.5 and the optical images in Figure 5.7, the Raman D band intensities do not change significantly at annealing temperatures above 700°C. However the presence of holes in the Ni films annealed above 750°C cause a reduction in the graphene coverage. We suggest that the holes are formed due to the high temperature that cause some Ni to evaporate or de-wet the surface, indicating that a Ni film thickness of 100 nm is insufficient for higher annealing temperature. Accordingly we have investigated thicker Ni films. Two samples with a thickness 250 nm were annealed at 750°C and 800°C by exposing to propylene for 20 min in pressure of 1 x 10^{-6} mbar. The Raman spectra of the 250 nm Ni films are shown in Figure 5.8 and can be compared with the 100 nm Ni films in Figure 5.5.

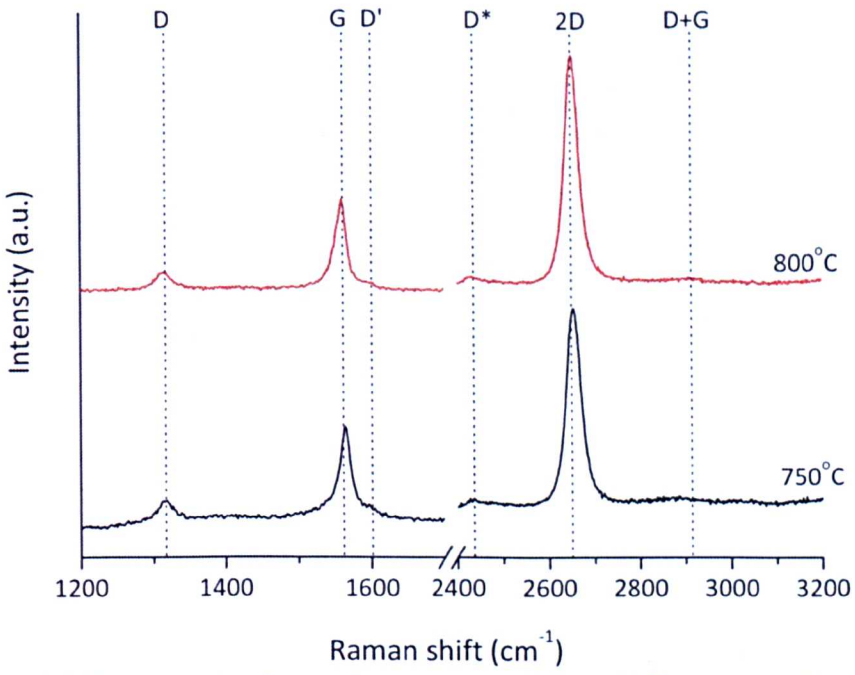

Figure 5.8: Raman spectra for graphene grown on 250 nm Ni films at annealing temperature of 750°c and 800°C. Both samples were exposed to propylene for 20 min, in pressure of 1 x 10^{-6} mbar. Raman spectra obtained for graphene transferred to 90 nm SiO_2 substrate.

The I_D/I_G intensities for the 750°C and 800°C are 0.3 and 0.2 respectively which indicate that thicker Ni films does not improve the quality of the graphene films any further. We suggest that the thicker Ni films may improve the surface morphology by providing enough Ni (as shown in Figure 5.9) however it do not influence the defects formation since it only occur on the surface along with graphene formation. Optical micrographs of both samples (250 nm Ni films) are shown in Figure 5.9, exhibit good surface morphology with small area with thin holes. The holes area for 250 nm Ni annealed at 750°C is 770 μm^2, smaller than holes area formed on 100 nm Ni annealed at the same temperature which is 1 x 10^3 μm^2. The holes area for 250 nm Ni annealed at 800°C is 297 μm^2, which is also smaller than holes area for 100 nm Ni (793 μm^2).

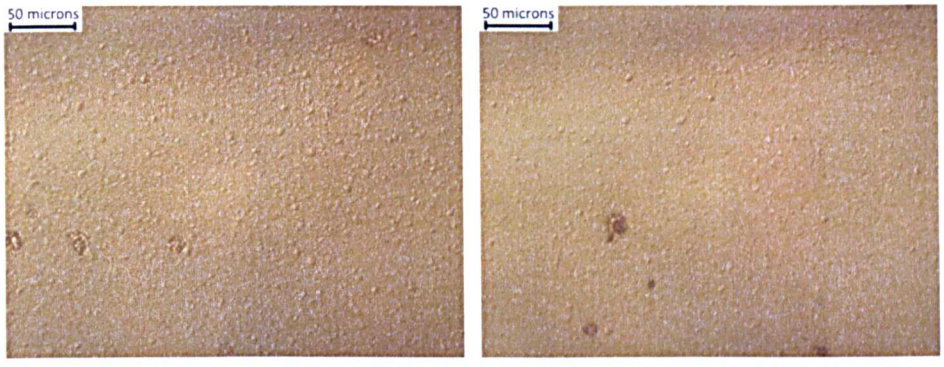

(a) (b)

Figure 5.9: Optical micrographs of graphene on Ni (250 nm) in Figure 5.9. Both samples were annealed at (a) 750°C and (b) 800°C. All the samples are exposed to propylene for 20 min in the pressure of 1×10^{-6} mbar.

We also investigated the surface of these Ni films with AFM. The AFM images are shown in Figure 5.10. The image of the Ni film annealed at 750°C in Figure 5.10(a) is a 10 μm scan and has RMS roughness of 39.8 nm. Figure 5.10(b) is a 1 μm scan of the same sample which shows a faceted island with width of about 0.4 μm. The Ni film annealed at 800°C is shown in Figure 5.10(c) (10μm scan) and has RMS roughness of 32.5 nm. The same sample (1 μm scan) in Figure 5.10(d) shows a larger faceted island than the sample annealed at 750°C with width of 0.8 μm.

So generally, this work has shown a significant 10x reduction of D band intensity and we found that the amount of defects in graphene is a minimum at an annealing temperature of 700°C and exposure to propylene for 20 min. We also suggest that the thickness of the Ni film only play a role in improving Ni morphology however it does not influence the defect formation.

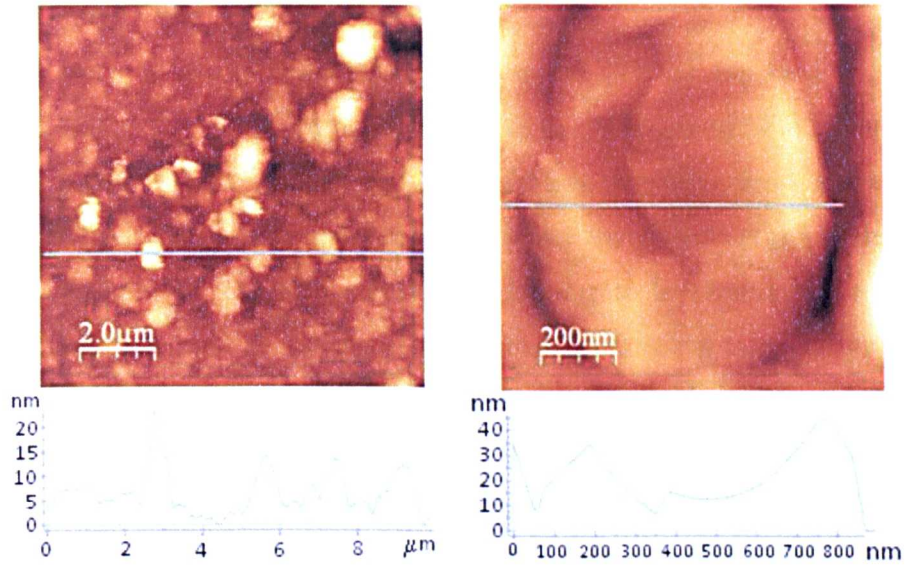

(a) (b)

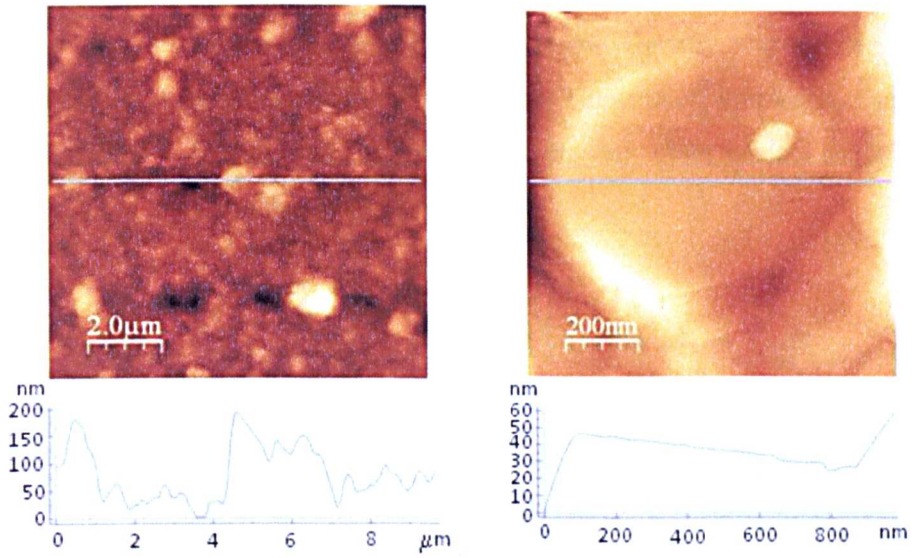

(c) (d)

Figure 5.10: AFM images and height profiles of graphene on 250 nm Ni thin films. (a) and (b) are Ni films annealed at 750°C, (c) and (d) Ni films annealed at 800°C. Both samples are exposed to propylene for 20 min in the pressure of 1 x 10^{-6} mbar.

5.6 Summary

In this chapter graphene growth on Ni film by exposure Ni surface to propylene in vacuum was presented. This approach is successful in producing single layer graphene with relatively high Raman D band intensity. Work is carried out to reduce the defect density and it has been shown that defects in graphene (based on D band intensity) are at minimum at annealing temperatures above 700°C and exposure to propylene for more than 20 min. Annealing temperatures between 800°C to 900°C cause the Ni films to restructure with the formation of holes. Initially we suggested that thicker Ni films could provide enough Ni so that the defects in graphene could be reduced and its coverage will be larger due to reduction of the holes. However, it is found that thicker Ni films do not affect the defect formation, but do improve the Ni surface morphology.

Overall, we have successfully reduced the intensity of the defect peak by a factor of 10 in the graphene films formed on Ni films using propylene. Thus we have demonstrated considerable progress towards our objective to acquire a large coverage of low defective graphene.

Chapter 6

Graphene Formation by Decomposition of C_{60}

6.1 Introduction

It is known that annealing Ni films on SiO_2 can lead to the formation of graphene on the Ni surface due to unintentional introduction of carbon, such as carbon containing adsorbates, or the intentional introduction of carbon sources, for instance gaseous hydrocarbons (Li et al., 2009; Yu et al., 2008; Reina et al., 2009; Kim et al., 2009; Usachov et al., 2008), organic solvents (Muller et al., 2009; Pollard et al., 2010) and solid sources (Sun et al., 2010). In this chapter the growth of graphene from the intentional inclusion of the fullerene, C_{60}, is discussed. Two methods of C_{60} decomposition are investigated; buried C_{60} under a Ni film and C_{60} sublimed on top of a Ni film. Both methods result in a graphene layer formed on top of Ni surface. Note that the buried layer was investigated to verify the conclusion in Chapter 4 that unintentional carbon impurities buried at the Ni/SiO_2 interface can give rise to the formation of graphene.

In the first part of this chapter basic techniques and properties used in the sample preparation will be described. The release-transfer of the graphene films to SiO_2 is achieved using a similar approach to that described in Chapter 3, 4 and 5. The transferred graphene film on SiO_2 is then characterized using Raman spectroscopy.

Both approaches will be discussed in the light of Raman spectra obtained from three different annealing temperatures (710°C, 766°C, 825°C). In addition, the adsorption and transformation of C_{60} to graphene caused by annealing is monitored using vacuum-STM and ambient-STM.

The main objective of this work is to investigate an alternative solid-state approach for the formation of graphene with controlled layer thickness. Particularly, this work is carried out to prove that is possible to form single layer graphene from the decomposition of C_{60}. This method provides a route to control the total dosage of carbon introduced into the film with a high degree of precision.

6.2 Sample preparation

Two methods are used which differ in the order that the C_{60} and Ni film were deposited. In the first method C_{60} is deposited on SiO_2, followed by Ni film deposition on C_{60}. In the second method C_{60} is deposited on Ni film. Initially, the SiO_2 substrates are loaded in a vacuum system with base pressure of 1×10^{-9} to 10^{-10} mbar. The samples are outgassed in 1×10^{-8} mbar pressure at ~500°C for about 12 to 18 hours followed by annealing at 800°C for over one hour. Based on the discussion in Chapter 4, omission of this step causes graphene formation on Ni film even in the absense of the intentional introduction of carbon.

For C_{60} deposition, a Knudsen cell is used to sublime C_{60} molecules at constant temperature with a deposition rate of 0.16 nm/min. It is calculated that 0.8 nm of C_{60} is equivalent to a single layer of C_{60} and has a surface density of 1.2×10^6 molecules/μm^2. After Ni and C_{60} deposition, the samples are annealed at temperatures between 650°C and 890°C for 2 to 15 min by flowing current through the silicon heater at the back of the sample (see Chapter 2). After this the sample is cooled by reducing the current to zero over 15 seconds.

The graphene films formed on the sample surface are transferred to 90 nm SiO_2 subsrates using the same method as described in Chapter 3 and Pollard et al., 2009. These films are optically visible. To confirm that the obtained film is graphene and to determine the quality and number of layers, Raman spectroscopy is used. The Raman spectra in this chapter were acquired with a 50x objective at 532 laser excitation and 1 μW of laser power using a Horiba Scientific LabRAM HR. The STM images are scanned using the Nanograph Systems microscope in vacuum at room temperature using Pt/Ir cut tips. The ambient STM is performed using Molecular Imaging (Agilent) also using Pt/Ir cut tips.

6.3 Buried C_{60} under a Ni thin film

The first part of the work is performed with C_{60} deposited on SiO_2 followed by deposition of a Ni film. The deposition of a C_{60} layer with average thickness ~1.6 nm leads to island formation on the surface with typical heights of ~14 nm, island width of 40 nm and separation between islands of 100 nm. The AFM images of the islands are shown in Figure 6.1 and are consistent with a Volmer-Weber growth mode for C_{60} on SiO_2. Ni deposition on C_{60} covers the islands and produces a similar topography which shows that Ni deposition does not strongly affect the C_{60} islands. However, following the annealing process, the topography of the islands are significantly flattened. It is observed that the surface is covered with polycrystalline facets which are similar to those typically observed for annealed Ni film without the insertion of C_{60}. The transformation from islands to a flat surface shows a significant reordering of surface constituents (Perdigao et al., 2011).

Graphene formed on the Ni surface is released and transferred to SiO_2. Figure 6.1e shows Raman spectra of transferred graphene for samples annealed at 710°C, 766°C and 825°C for 15 min. The samples annealed at 880°C provided no transferred graphene. The Raman spectra in Figure 6.1e confirm that graphene films

are successfully grown on Ni films and may be transferred to a SiO_2 substrate. The Raman bands observed are identified as D, G, D', 2D and D+G bands.

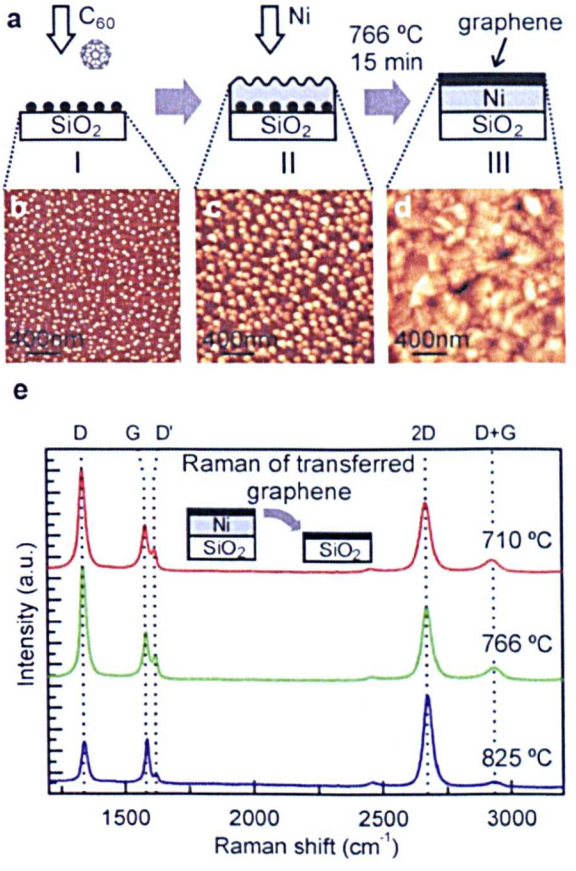

Figure 6.1: Graphene produced from buried C_{60} under a Ni film. a) Sample preparation and graphene growth process in a UHV system: (I) 1.6 nm of C_{60} deposited on a pre-outgassed SiO_2 surface, (II) nickel film grown by evaporation, and (III) the whole assembly was annealed at a chosen temperature for 15 min. b), c), and d) are tapping mode 2 × 2 μm AFM images of the samples taken out after each of the stages I, II, and III, respectively. e) is the Raman spectra of transferred graphene prepared at different annealing temperatures given, with the peaks D, G, D', 2D, and D + G assignment shown with dashed lines.

The spectra in Figure 6.1e show that the I_{2D}/I_G ratio increases with higher annealing temperatures. The spectra suggest that higher annealing temperature gives rise to a lower number of graphene layers (refer Chapter 2). Table 6.1 shows selected peak intensities for each temperature. The I_D/I_G intensity (>2) is high which

indicates a large amount of defects or disorder in the graphene film. Based on the investigation of the relation between the cooling rate and reduction of defects on graphene film, it is believed that the post annealing cooling rate plays an important role in improving graphene film quality since it limits carbon segregation and solvation during graphene grown by CVD (Yu et al., 2008).

Table 6.1: Summary of measured values obtained from the Raman spectra of transferred graphene (refer Figure 6.1e), prepared with buried C_{60} under Ni film and annealed at different temperatures.

Samples	Anneal temperature (°C)	D band	2D band		
		I_D/I_G	I_{2D}/I_G	Position (cm^{-1})	FWHM (cm^{-1})
1	710	2.31	1.61	2674	41.3
2	766	2.64	1.68	2676	37.7
3	825	0.95	2.18	2677	35.6

The effect of varying C_{60} dosage is investigated and the difference can be seen clearly in Figures 6.2a and 6.2b. The C_{60} exposure for 5 min (which results in 0.8 nm thick C_{60} coverage) produces isolated graphene islands with near circular form. The diameters and the separations of the graphene circles are ~10 μm. However, the 10 min C_{60} exposure (of 1.6 nm thick C_{60} coverage) produces a large near complete graphene film coverage. The graphene for film coverage is corresponds to darker contrast regions while lower contrast refers to SiO_2 substrate.

The Raman spectrum of 5 min and 10 min exposures are represented by the red and green spectrum respectively. It is clearly observed that 10 min exposure produces multilayer films based on the low 2D band intensity with $I_{2D}/I_G < 1$, while the 5 min exposure has an I_{2D}/I_G ratio of ~2 which is consistent with a single layer. Comparison between exposure times shows that higher exposure produces higher coverage hence higher number of layers are obtained. This demonstrates that the thickness of the graphene layer can be controlled by varying the C_{60} coverage.

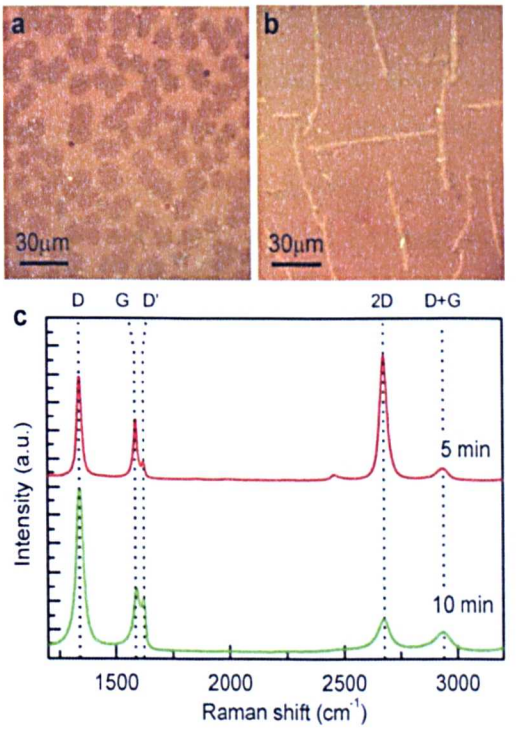

Figure 6.2: a) and b) are 150 x 150 μm optical microscope images of graphene transferred to SiO_2 which were produced with buried C_{60} sandwiched between SiO_2 and Ni film. a) is 5 min exposure to C_{60} results in 0.8 nm thick coverage and b) 10 min exposure to C_{60} results in 1.6 nm thick coverage. Darker and lighter contrasts are graphene and bare SiO_2, respectively. c) is the Raman spectra of the graphene regions in images a) green and b) red.

The fraction of carbon atoms that have been deposited which are incorporated in graphene film can be estimated. A C_{60} layer of average thickness 0.8 nm is equivalent to ~1 single layer of C_{60}, which has sufficient carbon to form ~3.2 single layers of graphene. However based on Figure 6.2, exposing the Ni film for 5 min produced 0.8 nm C_{60} layer which results in overall coverage of ~50% or 0.5 single layer graphene. We suggest, there are possibilities that the remaining carbon grows into pyrolitic carbon (PyC) at the interface of Ni and SiO_2 or remains dissolved within the Ni film. Accordingly, we checked the SiO_2 surface by etching the Ni film and this results in carbon layers remaining on the substrate. Raman spectroscopy and optical imaging are carried out and it was confirmed that the layer formed is

PyC based on its wide D and G bands as shown in Figure 6.3, similar to the spectra observed for PyC formed by CVD (Kumar et al., 2010).

In addition, the results show that graphene initially grows as a single layer due to nucleation. In terms of number of layers, the use of buried C_{60} is comparable to the use of amorphous carbon (Zheng et al., 2010) although there are differences in the Raman spectra observed for the fullerene source of carbon. In particular, the 2D band is narrower and higher in intensity, as compared with films grown from amorphous carbon.

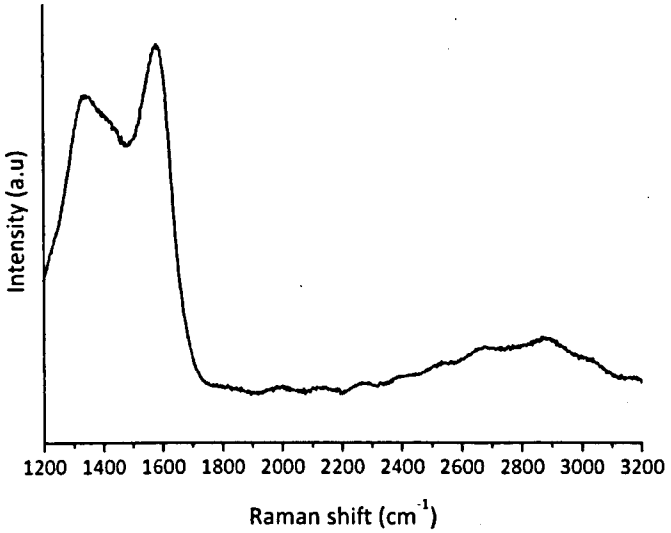

Figure 6.3: Raman spectrum of pyrolitic carbon (PyC) on SiO_2 after Ni etch.

6.4 C_{60} deposited on a Ni thin film

The samples prepared in this section were deposited with the same dosage as described above and annealed at 710°C, 766°C and 825°C for 15 min. The Raman spectra of the resulting graphene after the released-transfer process is shown in Figure 6.4. The peak intensities for the three different temperatures are specified in Table 6.2. By comparing the intensity of the 2D band in Figure 6.4b with Figure 6.1e, it is clear that the I_{2D}/I_G of C_{60} on Ni is generally higher than buried C_{60} under Ni film.

This suggests that the method of depositing C_{60} on Ni produces a higher fraction of single layer graphene. Moreover samples produced using this method have smaller FWHM and less variation with annealing temperature. This indicates that single layer graphene is best achieved with C_{60} deposited on Ni rather than buried C_{60} under Ni film.

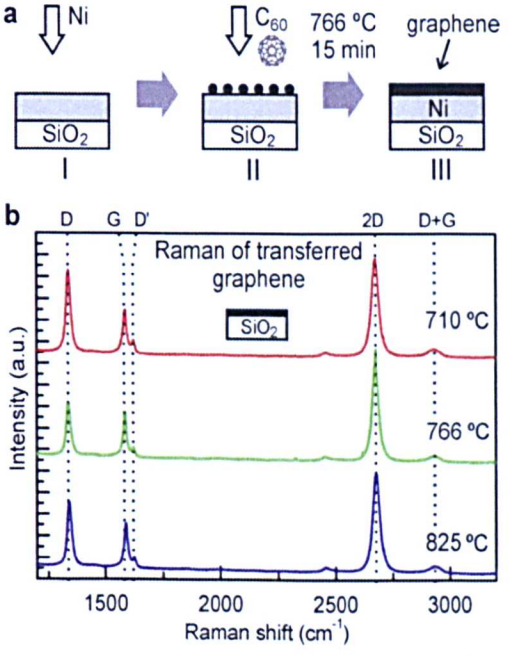

Figure 6.4: Graphene on SiO_2 which is synthesized from 1.6 nm C_{60} on Ni film. a) is the method of graphene growth using C_{60} deposition: I) Ni film is deposited on outgassed SiO_2 substrate, II) Exposure of the Ni film to C_{60} and III) the sample is annealed for 15 min producing graphene on top of Ni film surface. b) Raman spectra of post-transferred graphene on SiO_2 at different annealing temperature.

Based on the I_{2D}/I_G and the FWHM of the 2D band, we also suggest that single layer graphene is best achieved at higher temperatures in the range 760°C to 825°C. This is consistent with previous works (Shelton et al., 1974; Fujita et al., 1994; Eizenberg et al., 1979) that show higher-temperature annealing of Ni implanted with carbon produces a lower number of graphene layers. However, the sample annealed at 880°C did not provide graphene in common with the previous section. The D band intensity for C_{60} on Ni film is high. However, from a comparison of the D band

intensity (I_D/I_G) between Table 6.2 and Table 6.1, the C_{60} on Ni film has lower defects or disorder of graphene film which indicates that this approach produces better graphene quality.

Table 6.2: Summary of measured values obtained from the Raman spectra of transferred graphene (refer Figure 6.3b), prepared with C_{60} on Ni film and annealed at different temperatures.

Samples	Anneal temperature (°C)	D band	2D band		
		I_D/I_G	I_{2D}/I_G	Position (cm^{-1})	FWHM (cm^{-1})
4	710	1.94	2.33	2670.0	34.9
5	766	1.26	2.40	2674.3	31.0
6	825	1.53	2.39	2674.3	33.5

To understand the conversion of C_{60} to graphene, we have monitored the Ni film surface after C_{60} deposition and annealing process using STM. For this purpose we used sapphire as a substrate because the Ni films formed on it are flatter and smoother, making this a good choice of substrate for STM imaging. Figure 6.5 shows STM images of 1 single layer of C_{60} (deposited for 5 min with thickness of 0.8 nm) on Ni/sapphire after annealing.

As observed in the Figure 6.5a, generally the C_{60} arrangement is disordered. However it is possible to determine individual molecules. After annealing at 540°C for 10 min, well ordered hexagonal close-packed islands with height of 0.42 nm are observed as in Figure 6.5b. Previous studies on the absorption of C_{60} on Ni (111) using low energy electron diffraction (LEED) demonstrated that adsorption at room temperature causes a disordered arrangement of C_{60}. However following annealing process, a hexagonally ordered phase is achieved (Kusch et al., 1997). We found that the transition from disordered to well-ordered C_{60} domains occur at ~540°C which is very close to the temperature observed by Kusch et al., 1997.

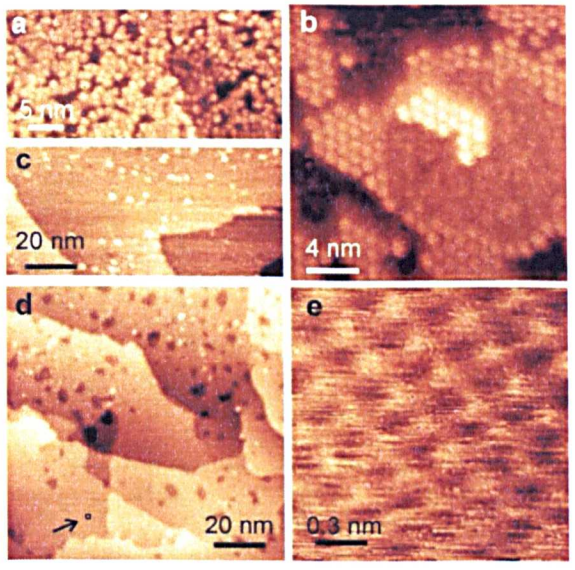

Figure 6.5: Series of STM images of C_{60} on Ni/sapphire. a) STM image of ~1 single layer of C_{60} deposited on 100 nm Ni on sapphire. b) STM image of well-ordered C_{60} islands on Ni/sapphire following annealing at 540°C for 10. c) STM image after additional annealing to 595°C for 10 min. d) ambient-STM image after the sample is taken out from the UHV system to atmosphere. e) ambient-STM image of the square region pointed with an arrow in d). Tunneling parameters are: a-0.5 V, 0.1 nA; b +0.3 V, 0.3 nA; c -1.0 V, 0.1 nA; d -0.3 V, 1.0 nA; e -0.2 V, 1.0 nA. The images are from Perdigao et al., 2011.

The measured intermolecular C_{60} distance of 1.0 nm corresponds to 4 x 4 periodicity with the Ni (111) surface. It is known that surface lattice constant of Ni, a_{Ni} is 0.249 nm which make 4 x a_{Ni} equal to 0.996 nm. At this stage, it is estimated that the C_{60} coverage is ~0.5 monolayers. When the annealing temperature is increased to 595°C, the surface morphology is modified so that the C_{60} domains are no longer present. However the Ni terraces are still observed as before. Hence we suggest that the dissociation of C_{60} occurs between 540°C and 595°C. From all the samples we produced, it is found that graphene is only obtained above 600°C. Previous study on the decomposition and conversion of C_{60} on Ni (110) to graphitic layer has demonstrated a slightly lower temperature of ~490°C (Cepek et al., 1996). We found that additional annealing, above 595°C, between 655°C and 710°C did not show a significant transformation of the observed surface morphology.

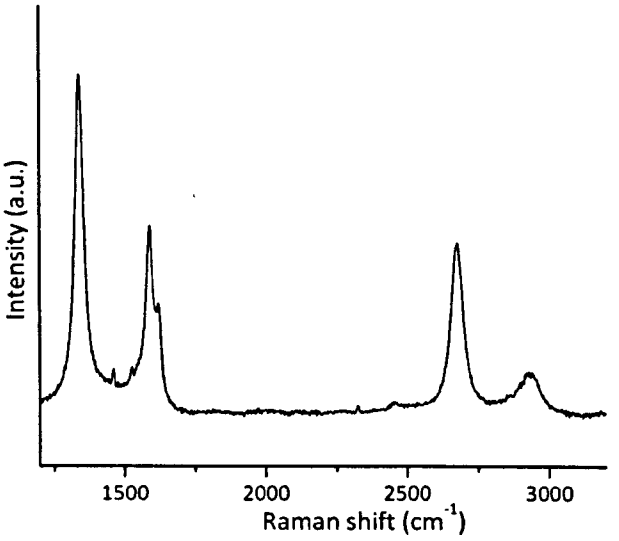

Figure 6.6: Raman spectrum of double layer graphene on SiO_2, which was transferred from C_{60} on Ni/Saph in Figure 6.5.

The sample in Figure 6.5 was taken out of the vacuum system and imaged using an ambient-STM. As shown in Figure 6.5d and 6.5e, generally the surface morphology is comparable to that observed in vacuum. However shallow holes are observed under the ambient-STM (Figure 6.5d). The region pointed by the arrow in the figure is imaged in a higher magnification as shown in Figure 6.5e, which shows a common structure with a period of ~ 0.24 ± 0.01 nm. This is close to the expected surface lattice constant of graphite or graphene and similar to previously published images of graphene on Ni (Usachov et al., 2008; Hofrichter et al., 2010). Raman spectrum (Figure 6.6) shows that the film obtained after a release-transfer process to SiO_2 is double layer graphene. It has been suggested in our previous work (Pollard et al., 2009) that a graphene layer inhibits oxidation of the metal surface and we believe that this assists out work with the ambient-STM. The holes or wells observed in Figure 6.5d have depth up to ~1.5 nm. We suggest that these holes cause defects in the graphene layer which allow, and possibly arise from, localized oxidation of the graphene on Ni surface (Perdigao et al., 2011).

6.5 Summary

In this chapter the decomposition of C_{60} on Ni was presented which ultimately produced single and double layer graphene films. Similar release-transfer method as described in Chapter 3 and 4 is carried out to transfer graphene from the Ni film to a SiO_2 substrate. Further investigation is carried out using Raman spectroscopy to identify the graphene layer. It is found that all the samples have a high fraction of single layer graphene, but are relatively high in defects and disorder which are confirmed by the high intensity of the D bands. The fraction of defects is higher than commonly observed in few-layer graphene grown on Ni film by CVD. It is suggested that the graphene quality can be improved by using other metals or different molecular precursors and at the same time a high fraction of single layer is maintained.

A few factors are identified to influence the characteristics of the resulting graphene film, particularly the coverage of C_{60}, annealing temperature and the sequence of depositing C_{60} and Ni film. This molecular source of carbon provides a method of controlling the total dosage of carbon introduced into the film with a high degree of precision (Perdigao et al., 2011). This work and our previous work (Pollard et al., 2009) suggest that carbon at a buried metal on SiO_2 has the possibility to diffuse and segregate at the top of the surface. Overall, this chapter provides an alternative solid-state approach for the formation of graphene, particularly using C_{60} with the capability to control layer thickness.

Chapter 7

Graphene Enhanced Raman Scattering (GERS) of PTCDI

7.1 Introduction

Surface enhanced Raman scattering (SERS) is a technique which is widely used to enhance a Raman signal. In SERS studies, the emphasis is on increasing the intensity of Raman signals, and this requires a substrate which is cheap and easy to obtain, and is also chemically inert and biocompatible. A candidate which could satisfy this requirement is graphene. Recently, a new approach for enhancing Raman signals of adsorbed molecules using graphene as a substrate has been reported (Ling et al., 2010; Ling & Zhang, 2010), known as graphene enhanced Raman scattering (GERS).

Here we study the GERS effect by investigating the Raman spectrum of PTCDI adsorbed on epitaxial and exfoliated graphene. The first part of this chapter will describe the SERS effect. This is followed by an introduction to PTCDI and the sample preparation methods used for this experiment are then discussed. The Raman spectra of PTCDI will be discussed in detail to demonstrate the enhancement due to GERS. We observed 12 Raman bands of the PTCDI and the assignment of each of the band obtained will be described. Further disscussion of the effect of using single layer and few-layer graphene will be given as well as the effect of varying the PTCDI

coverage. This work has confirmed that graphene is a good candidate as a substrate for Raman enhancement for adsorbed molecules.

7.2 Sample preparation

This work involves deposition of PTCDI molecules on graphene. Graphene films for this work are prepared using propylene, as explained in Chapter 5. After outgassing, a Ni film is deposited on SiO_2. Ni films are annealed at 650°C for 10 min in the presence of propylene. After graphene is formed on Ni surface, it is transferred to SiO_2 substrates as explained in Chapter 3 and Pollard et al., 2009. Before PTCDI deposition, the graphene films on SiO_2 are characterized using Raman spectroscopy.

For PTCDI deposition, a Knudsen cell is used to sublime PTCDI onto a graphene surface with a deposition rate of 0.062 Å/min. To perform the deposition, the Knudsen cell is heated at ~400°C while substrates are held at room temperature. Raman spectra are then acquired using a 50x objective at 532 nm and 1 μW of laser power using a Horiba Scientific LabRAM HR. For the STM images, we prepared graphene on Ni/Saphire/SiO_2/Si and scanned using the Nanograph Systems in vacuum at room temperature using Pt/Ir cut tips.

7.3 Perylene tetracarboxylic diimide (PTCDI)

Perylene derivatives have been widely studied in relation to two-dimensional self-assembly on various substrates and have potential applications in molecular electronics. The adsorption of perylene tetracarboxylic diimide (PTCDI) has been studied on several different substrates (Zahn et al., 2004; Hauschild et al., 2005; Kaake et al., 2007). Many studies using PTCDI are related to hydrogen bonding guided self-assembly by co-adsorption with melamine on silver terminated silicon (Theobald et al., 2003) or on gold surfaces (Perdigao et al., 2006). PTCDI/melamine

arrays form two-dimensional porous nanostructures with hexagonal shape. When deposited without melamine it has been reported that PTCDI molecules can form canted and brick wall structures. The canted structure consists of rows or chains of PTCDI, which are stabilized by hydrogen bonding. The brick wall structure contains rows of PTCDI with the adjacent rows shifted with respect to each other (Mura et al., 2009).

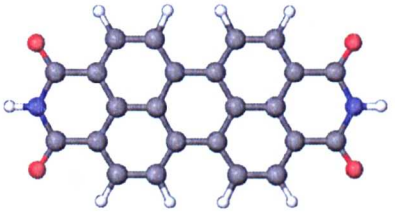

Figure 7.1: Perylene tetracarboxylic diimide (PTCDI) with carbon (grey), hydrogen (white), oxygen (red) and nitrogen (blue).

The investigation of the vibrational spectra of PTCDI is limited even though a complete assignment of IR and Raman spectra of PTCDA is available (Yu et al., 2003). PTCDI is a planar molecule with D_{2h} symmetry point group with 114 vibrational normal modes. 54 of the modes are Raman active, 49 are IR active and there are 8 silent modes (Chiş et al., 2009). The next section will discuss Raman spectra of PTCDI on graphene.

7.4 Raman spectra of PTCDI on graphene

An overview of PTCDI Raman bands will be given before discussing our results for PTCDI on graphene. Chiş and colleagues have recorded Raman spectrum of powder PTCDI and PTCDI dissolved in dimethyl sulfoxide (DMSO) at room temperature (Chiş et al., 2009). From the Raman spectrum of powder PTCDI, the most intense Raman bands are obtained at 1066, 1302, 1377, 1444, 1572 and 1585 cm^{-1}. From the calculated counterparts, all the bands have A_g symmetry, which is an

irreducible representation of D_{2h} point group symmetry. The band at 1066 cm^{-1} corresponds to carbon-hydrogen (CH) in-plane bendings coupled with in-plane rings deformation, and the bands at 1302 cm^{-1} and 1377 cm^{-1} both correspond to single carbon-carbon (CC) stretching coupled with CH in plane bendings (CC + CH), and the band at 1585 cm^{-1} corresponding to CC stretching. However the assignment of the band at 1444 cm^{-1} is not calculated because its intensity is very low, so the assignment for it is unknown. It is also reported that there is a band at 1285 cm^{-1}, corresponds to CC stretching coupled with CH in plane bendings (CC + CH), which has low intensity and appears as a shoulder next to the band at 1302 cm^{-1}. For PTCDI dissolved in DMSO, Raman bands at 1059, 1291, 1375, 1447 and 1571 cm^{-1} are recorded, slightly shifted compared to the bands obtained from powder PTCDI. Note that the spectral resolution of both powder PTCDI and PTCDI in DMSO are 4 cm^{-1} and 10 cm^{-1} respectively.

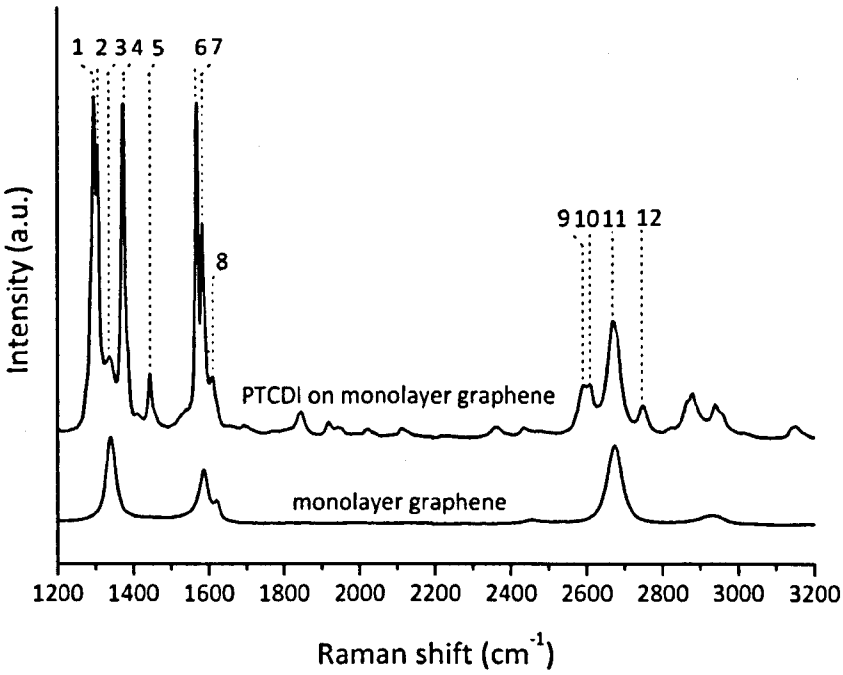

Figure 7.2: Raman spectrum of PTCDI on monolayer graphene. The labels (1 to 12) show most intense Raman bands of PTCDI and graphene.

From our observation on PTCDI on graphene, there are 12 intense Raman bands observed at room temperature. The bands appear at 1293, 1302, 1356, 1371, 1443, 1567, 1581, 1607, 2592, 2607, 2670 and 2747 cm^{-1}. Figure 7.2 gives an overview for the Raman bands of PTCDI on graphene. Raman bands between 1700 cm^{-1} to 2500 cm^{-1} have low intensity and the assignment for these bands is unknown, hence further discussion on these bands will not be included here. The Raman band at 1066 cm^{-1} (which also observed by Chiş et al., 2009) also has very low intensity so will also not be discussed further. The assignments of the Raman bands in Figure 7.2 are given in Table 7.1 based on Chiş et al., 2009.

Table 7.1: PTCDI and graphene Raman bands and its assignment based on Figure 7.2 and Chiş et al., 2009. v represents stretching, δ represents in-plane bending.

Bands no.	Raman shift (cm^{-1})	Assignments
1	1293	PTCDI (no assignment)
2	1302	PTCDI central ring stretch + δ(CH)
3	1356	Graphene D band
4	1371	PTCDI v(CN) + δ(CH)
5	1443	PTCDI (no assignment)
6	1567	PTCDI v(CC) + δ(CH)
7	1581	PTCDI v(CC) and graphene G band
8	1607	PTCDI (no assignment) and graphene D' band
9	2592	PTCDI overtone: 2 x 1293
10	2607	PTCDI overtone: 2 x 1302
11	2670	Graphene 2D band
12	2747	PTCDI overtone: 2 x 1371

As shown in Figure 7.2, the first two bands of PTCDI on graphene occur at wave numbers 1293 cm^{-1} and 1302 cm^{-1}, and are identified as band 1 and band 2 respectively. From a comparison with the powder PTCDI (Chiş et al., 2009), only a

band at 1302 cm^{-1} is observed (no band at 1293 cm^{-1}). However, for PTCDI in DMSO, only a band at 1291 cm^{-1} was obtained (no band at 1302 cm^{-1}). As mentioned before, the spectral resolution for powder PTCDI is higher than PTCDI in DMSO. Note that the reported resolution for the measurement of PTCDI in DMSO is comparable with the spacing of bands 1 and 2, significantly lower than our spectral resolution, 1 cm^{-1}. As observed in powder PTCDI, a shoulder at 1285 cm^{-1} is also resolved in the PTCDI on graphene spectrum in Figure 7.2, but is not observed for PTCDI in DMSO. The band at 1293 cm^{-1} is not observed in powder PTCDI. So both bands at 1293 cm^{-1} and 1305 cm^{-1} (band 1 and band 2) are due to PTCDI, but the assignment for band 1 is unknown. Band 2 corresponds to central rings stretch of PTCDI coupled with CH in-plane bendings (δ(CH)).

The third band at 1356 cm^{-1} (band 3) in Figure 7.2 corresponds to the D band of graphene. The following band at 1371 cm^{-1} (band 4) is a Raman band of PTCDI and corresponds to carbon-nitrogen (CN) symmetric stretching coupled with CH in-plane bendings (ν(CN) + δ(CH)). For the fifth Raman band at 1443 cm^{-1} (band 5) which is also observed by Chiş et al., 2009, the assignment for the band is unknown. The sixth band at 1567 cm^{-1} (band 6) is a CC stretching coupled with CH in plane bendings (ν(CC) + δ(CH)). The seventh band observed at 1581 cm^{-1} (band 7) is a combination of CC stretching in PTCDI (ν(CC)) and graphene G band. A shoulder at 1607 cm^{-1} (band 8) corresponds to the graphene D' band which coincides with a Raman band of PTCDI, but the assignment for the band is unknown. Band 8 is observed for PTCDI on both exfoliated (no D' band) and epitaxial graphene, as be presented in the next section, implying it arises from PTCDI. The ninth and the tenth Raman bands are overtones of PTCDI bands 1 and 2. The eleventh Raman band at 2670 cm^{-1} (band 11) corresponds to graphene 2D band while the last band at 2747 cm^{-1} (band 12) is the overtone of PTCDI band 4.

A comparison of the Raman spectrum of PTCDI with that of the monolayer graphene used in this experiment (with a relatively high D band) is also shown in the Figure 7.2. The three most intense bands of monolayer graphene (D, G and 2D

bands) can be distinguished in the Raman spectrum. As described in 7.2, the enhancement in the Raman signal of PTCDI can be measured by the difference in the intensity of the Raman bands of PTCDI on SiO_2 and PTCDI on graphene. Figure 7.3 compares PTCDI Raman spectra on graphene and on SiO_2. The PTCDI deposition was performed on the same sample which has patches of bare SiO_2 and also single layer graphene. The exposure time for PTCDI sublimation is 5 min which corresponds to 9% of a PTCDI monolayer. Only the four most intense Raman bands are observed in the Raman spectrum of PTCDI on SiO_2. So these four bands of PTCDI on graphene are used to compare with the signal from the signal from the PTCDI on SiO_2. The ratio of the Raman intensities in both spectra gives an average enhancement factor of the Raman signal of PTCDI on graphene of ~13. The bands intensities and ratios are given in Appendix A.

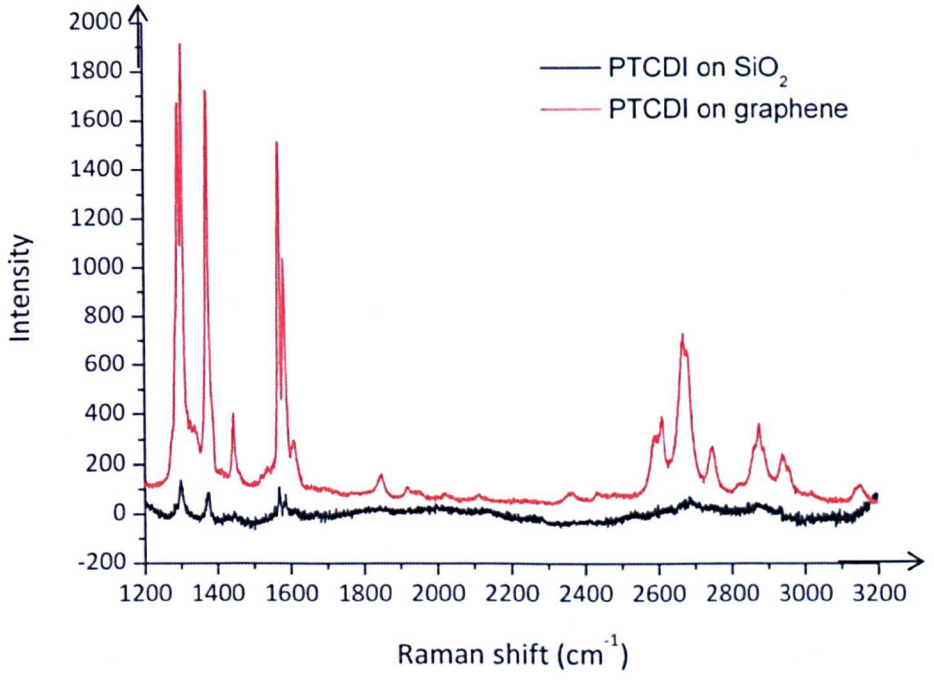

Figure 7.3: Raman spectrum of 9% monolayer PTCDI (5 min) on graphene and on SiO_2.

7.5 PTCDI on exfoliated graphene

We then deposited PTCDI on exfoliated graphene, which is known to be very high quality without a defect induced band (or D band). Figure 7.4 shows three different spectra which were taken on the same sample, before and after PTCDI exposure for 5 min (9% monolayer). Figure 7.4(a) shows Raman spectrum of PTCDI on monolayer graphene and the spectrum of monolayer graphene itself. PTCDI Raman spectrum in Figure 7.4(b) is on few-layer graphene, and 7.4(c) shows PTCDI on graphite.

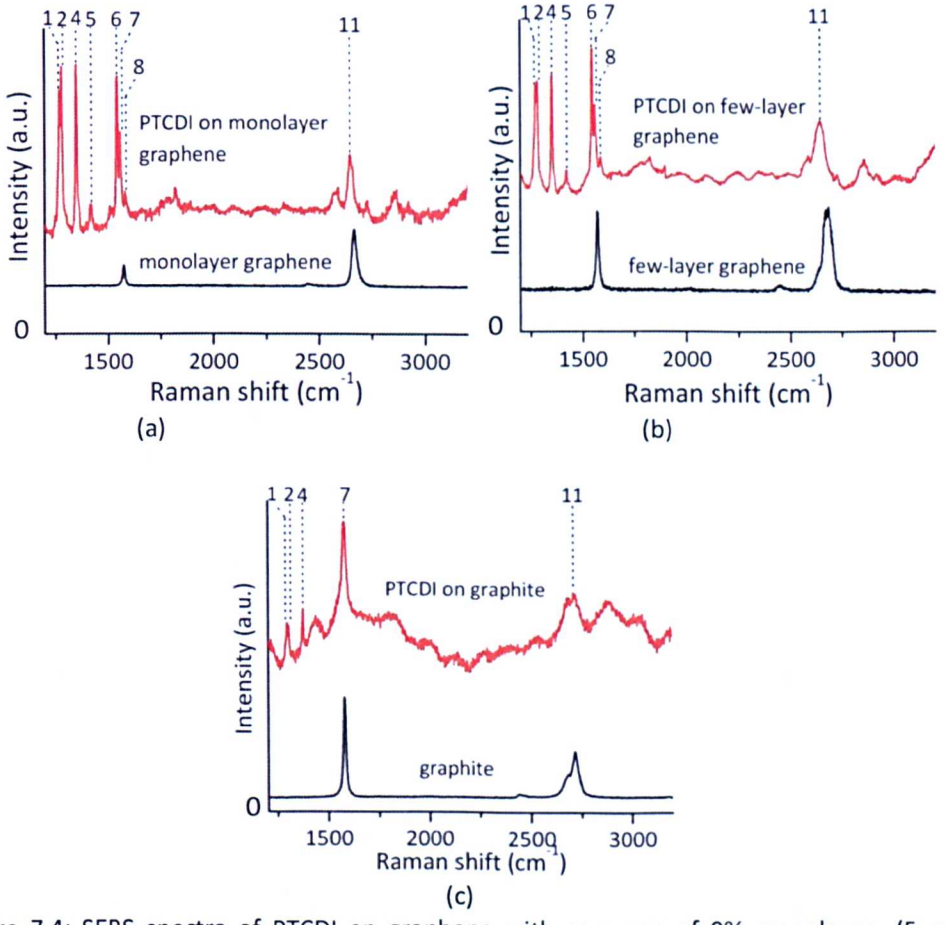

Figure 7.4: SERS spectra of PTCDI on graphene with coverage of 9% monolayer (5 min exposure) (a) PTCDI on monolayer graphene (red) and graphene without PTCDI (black). (b) PTCDI on few-layer graphene (red) and graphene without PTCDI (black). (c) PTCDI on graphite (red) and graphite without PTCDI (black). Graphene and graphite are on 90 nm SiO_2 and prepared by mechanical exfoliation before PTCDI is deposited on its surface.

The graphene layer in Figure 7.4(b) has an intensity ratio I_{2D}/I_G of 0.78 with 2D band FWHM of 38, which most likely to be two or three layers of graphene (Ferrari et al., 2006). The graphite layer in Figure 7.4(c) consists of more than 5 layers of graphene. As expected, it is found that the D band (or band 3) is not present in the PTCDI Raman spectra in Figure 7.4(a), (b) and (c). Amongst the three spectra, it is obvious that Figure 7.4(c) shows the least PTCDI Raman bands. PTCDI band 7 is the most intense band because it corresponds to the typical high intensity of G band in graphite. It can also be seen in Figure 7.4(a) and (b) that Raman bands of the PTCDI on monolayer graphene have higher intensity than PTCDI on few-layer graphene. Band 11 in the three figures ((a), (b) and (c)) is corresponds to the 2D band of graphene.

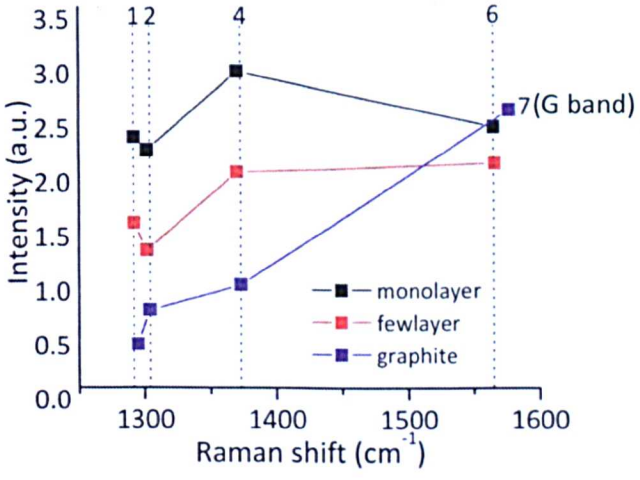

Figure 7.5: Raman bands of PTCDI on monolayer and few-layer graphene (a) direct comparison of PTCDI Raman spectra (b) PTCDI Raman band intensity for bands 1, 2, 4, and 6 (refer Table 7.1).

For clarity, a comparison of PTCDI spectra in Figure 7.4 is shown in Figure 7.5. We find that PTCDI Raman intensity is the highest for monolayer graphene, followed by few-layer and graphite. The Raman intensity of PTCDI on monolayer is 1x higher than the few-layer graphene. The lower intensity for higher number of graphene layers which is demonstrated in the figure is in agreement with work by Ling et al.,

2010. Band 6 is not observed for PTCDI on graphite, but band 7 is prominent due to the high G band intensity in graphite. The data for Figure 7.5 is presented in Appendix B. So generally we have shown that the Raman signal of adsorbed molecules (particularly PTCDI) on single layer graphene is stronger than few-layer graphene and graphite substrates which agrees well with previous studies (Jung et al., 2010; Ling et al., 2010).

To investigate the difference in the Raman intensity of PTCDI on monolayer graphene prepared by mechanical exfoliation and epitaxial process, we compare both Raman spectra as shown in Figure 7.6. The epitaxial graphene was grown according to the method described in Chapter 5 and transferred to SiO_2. The exposure to PTCDI is also performed for 5 min (9% monolayer). It can be seen in Figure 7.6(b) that the intensity difference are apparent in band 2 and band 4 with higher intensity for PTCDI on exfoliated graphene. Overall, the intensity difference between both samples is showing that Raman intensity of PTCDI is not significantly influenced by the quality of graphene.

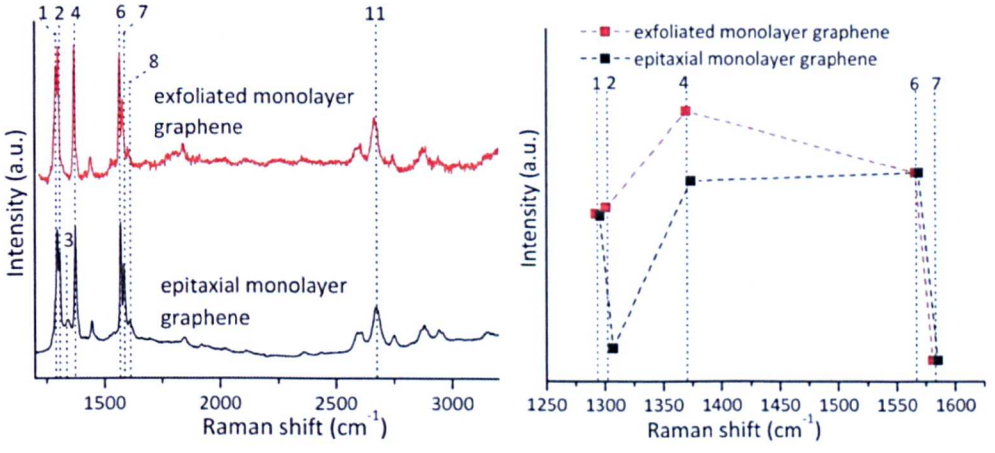

(a) (b)

Figure 7.6 : Raman bands of PTCDI on monolayer and few-layer graphene (a) direct comparison of Raman spectra of PTCDI on exfoliated and epitaxial monolayer graphene. (b) PTCDI Raman bands intensity for bands 1, 2, 4, 6, 7.

7.6 PTCDI on transferred graphene: coverage dependence

Another set of samples were prepared by deposition of PTCDI on transferred graphene (graphene on SiO_2). This section describes the dependence of the Raman spectra on PTCDI coverage. Raman spectra acquired for different PTCDI coverages are shown in Figure 7.7. The figure shows that the PTCDI Raman bands have different intensities relative to the PTCDI exposure dependence.

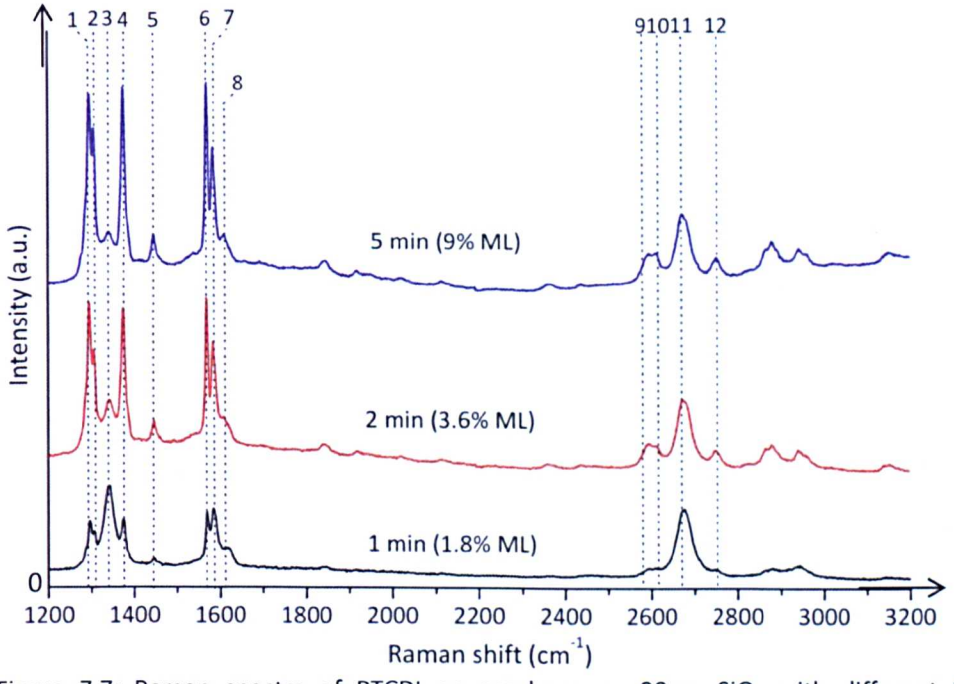

Figure 7.7: Raman spectra of PTCDI on graphene on 90nm SiO_2 with different PTCDI exposures and percentage of monolayer (ML) coverage; 1 min or 1.8% ML (black), 2 min or 3.6% ML (red) and 5 min or 9% ML (blue) .

It is clearly seen that the 1 min exposure has the lowest PTCDI Raman intensity, whereas bands 1, 2, 4, 6 and 7 have lower intensity than the intensity of band 3 which corresponds to defect induced band of graphene. Based on Figure 7.7, the Raman intensity difference is shown in Figure 7.8 by acquiring dominant PTCDI bands (1, 2, 4, 6 and 7) intensities. The figure shows that the 5 min exposure time has Raman bands intensity of 2x higher than the 2 min exposure and 3.5x higher

than the 1 min exposure. The figure also demonstrates that the intensity increases with coverage of adsorbed molecules, as expected.

An analysis is carried out by extracting the Raman band intensities from the three spectra in Figure 7.7. Figure 7.9 shows the Raman band intensities (for bands 1, 2, 4, 6, and 7) for different coverages of PTCDI. It is found that Raman band 6 has the highest intensity. As mentioned before, it corresponds to CC stretching coupled with CH in plane bending. This is followed by Raman band 4 which corresponds to CN symmetric stretching coupled with CH in plane bending. In sequence, Raman bands 1 and 2 have lower intensities. Raman band 2 which is the lowest intensity corresponds to the PTCDI central ring stretch, coupled with CH in plane bending. Band 7 does not follow the intensity difference as observed in other PTCDI bands since it corresponds to graphene G band. The data for Figure 7.8 and 7.9 is presented in Appendix C. Overall, we have shown that the PTCDI molecules can be detected at a small fraction of a monolayer coverage on single layer graphene.

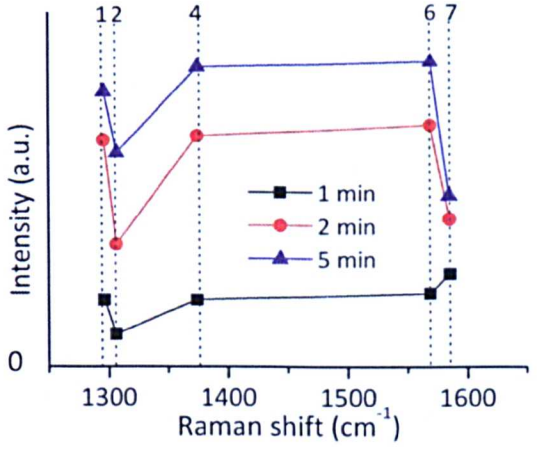

Figure 7.8: PTCDI Raman bands intensity difference from Figure 7.7 relative to PTCDI exposure dependence. PTCDI Raman bands 1, 2, 4, 6 and 7 are taken for comparison.

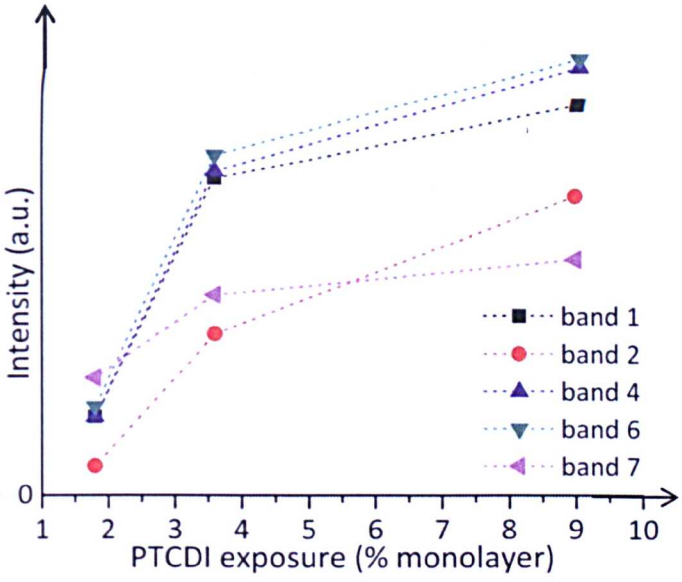

Figure 7.9: Raman bands intensities for different coverages of PTCDI. PTCDI Raman bands 1, 2, 4, 6 and 7 are taken for comparison.

7.7 PTCDI deposited on graphene before transfer

We investigated whether Raman enhancement occurs for PTCDI deposited on graphene-terminated Ni before transfer. In the course of this experiment, we have monitored the adsorption of PTCDI on graphene using UHV STM. For this purpose, sapphire is used as a substrate for the growth of Ni film since this surface is flatter and smoother compared with Ni on SiO_2, making it more easily compatible with STM imaging. The Ni film thickness is 100 nm and the deposition process is described in Chapter 3 and Chapter 4, while the graphene was grown using propylene, as described in Chapter 5.

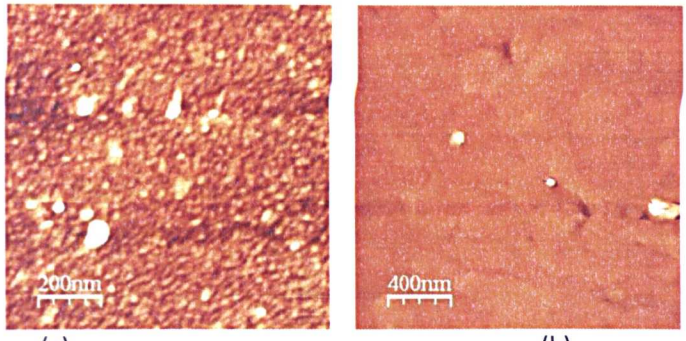

(a) (b)

Figure 7.10: AFM image of as-grown Ni on sapphire substrate with thickness of 100 nm (a) Ni before annealing (b) Ni after annealing at 750°C and exposure to propylene for 10 min.

Figure 7.10(a) shows a 100 nm Ni film on sapphire with a grain size of about 10 to 20 nm. Figure 7.10(b) shows that after annealing at a certain temperature (in this case, the sample is annealed at 750°C and exposure to propylene for 10 min), the Ni grains flatten and form terraces with typical widths of 0.3 μm. This process produced graphene (by exposure to propylene gas) on the Ni film on which PTCDI then deposited.

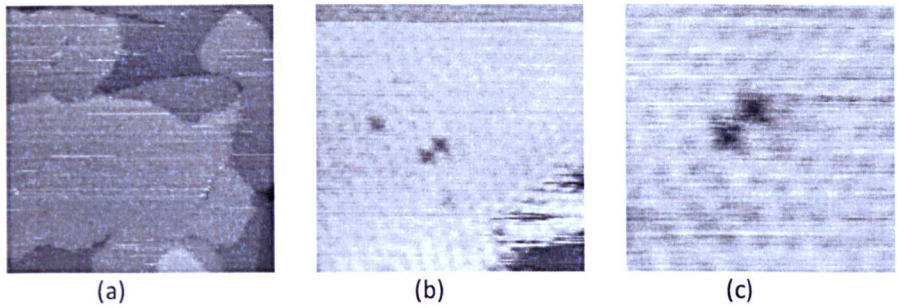

(a) (b) (c)

Figure 7.11: Four STM images of PTCDI monolayers on graphene/Ni/sapphire substrate. (a) image scale 100 x 100 nm, Vs = 1.5V, I = 0.05 nA. (b) image scale 20 x 20 nm, Vs = 1.5 V, I_t = 0.05 nA. (c) image scale 10 x 10 nm, Vs = 1.5 V, I_t = 0.05 nA. Images were taken by L.M.A. Perdigao.

Figure 7.11 shows STM images of a PTCDI monolayer on as-grown graphene on a Ni thin film. Note the coverage of PTCDI in the figure is 0.09 ML. Generally the PTCDI in Figure 7.11(a) forms large domains that span more than 100 nm. At higher resolution (Figure 7.11(b), and (c)), the molecular arrangement within the adsorbed layer may be determined.

We investigated the PTCDI monolayer using Raman spectroscopy before transfering it to a SiO_2 substrate. The Raman spectrum of PTCDI on graphene before transfer (graphene on Ni film) is shown in Figure 7.12. The background spectrum is quite high due to the Ni thin film but the PTCDI bands are clearly resolved. The PTCDI Raman bands observed before transfer are represented by bands 1, 2, 4, 5, 6, and 11. Graphene D and G bands (bands 3 and 7) are not resolved, which may due to the high background signal from Ni film. Graphene 2D band (band 11) is however resolved due to typical high intensity of *2D band of single layer graphene.* Remarkably, after the transfer to SiO_2, all the PTCDI bands are still obtained and have high intensity. Note that both spectra in Figure 7.12 were taken using the same parameters eg. laser wavelength, laser power and laser exposure.

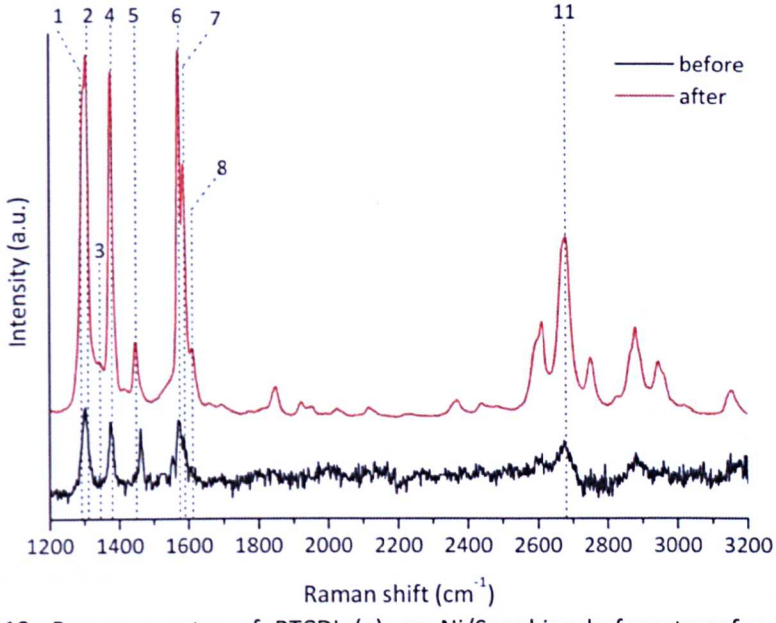

Figure 7.12: Raman spectra of PTCDI (a) on Ni/Sapphire before transfer (the data is increased 30x) (b) on SiO_2/Si after transfer.

After the transfer process, the graphene Raman bands (D, G and 2D bands) are obtained as in Figure 7.12, represented by bands 3, 7, 11. The D band (band 2) is very low suggesting that the graphene layer has a relatively low amount of defects. The intensity difference between both samples is shown in Figure 7.13. The

difference is significantly large whereas the intensity after transfer is 3x higher than before transfer.

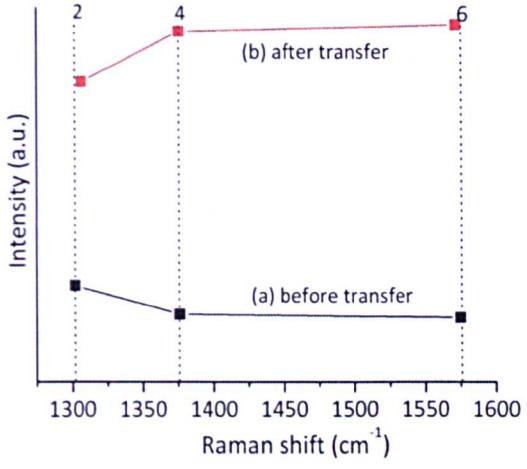

Figure 7.13: PTCDI Raman bands intensities from Figure 7.12 (a) on Ni/Sapphire before transfer (b) on SiO_2/Si after transfer.

The data for Raman band intensities and position are given in Appendix D. As presented in the table, band 2 is shifted 5 cm^{-1} towards higher wave number after transfer, instead band 6 shows a shift of 3 cm^{-1} towards lower wave number. Overall, this work has shown that the PTCDI on graphene is successfully transferred using the same transfer method typically used for graphene and the Raman enhancement of PTCDI on graphene is observed after the transfer.

7.8 Summary

In this chapter, preliminary results of graphene enhanced Raman scattering (GERS) of adsorbed PTCDI have been presented. There are 12 Raman bands of PTCDI on graphene to be considered. Based on previous measured and calculated Raman bands of PTCDI by Chiş et al., 2009, the bands occur due to the interaction of CC stretching, CH in plane bending, CN symmetric stretching and central rings

stretching. The three most intense bands (D, G and 2D bands) of single layer graphene can be distinguished from the Raman spectrum. From the measurement of the intensity of PTCDI bands on SiO_2 and PTCDI on graphene of 5 min exposure (0.09 ML), we found that the enhancement factor of PTCDI on graphene is ~13.

We studied PTCDI on different layers of exfoliated graphene, which is known high quality. This work has shown that Raman signal of PTCDI on single layer graphene is stronger than on few-layer and graphite, as expected. Then we compared PTCDI on exfoliated graphene and on transferred epitaxial graphene, which then we found the intensity difference is considerably small and is not significantly influenced by the graphene quality.

We also investigated the PTCDI coverage dependence. The PTCDI exposure of 1 min, 2 min and 5 min, produces 1.8%, 3.6% and 9% ML of PTCDI respectively. From this experiment, we found that Raman band 6 has the highest intensity, which corresponds to CC stretching coupled with CH in plane bending. We have shown that the PTCDI molecules can be detected at a small fraction of a monolayer coverage on single layer graphene.

Finally we investigated a PTCDI monolayer on graphene/Ni before transferring it to SiO_2 using the same transfer method typically used for graphene. Before transfer (graphene/Ni), only bands 1, 2, 4, 5, 6, and 11 are resolved. After transfer (graphene/SiO_2), all the PTCDI bands are observed and has higher intensity than before transfer. Generally, we managed to detect GERS of PTCDI after the transfer and we have demonstrated the role of substrate in enhancing the Raman signal of PTCDI.

Chapter 8

Conclusion

In this thesis, the growth of graphene-terminated Ni thin films using several different methods has been presented with the aim of achieving low defect single layer graphene. The characterization of the graphene was carried out directly on the graphene-terminated Ni and graphene on SiO_2 by using atomic force microscopy (AFM), scanning tunneling microsccpy (STM), X-ray diffraction (XRD), optical microscopy and Raman spectroscopy. The emphasis of the characterization is on Raman spectroscopy which provides the information about the graphene layers being investigated with the focus on the three most prominent Raman bands; D, G and 2D bands.

Before our work was reported (Pollard et al., 2009), graphene growth on Ni thin films mostly produced large-areas of few-layer graphene and the process was rather complicated (Obraztsov, 2007; Yu et al., 2008; Reina et al., 2009). For the application of graphene based devices, the growth of single layer graphene is of interest and new methods for the controlled growth are required. We have presented methods for the production of large areas of single layer graphene using the very simple process of annealing Ni thin films in vacuum. This process involves converting trace amounts into single layer graphene and is highly reproducible. The films obtained have a higher fraction of single layer than alternative graphene

growth process on Ni film. We also emphasize the importance of considering unintentional carbon sources when developing models for graphene growth.

The control of graphene defects is required depending on the application, in which commonly, high quality of graphene layers is required. We have grown graphene by exposure to propylene, which formed a large-area of single layer, but with relatively high Raman D band intensity, commonly observed for CVD graphene grown on Ni films. We have demonstrated a significant reduction of the Raman D band by fine tuning the growth parameters; the annealing temperature, exposure time and Ni film thickness. Our results show that higher temperature and longer exposure to carbon containing gas with thicker Ni films produce low defect single layer graphene with a considerably good coverage. So a considerable progress towards a large coverage of low defect graphene grown on Ni film is presented.

The growth of graphene on Ni has been studied extensively using various methods. In this thesis we demonstrated an alternative solid state approach for the formation of graphene by decomposition of C_{60}. We found that the C_{60} coverage, annealing temperature, and deposition sequence influence the properties of graphene layers. This molecular source of carbon provides a method of controlling the total dosage of carbon introduced into the film with a high degree of precision. This approach results in high fraction of single layer graphene, but with relatively high Raman D band intensity. Our results also show that carbon present at the buried metal/ SiO_2 layer can diffuse and segregate at the surface, and has verified that trace amounts on SiO_2 can give rise to the formation of graphene. This suggests the importance of removal the trace amounts by annealing, or outgassing.

Research on graphene enhanced Raman scattering (GERS) was only explored since two years ago, which has shown that graphene is a very good substrate for enhancing the Raman signal and there are only a few studies of Raman spectroscopy of PTCDI reported. We have presented preliminary results of GERS of adsorbed molecules, PTCDI. We compared our results with Chiş et al., 2009, which gives the assignment of the PTCDI Raman bands. Our results showed that the PTCDI

molecules can be detected at a small fraction of a monolayer coverage on single layer graphene. We have also demonstrated the effect of a substrate for graphene which can give rise to the enhancement of a Raman signal of adsorbed molecules.

This thesis has presented several approaches to grow graphene on Ni films such as converting carbon containing adsorbates into graphene, exposure to carbon containing gas and a solid state approach to decomposition of molecules. Overall, we have successfully produced single layer graphene over large areas and we have shown that the amount of defects in graphene quantified by the Raman D band can be controlled. We have also studied GERS of PTCDI, which is one application of graphene.

8.1 Suggestions for future work

The graphene growth discussed previously, produces graphene with rather high Raman D band intensity. The reduction of the D band intensity by fine tuning the growth parameters need a more detailed study especially on the cooling step after the annealing. We normally do the cooling to room temperature in 1 – 2 min by reducing the current through a silicon strip heater to zero, but the actual temperature of the sample does not reduce as abrupt as we expected. The actual temperature on the sample surface during the cooling process may be measured in the future. The effect of the cooling rate to the formation of graphene and defects could be studied in a more structured manner.

Since some defects in graphene are zero-dimensional and pointlike, the amount of disorder can be provided by the distance between defects, L_D. Recently, experiments on quantifying L_D using Raman spectroscopy were reported (Cancado et al., 2011; Lucchese et al., 2010; Martins Ferreira et al., 2010). The same approach can be carried out to study our graphene layers to quantify the amount of pointlike

defects based on different growth parameters, such as the annealing temperature, exposure to carbon source and cooling rate.

The distribution of the defective area can be measured by Raman mapping of the graphene layer. This mapping was not carried out before because of the limited access to the Raman system since it will take a longer scanning time than on a point. As presented, all the growth methods formed a majority of single layer. The coverage of single layer and few-layer can also be measured precisely by performing the Raman mapping. The effect of different laser excitation energy can also be performed in the future. Other than that, parameters that influence the Raman shift for each graphene bands can also be investigated.

Graphene growth by immersion in organic solvents was initially performed to investigate the effect of outgassing process and single layer graphene is formed but high defective. The defects quantified by the Raman D band intensity for samples produced using this method are 2x higher than all the graphene layers produced by other methods presented in this thesis. A detailed study can be carried out to reduce the defects by investigating the immersion time, annealing temperature and time as well as the cooling rate. For alternative solid-state approach in graphene growth on Ni film, the graphene quality can be further improved using different molecular precursors while maintaining the high fraction of single layer.

The work on GERS of PTCDI is still in early stage. Since only Chiş et al., 2009, reported an almost complete assignments for the PTCDI Raman bands, a further experiment and calculation can be carried out, particularly for PTCDI on graphene. As presented before, there are some PTCDI bands on graphene observed but not obtained by Chiş et al., 2009. We notice that there is a slight shift in the PTCDI bands for different graphene layer which may influenced by the amount of defects, PTCDI coverage and exposure. A further study can be performed to investigate the parameters that can affect the Raman shift and of the origin of this effect.

We have investigated fullerenes on graphene using Raman spectroscopy but we did not observe Raman enhancement as we obtained with PTCDI. This may

caused by the unsuitable laser excitation and the fact that graphene may not be a suitable substrate for SERS of fullerenes. A further investigation is needed to verify this analysis. Since graphene has proven to be a good substrate for SERS effect, other adsorbed molecules can be investigated.

References

Albrecht M.G. and Creighton J.A., 1977, Anomalously intense Raman spectra of pyridine at a silver electrode, *J. American Chem. Soc.* **99**, 15, 5215

Alov N.V., 2005, Fifty years of x-ray photoelectron spectroscopy, *J. Anal. Chem.* **60**, 3, 297.

Balandin A. A., Ghosh S., Bao W., Calizo I., Teweldebrhan D., MiaoF and Ning Lau C., 2008, Superior thermal conductivity of single layer graphene, *Nano Lett.*, **8:3**, 902.

Baird D., Nordmann A, and Schummer *J., 2004, Discovering the nanoscale, Amsterdam: IOS Press.*

Banhart F., 2009, Interactions between metals and carbon nanotubes: At the interface between old and new materials, *Nanoscale*, **1**, 201.

Banhart F., Kotakoski J. and Krasheninikov A. V., 2011, Structural defects in graphene, *Rev ACS Nano*, **5**, **1**, 26.

Berciaud S., Ryu S., Brus L.E., Heinz T.F., 2009, Probing the intrinsic properties of exfoliated graphene: Raman spectroscopy of free standing monolayers, *Nano Lett.* **9**, 346.

Berger, C.; Song, Z. M.; Li, T. B.; Li, X. B.; Ogbazghi, A. Y.; Feng, R.; Dai, Z. T.; Marchenkov, A. N.; Conrad, E. H.; First, P. N.; de Heer, W. A., 2004, Ultrathin epitaxial graphite: 2-D electron gas properties and a route toward graphene based nanoelectronics, *J. Phys. Chem. B*, **108**, 19912.

Berger, C.; Song, Z. M.; Li, X. B.; Wu, X. S.; Brown, N.; Naud, C. Mayou, D.; Li, T. B.; Hass, J.; Marchenkov, A. N.; Conrad, E. H.; First, P. N.; de Heer, W. A., 2006, Electronic confinement and coherence in patterned epitaxial graphene, *Science*, **312**, 1191.

Blake P., Hill E.W., Castro Neto A.H., Novoselov K.S., Jiang D., Yang R., Booth T.J., Geim A.K., 2007, Makin graphene visible, *Appl. Phys. Lett.*, **91**, 063124.

Blunt M., Far from equilibrium nanoparticle assembles: patterns transport and dynamics, *PhD Thesis.*

Bonzel H.P. & Krebs, 1980, On the Chemical Nature of the Carbonaceous Deposits on Iron after. CO Hydrogenation, *Surf. Sci.* **91**, 499.

Bunch, J. S., 2008, PhD Thesis: Mechanical and electrical properties of graphene sheets. Cornell University.

Campagnoli G., and Tossati E., 1989, in Progress on Electron Properties of Metal, edited by Girlanda R. et al, Kluwer Dordrecht, 337.

Cancado L.G., Jorio A., Martins Ferreira E.H., Stavale F., Achete E.A., Capaz R.B., Mautinho M.V.O., Lombardo A., Kulmala T.S., and Ferrari A.C., 2011, Quantifying defects in graphene via Raman spectroscopy at different excitation energies, *Nano Lett.* **11**, 3190.

Casiraghi C., Hartschuh A., Qian H., Piscanec S., Georgi C., Fasoli A., Novoselov K.S., Basko D.M. and Ferrari A.C., 2009, Raman spectroscopy of graphene edges, *Nano Lett.* **9**, 1433.

Casiraghi C., Pisana S., Novoselov K.S., Geim A.K., Ferrari A.C., 2007, Raman fingerprint of charged impurities in graphene, *Appl. Phys. Lett.*, **91**, 233108.

Castro E.V., Ochoa H., Katsnelson M.I., Gorbachev R.V., Elias D.C., Novoselov K.S., Geim A.K. and Guinea F., 2010, Limits on carrier mobility in suspended graphene due to flexural phonons, *Phys. Rev. Lett.* **105**, 266601.

Castro Neto A. H., Guinea H., Peres N. M. R., Novoselov K. S. and Geim A. K., 2009, The electronic properties of Carbon, *Rev. Mod. Phys.* **81**, 109.

Cepek C., Goldoni A. and Modesti S., 1996, Chemisorption and fragmentation of C60 on Pt(111) and Ni(111), *Phys. Rev. B* **53**, 7466.

Chambers A., Fitch R.K., and Halliday B. S., 1998, Basic Vacuum Technology, 2nd Ed., *IOP Publishing Ltd*, ISBN **0 7503 0495 2**.

Charlier J.C., Eklund P.C., Zhu J., and Ferrari A.C., 2008, Electron and phonon properties of graphene: their relationship with carbon nanotubes, *Topics Appl. Phys* **111**, 673.

Chiş V., Mile G., Ştiufiuc R., Leopold N., and Oltean M., 2009, Vibrational and electronic structure of PTCDI and melamine-PTCDI complexes, *J. Mol. Struc.* **924**, 47.

Das Sarma S., Adam S., Hwang E.H., Rossi E., Electronic transport in two dimensional graphene, 2011, *Rev. Mod. Phys.* **83**, 407.

Davidson M. W. and Abramowitz M., 2002, Optical Microscopy, Encyclopedia of Imaging Science and Technology, John Wiley & Sons.

Dedkov Y.S., Fonin M. and Laubschat C., 2008, A possible source of spin-polarized electrons: inert graphene/Ni(111) system, Appl. Phys. Lett. **92**, 052506.

Dedkov Y.S., Fonin M., Rüdiger U and Laubschat C., 2008, Graphene Ni (1 1 1) System: spin- and angle-resolved photoemission studies, *arXiv DL- 10.* **1**.

de Heer W. A., Berger C., Wu X., First P. N., Conrad E. H., Li X., Li T., Sprinkle M., Hass J., Sadowski M. L., Potemski M. and Martinez G., 2007, Epitaxial graphene, *Solid State Commun.* **143**, 92.

Eckertová L., 1986, Physics of Thin Films, *Plenum Press, New York and London*, 23.

Eda, G.; Fanchini, G.; Chhowalla, M., 2008, Large-area ultrathin films of reduced graphene oxide as a transparent and fl exible electronic material, *Nat. Nanotechnol.*, **3**, 270.

Eizenberg M. and Blakely J., 1979, carbon monolayer phase condensation on Ni(111), *Surf. Sci.* **82**, 228.

Elias D. C., Nair, R. R., Mohiuddin T. M. G., Morozov S. V., Blake P., Halsall M. P., Ferrari A. C., Boukhvalov D. W., Katsnelson M. I., Geim A. K., Novoselov K. S., 2009, Control of graphene's properties by reversible hydrogenation: evidence for graphene, *Science* **323**, 5914, 610.

Farias D., Shikin AM., Rieder K.-H., and Dedkov Y.S., 1999, Synthesis of a weakly bonded graphite monolayer on Ni(111) by intercalation of silver, *J. Phys.: Condens. Matter*, **11**, 8453.

Ferrari A.C., 2007, Raman spectroscopy of graphene and graphite: Disorder, electron-phonon coupling, doping and nonadiabatic effects, *Solid State Comm.*, **143**, 47.

Ferrari A. C., Meyer J. C., Scardaci V., Casiraghi C., Lazzerri M., Mauri F., Piscanec S., Jiang D., Novoselov K. S., Roth S., and Geim A. K., 2006, Raman spectrum of graphene and graphene layers, *Phys. Rev. Lett.*, **97**, 187401.

Ferraro J.R., Nakamoto K., and Brown C.W., 2003, Introductory Raman spectroscopy, Academic Press.

Fleischman M., Hendra P.J., McQuillan A.J., 1974, Raman spectra of pyridine adsorbed at a silver electrode, *Chem. Phys. Lett.* **26**, 2, 163.

Franc J. and Bastl Z., 2008, Nickel evaporation in high vacuum and formation of nickel oxide nanoparticles on highly oriented pyrolytic graphite. X-ray photoelectros spectroscopy and atomic force microscopy study, *Thin Sol. Film*, **516**, 18, 6095.

Fujita D., Ohgi T., Onishi K., Kumakura T., Harada M., 2003, Discovery of carbon nanowires formed on the carbon-doped Ni(111) substrate by a bulk-to-surface precipitation process, *Jpn. J. Appl. Phys.* **42**, 1391.

Fujita D., Schleberger M. and Tougaard S., 1995, XPS study of the surface enrichment process of carbon on C-doped Ni (111) using inelastic background analysis, *Surf. Sci.* **331**, 343.

Fujita D. and Yoshihara K. J., 1994, Surface precipitation process of epitaxially grown graphite (0001) layers on carbon-doped nickel(111) surface, *Vac. Sci. Technol. A* **12**, 2134.

Gamo Y., Nagashima A., Wakabayashi M., Terai M., Oshima C., 1997, Atomic structure of monolayer graphite formed on Ni (111), *Surf. Sci.* **374**, 61.

Geim A.K. and Novoselov K.S., 2007, The rise of graphene, *Nature*, **6**, 183.

Giessbl F. J., 2003, Advances in atomic force microscopy, *Rev. Mod. Phys.* **75**, 949.

Girit C.O., Meyer J. C., Erni R., Rossell M.D., Kisielowski C., Yang L., Park C.-H, Crommie M.F., Cohen M.L., Louie S.G., 2009, Graphene at the edge: stability and dynamics, *Science* **323**, 1705.

Gomez-Navarro C., Weitz R. T., Bittner A. M., Scolari M., Mews A., Burghard M., Kern K., 2007, Electronic transport peoperties of individual chemically reduced graphene oxide sheets, *Nano Lett.* **7**, 11, 3499.

Graf D., Molitor F. and Ensslin K., 2007, Spatially resolved Raman spectroscopy of single- and few-layer graphene, *Nano Lett.* **7**, 2, 238.

Grant J.T. and Haas T.W., 1970, A study of Ru(0001) and Rh(111) surfaces using LEED and Auger electron spectroscopy, *Surf. Sci.*, 21, 76.

Grüneis A., Kummer K. and Vyalikh V., 2009, Dynamic of graphene growth on a metal surface: a time dependent photoemission study, *New J. Phys.* **11**, 073050.

Guinea F., Castro Neto A. H., Peres N. M. R., 2007, Electronic properties of stacks of graphene layers, *Solid State Commun.* **143**, 116.

Gupta A., Chen G., Joshi P., Tadigadapa S., and Eklund P. C., 2006, Raman scattering from high frequency phonons in supported n-graphene layer films, *Nano Lett.* **6**, 12, 2667.

Hauschild A., Karki K., Cowie B.C.C., Rohlfing M., Tautz F.S., Sokolowski M., 2005, Molecular distortions and chemical bonding of a large π-conjugated molecule on a metal surface, *Phys. Rev. Lett.* **94**, 036106.

Hernandez, Y.; Nicolosi, V.; Lotya, M.; Blighe, M.; Sun, Z.; De, S.; McGovern, I. T.; Holland, B.; Byrne, M.; Gun'ko, Y. K.; Boland, John J.; Niraj, P.; Duesberg, G.; Krishnamurthy, S.; Goodhue, R.; Hutchison, J.; Scardaci, V.; Ferrari, Andrea C.; Coleman, Jonathan N., 2008, High-yield production of graphene by liquid-phase exfoliation of graphite, *Nat. Nanotechnol.*, ***3***, 563.

Himpsel F. J., Christmann K., Heimann P., Eastman D. E. and Feibelman P.J., 1982, Adsorbate band dispersions for C on Ru (0001), *Surface Science.* **115**, L159

Hofrichter J., Szafranek B.N., Otto M., Echtermeyer T.J., Baus M., Majerus A., Geringer V., Ramsteiner M., Kurz H., 2010, Synthesis of graphene on Silicon Dioxide by a solid carbon source, *Nano Lett.* **10**, 36.

Honig R.E, 1962, Vapor pressure data for the solid and liquid elements, *RCA Rev.* **23**, 567.

Huang P.Y., Ruiz-Vargaz C.S., van der Zande A.M., Whitney W.S., Levendorf M.P., Kevek J.W., Garg S., Alden J.S., Hustedt C.J., Zhu Y., Park J., McEuen P.L., Muller D.A., 2011, Grains and grain boundariesin single layer graphene atomic patchwork quilts, *Nature*, **469**, 389.

Ismach A., Druzgalski C., Penwell S., Schwartzberg A., Zheng M., Javey A., Bokor J., and Y. Zhang, 2010, Direct chemical vapour deposition of graphene on dielectric surfaces, *Nano Lett.* **10**, 1542.

Jeanmarie D.L. & van Duyne R.P., 1977, Surface Raman electrochemistry Part I. Heterocyclic, aromatic and aliphatic amines adsorbed on the anodized silver electrode, *J. Electroanal. Chem.* **84**, 1.

Jiang J., Saito R., Samsonidze Ge. G., Chou S. G., Jorio A., Dresselhaus G, and Dresselhaus M. S., 2005, Electron-phonon matrix elements in single-wall carbon nanotubes, *Phys. Rev. B* **72**, 235408.

Jung N., Crowther A.C., Kim N., Kim P., Louis B., 2010, Raman enhancement on graphene: adsorbed and intercalated molecular species, *ACS Nano*, **4**, 11, 7005.

Kaake L.G., Zou Y., Panzer M.J., Frisbie C.D., Zhu X.-Y., 2007, Vibrational spectroscopy reveals electrostatic and electrochemical doping in organic thin film transistors gated with a polymer electrolyte dielectric, *J. Am. Chem. Soc.* **129**, 7824.
Kelly, B. T., 1981, Physics of graphite. London; Englewood, N.J., Applied Science.

Kim K. S., Zhao Y., Jang H., Lee S. Y., Kim J. M., Kim K. S., Ahn J. H., Kim P., Choi J. Y., Hong B. H., 2009, Large-scale pattern growth of graphene films for stretchable transparent electrodes, *Nature*, **457**, 706.

Kumar S., McEvoy N., Lutz T., Keeley G.P., Nicolosi V., Murray C.P., Blau W.J., Duesberg G.S., 2010, Gas phase controlled deposition of high quality large area graphene films, *Chem. Commun.* **46**, 1422.

Kusch C., Winter B., Mitzner R., Gomes Silva A., Campbell E.E.B., Hertel I. V., 1997, Stability of photo-excited C60 chemisorbed on Ni(111), *Chem. Phys. Lett.* **275**, 469.

Lahiri, J.; Lin, Y.; *Bozkurt, P.; Oleynik,* I. I.; Batzill, M., 2010, An Extended Defect in Graphene as a Metallic Wire., *Nat. Nanotechnol.*, **5**, 326.

Landau L.D., 1937, Zur Theorie der phasenumwandlungen II., *Phys. Z. Sowjetunion* **11**, 26.

Lee C., Wei X., Kysar J.W., Hone J., 2008, Measurement of the elastic properties and instrinsic strength of monolayer graphene, *Science*, 321.

Lespade P., Marchand A., Couzi M., and Cruege F., 1984, Caracterisation de materiaux carbones par microspectrometrie Raman, *Carbon* **22**, 375.

Levendorf M.P.; Ruis-Vargas C.S.; Garg S. and Park J., 2009, Transfer-free batch fabrication of single layer graphene transistors, *Nano Lett.* **9**, 12, 4479.

Li, D.; Mueller, Marc B; Gilje, S.; Kaner, Richard B.; Wallace, Gordon G., 2008, Processable aqueous dispersions of graphene nanosheets, *Nat. Nanotechnol.*, **3**, 101 105.

Li X., Cai W., An J., Kim S., Nah J., Yang D., Piner R., Velamakanni A., Jung I., Tutuc E., Banerjee S.K., Colombo L., Ruoff R.S., 2009, Large-area synthesis of high quality and uniform graphene films on copper foils, *Science* **324**, 1312.

Ling X., Xie L., Fang Y., Xu H., Zhang H., Kong J., Dresselhaus M.S., Zhang J., and Liu Z., 2010, Can graphene be used as substrate for Raman enhancement?, *Nano Lett.* **10**, 553.

Ling X. and Zhang J., 2010, First layer effect in graphene-enhanced Raman scattering, *Small* **6**, 18, 2020.

Ling X. and Zhang J., 2011, Interference phenomenon in graphene-enhanced Raman scattering, *J. Phys. Chem. C* **115**, 2835.

Livneh T., Haslett T. L. and Moskovits M., 2002, Distinguishing disorder-induced bands from allowed Raman bands in graphite, *Phys. Rev. B* **66**, 195110.

Lucchese M.M., Stavale F., Ferriera E.H., Vilane C., Moutinho M.V.O., Capaz R.B., Achete C.A., Jorio A., 2010, Quantifying ion-induced defects and Raman relaxation length in graphene. *Carbon* **48**, 1592.

Lui C. H., Li Z., Chen Z., Klimov P. V., Brus L. E., and Heinz T. F., 2011, Imaging Stacking Order in Few-Layer Graphene, *Nano Lett.* **11**, 164.

Mafra D. L., Samsonidze G., Malard L. M., Elias D. C., Brant J. C., Plentz F., Alves E. S., Pimenta M. A.,2007, Determination of LA and TO phonon dispersion relation of graphene near the Dirac point by double resonance Raman scattering, *Phys. Rev. B.* **76**, 233407.

Malard, L. M., Pimenta, M. A., Dresselhaus G., and Dresselhaus M. S., 2009, Raman spectroscopy of graphene, *Physics Reports*, **473**, 51.

Malola S., Ha¨kkinen H. And Koskinen P., 2010, Structural, chemical, and dynamical trends in graphene grain boundaries, *Phys. Rev. B.*, **81**, 165447.

Martins Ferreira E.H., Moutinho M.V.O., Stavale F., Lucchese M.M., Capaz R.B., Achete C.A., Jorio A., 2010, Evolution of the Raman spectra from single-, few-, and many-layer graphene with increasing disorder. *Phys. Rev. B* **82**, 125429.

Mattevi C., Kima H., and Chhowalla M., 2011, A review of chemical vapour deposition of graphene on copper, *J. Mater. Chem.*, **21**, 3324.

Maultzsch J., Reich S., Thomsen C., Requardt H. and Ordejon P., 2004, Phonon dispersion in graphite, *Phys. Rev. Lett.* **92**, 7.

McCann E. and Fal'ko V. I., 2006, Landau level degeneracy and quantum Hall effect in a graphite bilayer, *Phys. Rev. Lett.* **96**, 086805.

McClure, J. W., 1956, Diamagnetism of graphite, *Phys. Rev.*, **104**, 666.

Meyerhofer D., 1978, Characteristics of resist films produced by spinning, *J. Appl. Phys.* **49**, 7, 3393.

Mrozek I. and Otto A., 1990, Long and short range effects in SERS from Silver, *Eerophys. Lett.* **11**, 243.

Müller F., Sachdev H., Hufner S., Pollard A.J., Perkins E.W., Russell J.C., Beton P.H., Gsell S., Fischer M., Schreck M., Stritzker B., 2009, How does graphene grow?Easy access to well ordered grapphene films, *Small* **5**, 2291.

Mura M., Silly F., Briggs G.A.D., Castell M.R. and Kantorovich L.N., 2009, H-bonding supramolecular assemblies of PTCDI molecules on the Au(111) surface, *J. Phys. Chem. C* **113**, 21840.

Nair R.R., Blake P., Grigorenko A.N., Novoselov K.S., Booth T.J., Stauber T., Peres M.R., Geim A.K., 2008, Fine structure constant defines visual transparency of graphene, *Science*, **320:3881**, 1308.

Nandamuri G., Roumimov S., and Solanki R., 2010, Chemical vapor deposition of graphene films, *Nanotech.* **21**, 145604.

Novoselov, K. S., Geim A.K., Morozov S.V., Jiang D., Zhang Y., Dubonos S.V., Griegoriva I.V. and Firsov A.A., 2004, Electric field effect in atomically thin carbon films, *Science*, **306**, 666.

Neddermeyer H., 1996, Scanning tunneling microscopy of semiconductor surfaces, *Rep. Prog. Phys.* **59**, 701.

Novoselov, K. S., Jiang D., Schedin F., Booth T.J., Khotkevich V.V., Morosov S,V. and Geim A.K., 2005, Two-dimensional atomic crystals., *Proc. Natl Acad. Sci. USA*, **102**, 10451.

Novoselov K.S. et al., 2007, Room temperature quantum Hall effect in graphene, *Science*, 1137201.

Obraztsov, A. N.; Obraztsova, E. A.; Tyurnina, A. V.; Zolotukhin, A. A., 2007, Chemical vapor deposition of thin graphite films of nanometer thickness, *Carbon*, **2017**, 45.

Ohnesorge F., Binning G., 1993, True atomic resolution by atomic force microscopy through repulsive and attractive forces, *Science* **260**, 1451.

Ohta T., Bostwick A., Seyller T., Horn K., Rotenberg E., 2006, Controlling the Electronic Structure of Bilayer Graphene, *Science* **313**, 951.

Pimenta M.A., Dresselhaus G., Dresselhaus M.S., Cancado L.G., Jorio A., Saito R., 2007, Studying disorder in graphite based systems by Raman spectroscopy, Physical Chem Chem Phys. **9**, 1276.

Perdigao L.M.A., Perkins E.W., Ma J., Staniec P.A., Rogers B.L., Champness N.R. & P.H. Beton, 2006, Bimolecular networks and supramoleculartraps on Au(111), *J. Phys. Chem. B* **110**, 12539.

Perdigao L.M.A., Sabki S.N., Garfitt J.M., Capiod P., Beton P.H., 2011, Graphene formation by decomposition of C60, *J. Phys. Chem C.*, **115**, 7472.

Pollard A. J., Nair R. R., Sabki S. N., Staddon C. R., Perdigao L. M. A., Hsu C. H., Garfitt J. M., Gangopadhyay S. , Gleeson H. F., Geim A. K., and Beton P. H., 2009, Formation of Monolayer Graphene by Annealing Sacrificial Nickel Thin Films, *J. Phys. Chem C.*, **113**, 16565.

Pollard A.J., Perkins E.W., Smith N., Saywell A., Goretzki G., Phillips A., Argent S., Sachdev H., M€uller F., H€ufner S., Gsell S., Fischer M., Schreck M., Osterwalder J., Greber T., Berner S., Champness N.R., Beton P. H., 2010, Supramolecular assemblies formed on an epitaxial graphene superstructure, *Angew. Chem. Int. Ed.*, **49**, 1794.

Rao C.N.R., Sood A.K., Subrahmanyam, K.S. and Govindraj A.,2009, Graphene: The new two-dimensional nanomaterial, *Angew. Chem. Int. Ed.* 7752.

Reich S. and Thomsen C., 2004, Raman spectroscopy of graphite, *Phil. Trans. R. Soc. Lond. A* **362**, 2271.

Reina A., Jia X. T., Nezich, J., Son, H. B., Bulovic, V., Dresselhaus, M. S., Kong, J., 2009, Large area, few-Layer graphene films on arbitrary substrates by chemical vapor deposition, *Nano Lett.*, **9**, 3035.

Reina A., Thiele S., Jia X., Bhaviripudi S., Dresselhaus M. D., Schaefer J. A. and Kong J., 2009, Growth of large-area single- and bi-layer graphene by controlled carbon precipitation on polycrystalline Ni surfaces, *Nano Res.* **2**, 509.

Ruan G., Sun Z., Peng Z., Tour J.M., 2011, Growth of graphene from food, insects and wastes, *ACS Nano*, **5**, 9, 7601.

Saito R., Dresselhaus G. and Dresselhaus M. S., 1998, Physical Properties of Carbon Nanotubes. Imperial, London.

Schedin F., Lidorikis E., Lombardo A., Kravets V.G., Geim A.K., Grigorento A.N., Novoselov K.S., Ferrari A.C., 2010, Surface-enhanced Raman spectroscopy of graphene, *ACS Nano* **10**, 5617.

Shelton J. C., Patil H. R., and Blakeley J. M., 1974, Equilibrium segregation of carbon to a nickel (111) surface: A surface trace transition, *Surf. Sci.* **43**, 493.

Shelton J.C., Patil H. and Blakely J., 1974, Equilibrium segregation of carbon to a nickel(111) surface: A surface phase transition, *Surf. Sci.* **43**, 493.

Slonczewski, J. C. & Weiss, P. R., 1958, Band structure of graphite. *Phys. Rev.*, **109**, 272.

Sun Z., Yan Z., Yao J., Beitler E., Zhu Y., and Tour J. M., 2010, Growth of graphene from solid carbon sources, *Nature* **468**, 549.

Sutter E., Albrecht P., and Sutter P., 2009, Graphene growth on polycrystalline Ru thin films, *Appl. Phys. Lett.*, **95**, 133109.

Sutter P. W., Albrecht P. M., and Sutter E. A., 2010, Graphene growth on epitaxial Ru thin films on sapphire, *Appl. Phys. Lett.* **97**, 213101.

Stankovich, S.; Dikin, D. A.; Piner, R. D.; Kohlhaas, K. A.; Kleinhammes, A.; Jia, Y.; Wu, Y.; Nguyen, S. T.; Ruoff, R. S., 2007 Synthesis of graphene-based nanosheets via chemical reduction of exfoliated graphite oxide, *Carbon*, **45**, 1558.

Swarbrick J.C., Ma J., Theobald J.A., Oxtoby N.S., O'Shea J.N., Champness N.R., Beton P.H., 2005, Square, hexagonal, and row phases of PTCDA and PTCDI on Ag-Si(111) [root]3 x [root]3R30°, *J. Phys. Chem. B* **109**, 12167.

Tersoff J. and Lang N. D., 1993, Theory of scanning tunneling microscope, *Meth. Exp. Phys.* **27**, 1.

Usachov D., Dobrotvorskii A.M., Varykhalov A., Rader O., Gudat W., Shikin A.M., Adamchuk V. K., 2008, Experimental and theoretical study of the morphology of the commensurate and incommensurate graphene layers on Ni single crystal surfaces, *Phys. Rev. B* **78**, 085403.

Vasquez de P., Calleja A. L. F., Borca B., Passeggi Jr., Hinajero J. J., Guinea F., and Miranda R., 2008, Periodically rippled graphene: growth and spatially resolved electronic structure, *Phys. Rev. Lett.* **100**, 056807.

Wallace P. R., 1947, The band theory of graphite, *Phys. Rev.* **71**, 622.

Xie L.M., Ling X., Fang Y., Zhang J., Liu Z.F., 2009, Graphene as a substrate to suppress fluorescence in resonance Raman spectroscopy, *J. Am. Chem. Soc.* **131**, 9890.

Yazyev, O. V. and Louie, S. G., 2010, Topological Defects in Graphene: Dislocations and Grain Boundaries. *Phys. Rev. B* **81**, 195420.

Yoshii S., Nozawa K., Toyoda K., Matsukawa N., Odagawa A., and Tsujimura A., 2011, Suppression of Inhomogeneous Segregation in Graphene Growth on Epitaxial Metal Films, *Nano Lett.* **11**, 7, 2628.

Yu Q., Lian J., Siriponglert S., Li H., Chen Y. P., and Pei S. S., 2008, Graphene segregated on Ni surfaces and transferred to insulators, *Appl. Phys. Lett.*, **93**, 113103.

Zahn D.R.T., Salvan G., Paez B.A., Scholz R., 2004, Interaction between metals and organic semiconductors studied by Raman spectroscopy, *J. Vac. Sci. Technol. A* **22**, 1482.

Zhou J.B., Gustafsson T., Lin R.F. and Garfunkel E., 1993, Medium energy ion scattering study of Ni on ultra thin films of SiO_2 on Si (111), *Surface Science* **281**, 1, 67.

Appendices

Appendix A

Raman intensity ratio for spectra in Figure 7.7. The band number can be referred to Figure 7.2.

Band no. & Raman shift (cm^{-1})	Raman intensity of PTCDI on graphene (A) (a.u.)	Raman intensity of PTCDI on SiO_2 (B) (a.u.)	Ratio A/B
2: 1303	1410	135	10.4
4: 1374	1610	121	13.3
6: 1569	1470	102	14.4
7: 1585	827	56	14.8

Appendix B

PTCDI Raman band position (Raman shift, cm^{-1}) and intensity (a.u.) for Figure 7.5

Exfoliated graphene	Monolayer		Few-layer		Graphite	
Band number	Pos (cm^{-1})	Intensity (a.u.)	Pos (cm^{-1})	Intensity (a.u.)	Pos (cm^{-1})	Intensity (a.u.)
1	1292	2.31	1292	1.51	1295	0.39
2	1302	2.19	1302	1.30	1304	0.72
4	1370	2.92	1370	2.00	1373	0.95
6	1565	2.41	1566	2.07	1577	2.56

Appendix C

Raman bands position (Raman shift, cm^{-1}) and intensity (a.u.) for different coverages of PTCDI.

Exposure (% ML)	1 min (1.8% ML)		2 min (3.6% ML)		5 min (9% ML)	
Band No.	Pos (cm^{-1})	Intensity (a.u.)	Pos (cm^{-1})	Intensity (a.u.)	Pos (cm^{-1})	Intensity (a.u.)
1	1296	0.55	1296	1.92	1296	2.33
2	1306	0.27	1307	1.03	1307	1.81
4	1374	0.55	1374	1.96	1374	2.54
6	1569	0.61	1569	2.05	1569	2.59
7	1585	0.78	1585	1.25	1585	1.45

Appendix D

Raman bands position (Raman shift, cm^{-1}) and intensity (a.u.) for PTCDI (a) before transfer (graphene/Ni) and (b) after transfer (graphene/SiO_2)

Sample	(a) before transfer		(b) after transfer	
Band no.	Pos (cm^{-1})	Intensity (a.u.)	Pos (cm^{-1})	Intensity (a.u.)
2	1302	5130	1307	16100
4	1376	3610	1376	18700
6	1575	3440	1572	19100